

Construction of a spectroscopic terahertz time-domain ellipsometer

by

Shane Raymond Smith



*Dissertation presented for the degree of Doctor of
Philosophy in Physics in the Faculty of Nature Science in the
Faculty of Nature Science at Stellenbosch University*

Supervisor: Dr. P.H. Neethling

Co-supervisor: Prof. E.G. Rohwer

March 2020

Declaration

By submitting this dissertation electronically, I declare that the entirety of the work contained therein is my own, original work, that I am the sole author thereof (save to the extent explicitly otherwise stated), that reproduction and publication thereof by Stellenbosch University will not infringe any third party rights and that I have not previously in its entirety or in part submitted it for obtaining any qualification.

Date:

Copyright © 2020 Stellenbosch University
All rights reserved.

Opsomming

Ontwikkeling van 'n spektroskopiese terahertz tyd-domein ellipsometer

(“Construction of a spectroscopic terahertz time-domain ellipsometer”)

S.R. Smith

Departement Fisika,

Universiteit Stellenbosch,

Privaatsak X1, Matieland 7602, Suid Afrika.

Proefskrif: PhD (Fisika)

Maart 2020

Terahertz bronne en ontvangers het baie ontwikkeling ondergaan in onlangse jare, wat gelei het tot 'n vergemakliking van laboratorium gebaseerde metings in hierdie spektrale gebied. In onlangse jare is dit ook gevind dat proteïene optiese eienskappe in die THz spektrale gebied het wat dit moontlik maak om hulle te identifiseer. Hierdie materiale moet in water geplaas word om hul natuurlike aard te toon. THz straling word egter sterk geabsorbeer deur water, en dus is dit moeilik om hierdie monsters met transmissie sisteme te bestudeer.

Ons stel voor die gebruik van 'n ellipsometriese weerkaatsing-gebaseerde sisteem om die beperking te oorkom. Ellipsometrie benodig nie 'n verwysings monster nie, wat 'n groot potensiële bron van belynings probleme kan wees in tradisionele weerkaatsings sisteme. 'n THz tyd-domein spektroskopiese ellipsometer is ontwikkel en gebou. Dit het ingesluit die ontwikkeling en vervaardiging twee polariseerders wat in die spektrale gebied funksioneer.

Twee ellipsometriese dataverwerkingsmetodes is ontwikkel om die data te verwerk wat deur die sisteem gemeet is. 'n Simulasie tegniek vir ellipsometriese data was ook ontwikkel om hierdie dataverwerkingsmetodes te toets voor hulle toegepas is op die gemete data. Twee bestaande dataverwerkingsmetodes was ook gebruik vir toets doeleindes.

Metings is gedoen op glasmonsters, silikonmonsters en etanol-water oplossings. Die vloeistofmonsters is geplaas in 'n kuvette met silikon vensters, wat deur ons ontwikkel en geproduseer is. Daar is gevind dat die sisteem en dataverwerkingstegnieke goed werk vir die glasmonsters. Ons tegnieke kon

die reële brekingsindeks van die silikonmonsters verkry met hoë akkuraatheid, maar aangesien die monsters hoogs deurlatend is het dit die beperkings van die metodes getoon met verwysing tot hoe akkuraat die uitdowingskoëffisiënt bepaal kan word uit die gemete data. Daar is ook gevind dat die sisteem data kan produseer waarmee vloeistofmonsters van mekaar onderskei kan word.

Abstract

Construction of a spectroscopic terahertz time-domain ellipsometer

S.R. Smith

*Department of Physics,
Stellenbosch University ,
Private Bag X1, Matieland 7602, South Africa.*

Dissertation: PhD (Physics)

March 2020

In recent years, developments in terahertz (THz) sources and detectors have come a long way, making lab based measurements in this spectral region far easier.

It has been found that proteins are identifiable in the THz region and have unique optical properties. These materials need to be suspended in an aqueous solution to maintain their natural behaviour. This is a limiting factor for transmission based THz spectroscopy, as THz radiation is strongly absorbed by water.

We propose the use of a reflection based ellipsometry system to overcome this limitation. Ellipsometry removes the need for a reference sample, which would potentially be a large source of alignment based error in a traditional reflection spectroscopy setup.

A terahertz time-domain spectroscopic ellipsometer was designed and constructed. This included the design and manufacture of two polarization optics.

An ellipsometry data simulation technique and two ellipsometry data extraction techniques were developed to analyze data measured by this system. Two other preexisting data extraction techniques were also tested.

Measurements were performed on glass samples, silicon samples, water and ethanol-water solutions. The liquid samples were housed in a silicon windowed cuvette we designed and manufactured.

It was found that the setup and techniques worked well with regard to the glass samples. The techniques could extract the real refractive index of the silicon samples with great accuracy, but as these samples were nearly transparent, they illustrated the limit to which the method developed can

ABSTRACT

v

currently extract the extinction coefficient from measured data. It is found that the system can produce data with which different liquid samples can be distinguished from one another.

Acknowledgements

I would like to express my sincere gratitude to the following people and organizations. To my supervisor, Dr P.H. Neethling, and co-supervisor, Prof E.G. Rohwer, for their continued help.

To my mother, Benita Heyburgh, for continued emotional and financial support.

To my aunt, Rene Staub, for supporting me emotionally and with administrative duties.

To my grandparents, Bennie and Marie Steffens, for supporting me emotionally.

To my one and only Jane Dai, without whom I would not have been able to make it through this endeavor.

To my friends, Paul Williams, Andre de Bruyn, Fredric Waso, Vihan Combrink, Jaco Moster and Carna Combrink for keeping me mentally and emotionally serviceable through these many years.

The Stellenbosch Physics department workshop staff who assisted me with acquiring materials and manufacturing components for my system, Lawrence Ashworth, Hugh Esterhuizen, Eben Shields, David Pool, Johan Germishuizen and Gerhard Louwrens.

Prof. Mark Tame, who assisted me financially in my final year.

The financial assistance of the National Research Foundation (NRF) towards this research is hereby acknowledged. Opinions expressed and conclusions arrived at, are those of the author and are not necessarily to be attributed to the NRF.

Contents

Declaration	i
Opsomming	ii
Abstract	iv
Acknowledgements	vi
Contents	vii
List of Figures	x
Nomenclature	xiv
1 Introduction	1
2 Background theory	3
2.1 Polarization	3
2.2 Complex refractive index	3
2.3 Fresnel Equations	4
2.4 Snell's Laws	7
2.5 Ellipsometry	8
3 Experimental setup	9
3.1 Terahertz generation and detection	9
3.1.1 Photo-conductive antennae as THz emitter	10
3.1.2 Photo-conductive antennae as THz receiver	11
3.2 Brewster stacks	12
3.3 Rotational mount	19
3.4 Layout	21
3.5 Nitrogen (N_2) Chamber	24
4 Simulation of THz ellipsometry measurements	28
4.1 Incident Electric Field	28
4.2 General transfer function	29

<i>CONTENTS</i>	viii
4.3 Geometric Correction	30
4.4 High resistivity silicon simulation example	32
5 Data Analysis	37
5.1 Bulk isotropic model	37
5.2 Single layer isotropic model	40
5.2.1 Transfer Function	42
5.2.2 Complex refractive index extraction	43
5.2.3 Smoothing algorithm: LULU	45
5.2.4 Error tolerance	47
5.2.5 Thickness extraction	51
5.2.6 Complete data extraction method	54
5.3 Single layer isotropic medium followed by bulk isotropic sample model	59
5.3.1 Two layer ellipsometric method	59
5.3.2 Self-reference method	64
5.3.3 Comparison	70
6 Results and discussion	73
6.1 System transfer function measurement	73
6.2 Bulk isotropic sample: Thick float glass	75
6.3 Single layer isotropic	77
6.3.1 Borosilicate Glass	77
6.3.2 High resistivity silicon	78
6.3.3 Lightly n-type doped silicon	81
6.4 Single layer isotropic medium followed by bulk isotropic sample	83
6.4.1 High resistivity silicon cuvette filled with water-ethanol mixture	83
6.4.1.1 Ellipsometry	85
6.4.1.2 Self-reference	85
6.4.1.3 Discussion	86
7 Conclusion	90
7.1 Future Work	91
Appendices	93
A Knife-Edge	94
B Alignment	97
B.1 Rotational mount alignment	97
B.2 Ellipsometric stage and THz antenna alignment	97
C Calculation of the geometric correction	101

CONTENTS

ix

Bibliography

105

List of Figures

2.1	Fresnel diagram	5
2.2	Reflection coefficients of high resistivity silicon.	6
3.1	Photo-conductive antenna diagram and image	11
3.2	Brewster stack photo	13
3.3	Brewster stack diagram	13
3.4	Spectrum with and without Brewster stacks	14
3.5	Spectrum of orthogonal and co-linear Brewster stack pairs	15
3.6	Intensity spectrum of orthogonal and co-linear Brewster stack pairs	16
3.7	Degree of polarization calculated for the silicon Brewster stacks . .	17
3.8	Extinction coefficient calculated for the silicon Brewster stacks . . .	18
3.9	Degree of polarization comparison	18
3.10	Rotational mount mock-up	19
3.11	Rotational mount diagram	20
3.12	Full optical setup diagram	21
3.13	Terahertz optical setup diagram	22
3.14	S- and P-reflection coefficient at 60° over refractive index	23
3.15	Ratio between p- and s-reflection coefficient at 60° over refractive index	23
3.16	THz water vapour real refractive index and absorption spectrum . .	25
3.17	Nitrogen gas chamber diagram	26
3.18	Measured THz spectrum with and without Nitrogen	26
4.1	Simulated terahertz electric field in time	29
4.2	Diagram depicting ray-trace of internal reflection compared to sur- face reflection	31
4.3	Measured p-polarized terahertz electric field in time for high resis- tivity silicon	32
4.4	Simulated p-polarized terahertz electric field in time for high resis- tivity silicon	33
4.5	Measured s-polarized terahertz electric field in time for high resis- tivity silicon	33
4.6	Simulated s-polarized terahertz electric field in time for high resis- tivity silicon	34

<i>LIST OF FIGURES</i>	xi
4.7 Comparison of measured and simulated p-polarized terahertz electric field in time for high resistivity silicon	35
4.8 Comparison of measured and simulated p-polarized terahertz electric field in time for high resistivity silicon	35
5.1 Diagram of light-matter interaction with bulk isotropic sample	38
5.2 Simulated bulk isotropic example	39
5.3 Extract complex refractive index of bulk isotropic example	40
5.4 Diagram of light-matter interaction with single layer isotropic sample	41
5.5 Simulated single layer isotropic example	42
5.6 Extracted complex refractive index for single layer isotropic example	45
5.7 Comparison of numerical spikes when sampling shifted	46
5.8 Extracted complex refractive index for single layer isotropic example with LULU	47
5.9 Error in extracted complex refractive index for constant absorption coefficient, varied real refractive index and multiple thickness errors	48
5.10 Error in extracted complex refractive index for constant real refractive index, varied absorption coefficient and multiple thickness errors	48
5.11 Error in extracted complex refractive index for transparent sample and multiple thickness errors	49
5.12 Error in extracted complex refractive index for constant absorption coefficient, varied real refractive index and multiple incident angle errors	50
5.13 Error in extracted complex refractive index for constant real refractive index, varied absorption coefficient and multiple incident angle errors	50
5.14 Error in extracted complex refractive index for transparent sample and multiple incident angle errors	51
5.15 Extracted complex refractive index for single layer isotropic with $10\ \mu\text{m}$ error	52
5.16 Extracted complex refractive index for single layer isotropic with $10\ \mu\text{m}$ error after one pass of thickness correction	53
5.17 Extracted complex refractive index for single layer isotropic with $10\ \mu\text{m}$ error after second pass of thickness correction	53
5.18 Simulated single layer isotropic example with strong resonances	56
5.19 Simulated single layer isotropic example with strong resonances with Hann window	56
5.20 Extracted complex refractive index for single layer isotropic sample with Hann window and bulk isotropic model	57
5.21 Extracted complex refractive index for single layer isotropic sample with Hann window as initial guess	57
5.22 Extracted complex refractive index for single layer isotropic samples with uniform properties	58

5.23	Extracted complex refractive index for single layer isotropic samples with resonances present	59
5.24	Diagram of light-matter interaction with single layer isotropic medium deposited on bulk isotropic sample	60
5.25	Simulated example of a single layer isotropic medium deposited on a bulk isotropic sample	61
5.26	Application of Hann window to truncate to first pulse	62
5.27	Application of Hann window to truncate to second pulse	63
5.28	Complex refractive index extracted from example of a single layer isotropic medium deposited on a bulk isotropic sample	63
5.29	Two layer ellipsometry error	64
5.30	Diagram of light-matter interaction with empty reference cuvette	65
5.31	Diagram of light-matter interaction with filled cuvette	65
5.32	Simulated example of a single layer isotropic medium deposited on a bulk isotropic sample only p-polarization	67
5.33	Application of Hann window to truncate to first pulse	68
5.34	Application of Hann window to truncate to second pulse	68
5.35	Complex refractive index extracted from example of a single layer isotropic medium deposited on a bulk isotropic sample, via the self-reference method	69
5.36	Two layer self-reference error	69
5.37	Time data for several two layer samples	70
5.38	Complex refractive index extracted from example of a single layer isotropic medium deposited on a bulk isotropic sample	71
5.39	Complex refractive index extracted from example of a single layer isotropic medium deposited on a bulk isotropic sample, via the self-reference method	71
6.1	Time-domain measurement: Silver mirror	74
6.2	FFT of measured mirror data	74
6.3	Amplitude and phase correction factors	75
6.4	Time-domain measurement: Bulk Glass, focused on pulse	76
6.5	Extract complex refractive index of bulk glass sample	76
6.6	Time-domain measurement: Single layer glass, focused on pulse and internal reflection	77
6.7	Extract complex refractive index of single layer glass sample	78
6.8	Time-domain measurement: Single layer undoped silicon, focused on pulse and internal reflections	79
6.9	Extract complex refractive index of single layer undoped silicon sample	79
6.10	Error in data extracted for undoped silicon	80
6.11	Extract absorption coefficient of single layer undoped silicon sample	80
6.12	Literature values of single layer undoped silicon sample	81
6.13	Literature values of single layer undoped silicon sample - Transmission	81

6.14	Time domain measurement of lightly doped silicon	82
6.15	Extract complex refractive index of single layer n-doped silicon sample	82
6.16	Photos of Silicon cuvette	84
6.17	Time domain cuvette measurements	84
6.18	2 layer ellipsometry extracted complex refractive index	85
6.19	Comparative n for two layer system	86
6.20	2 layer self-reference extracted complex refractive index	86
6.21	Dielectric constant error two layer system - ellipsometry	87
6.22	Dielectric constant error two layer system - self-reference	88
6.23	Comparative complex dielectric constant	88
A.1	Knife-edge measurement and fitting when only the central frequency is considered.	95
A.2	Knife-edge measurement and fitting when integrated spectrum is considered.	95
A.3	Frequency domain data at different knife-edge translations.	96
B.1	Diagram of HeNe alignment laser optical path	98
B.2	Example of centering alignment	99
B.3	Example of straightening the sample	100
C.1	Diagram depicting ray-trace of internal reflection compared to sur- face reflection	101
C.2	First section of the exiting beam path used to calculate a geometric correction for subsequent beams.	102
C.3	Second section of the exiting beam path used to calculate a geo- metric correction for subsequent beams.	103

Nomenclature

Constants

$$c = 2.998 \times 10^8 \text{ m/s}$$

$$\mu_0 = 4\pi \times 10^{-7} \text{ Wb/A m}$$

$$\epsilon_0 = 8.85419 \times 10^{-12} \text{ C}^2/\text{J m}$$

Variables

r	Coordinate	[m]
θ	Rotation angle	[rad]
q	Charge	[C]
ω	angular frequency	[rad/s]
t	time	[s]
α	absorption coefficient	[cm^{-1}]
E	Electric field	[V/m]

Chapter 1

Introduction

Terahertz (THz) radiation lies between far infrared and microwave radiation on the electromagnetic spectrum, and is generally seen as being from 0.3 – 10 THz. This area can also be seen as the border between optical and electronic wavelengths.

Studies in the THz region are of great importance, as picosecond-timescale processes are very prominent in material sciences [1–3]. Traditionally it was difficult to generate and measure THz radiation, as the sources were weak, the wavelengths are long, and ambient black body contamination obscured measured data [3]. In recent years, developments in THz sources and detectors have come a long way, making lab based measurements in this spectral region far easier [3]. THz radiation is now used in many different fields, such as the characterization of novel solids, optimization studies for coatings, detection of explosives and bio-hazardous materials and non-invasive imaging, to name but a few [3].

In previous studies conducted, it was found that conformational changes in polymers were observable in the THz spectrum [4]. It has been found that biological polymers, proteins, are identifiable in the THz region and have unique optical properties [5–7]. These materials need to be suspended in an aqueous solution to maintain their natural behaviour [5–7]. This is a limiting factor for transmission based THz spectroscopy, as THz radiation is strongly absorbed by water [8]. In previously performed measurements, high power narrow band THz sources were used as a means to overcome this limitation [5–7]. Alternatively, this limitation can be overcome by working with a reflection based system instead of a transmission system. A reference sample is needed in conventional reflection spectroscopy, as this will be required for eliminating the incident electric field from the data during calculations. This in turn introduces strenuous alignment limitations as the path length error between the sample and reference can not be larger than $10\ \mu\text{m}$ [9]. In our setup, ellipsometry is used to eliminate the need for a reference sample. Ellipsometry compares

the p- and s-polarized light reflected from a sample to determine the sample's optical properties.

Ellipsometry has generally been done in the UV, visible and near infrared spectral regions and has been implemented for use in many fields, such as analysis of thin films, semi-conductive substrates, lithographic products, polymer films, proteins, DNA, TFT films, OLEDs and optical coatings [3].

THz ellipsometers are still a very new development in the spectroscopy world, with several other groups having presented their setups in recent years [1–3]. The layout and optics of our setup are unique and during the course of this dissertation, several novel data extraction techniques will be presented, each for specific sample types.

In this research a terahertz time-domain ellipsometer has been constructed and several test measurements have been performed and analyzed. This process required the design and manufacturing of components needed for the optical setup, as well as the development of data extraction methods necessary for extracting information from measured data and simulation software for testing the aforementioned data extraction techniques.

Chapter 2

Background theory

During the course of this p spectroscopic techniques will be used to extract information about the optical properties of materials. Spectroscopy uses light to examine materials.

Light that has interacted with a material contains information about the material. The extraction of this data necessitates an understanding of how light and matter interact. Light that interacts with a dielectric material experiences absorption and changes in the phase of the wave (refraction).

2.1 Polarization

Transverse waves, such as light, oscillate perpendicular to the direction of propagation. The orientation of this oscillation is known as the polarization. Relative to the plane of incidence, the polarization can be broken up into two components, s- and p-polarization, where s- refers to the component of the electric field oscillating perpendicular to the plane of incidence and p- refers to the component of the electric field oscillating parallel to the plane of incidence.

2.2 Complex refractive index

The complex refractive index determines how light propagates through a medium. The complex refractive index consists of two components, the real refractive index, n , and the extinction coefficient, κ .

$$\tilde{n} = n - i\kappa \quad (2.2.1)$$

Light traveling through a dielectric medium propagates slower compared to vacuum. The propagation speed is inversely proportional to the real refractive index of the medium. The electric field also undergoes attenuation as it propagates through the medium. This attenuation is determined by the extinction coefficient of the material.

$$E(t) = E_0 e^{-i(\tilde{k}x - 2\pi ft)} \quad (2.2.2)$$

$$\tilde{k} = \frac{2\pi f \tilde{n}}{c} \quad (2.2.3)$$

For free space:

$$\tilde{n} = 1 \quad (2.2.4)$$

$$E_i(t) = E_0 e^{-i2\pi f(\frac{d}{c} - t)} \quad (2.2.5)$$

while, for a dielectric medium:

$$\tilde{n} = n - i\kappa \quad (2.2.6)$$

$$E_t(t) = E_0 e^{-i2\pi f(\frac{nd}{c} - t)} e^{-2\pi \frac{f\kappa d}{c}} \quad (2.2.7)$$

In equation 2.2.7, $E_t(t)$ is the electric field after having traveled through a dielectric medium of thickness d ; $E_i(t)$ is the electric field which has propagated a distance, d , through free space; n is the real refractive index of the dielectric medium, and κ is the extinction coefficient of the medium. The extinction coefficient, κ , is related to the absorption coefficient, α by the following relationship:

$$\kappa = \frac{\alpha c}{4\pi f} \quad (2.2.8)$$

The attenuation and phase delay introduced by traveling through a dielectric medium is derived from equation 2.2.7 and is compounded into a single variable, A .

$$A = e^{-i2\pi f \frac{\tilde{n}d}{c}} \quad (2.2.9)$$

2.3 Fresnel Equations

Light incident on the interface between two materials with different refractive indexes will undergo reflection and transmission at the interface. The ratio of the electric field that is reflected and transmitted is described by the Fresnel equations. The ratio can be reduced to reflection and transmission coefficients. These coefficients are polarization dependent, with different coefficients for the p- and s-polarization [10].

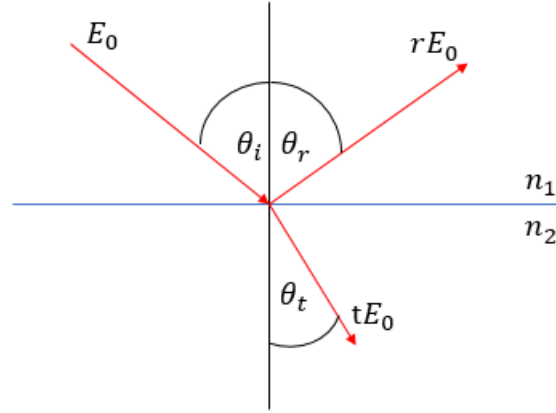


Figure 2.1: Diagram depicting the interaction of light at the interface between two media with different refractive indexes. A fraction of incident light is reflected and a fraction is transmitted into the second medium.

$$r_p = \frac{n_1 \cos \theta_t - n_2 \cos \theta_i}{n_1 \cos \theta_t + n_2 \cos \theta_i} \quad (2.3.1)$$

$$r_s = \frac{n_1 \cos \theta_i - n_2 \cos \theta_t}{n_1 \cos \theta_i + n_2 \cos \theta_t} \quad (2.3.2)$$

$$t_p = \frac{2n_1 \cos \theta_i}{n_1 \cos \theta_t + n_2 \cos \theta_i} \quad (2.3.3)$$

$$t_s = \frac{2n_1 \cos \theta_i}{n_1 \cos \theta_i + n_2 \cos \theta_t} \quad (2.3.4)$$

In equations 2.3.1 and 2.3.3 r_p and t_p are the reflection and transmission coefficients for the p-polarized component of the the incident electric field and r_s and t_s are the reflection and transmission coefficients for the s-polarized component of the the incident electric field. The real refractive index of the first medium is represented by n_1 and the real refractive index of the second medium is represented by n_2 , while θ_i represents the angle at which the wave is incident on the interface between the two media and θ_t represents the angle at which the wave refracts through the interface between the two media.

From the Fresnel equations (equations 2.3.1 - 2.3.4) it is found that at a specific angle of incidence, for a given material the reflection coefficient for p-polarized light becomes 0 while the reflection coefficient for s-polarized light is non-zero. Thus there will be a loss to s-polarized light transmitted through this material, but not p-polarized light. This angle is known as Brewster's angle and can be easily calculated from equation 2.3.1,

$$\tan \theta_B = \frac{n_2}{n_1} \quad (2.3.5)$$

where θ_B is Brewster's angle [11].

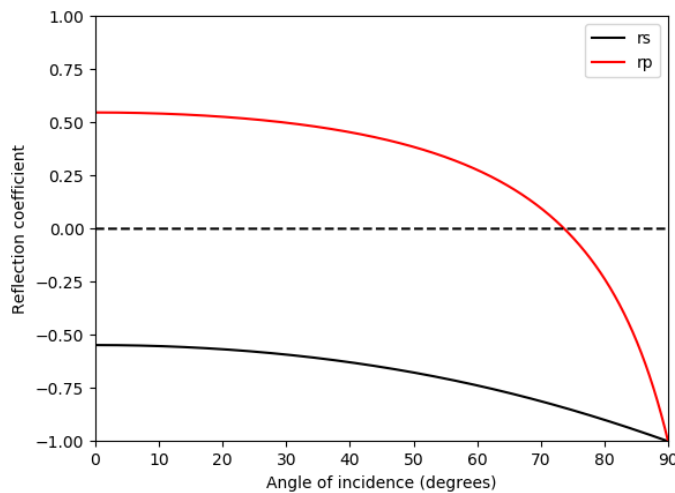


Figure 2.2: The real part of the s- and p-reflection coefficients for high resistivity silicon as a function of the angle of incidence.

It should be noted that, in figure 2.2, where the reflection coefficients are negative, it indicates that the reflected electric field will undergo a π -phase shift, which can be seen in the time domain as an inversion of the electric field about the time-axis.

The Fresnel equations still hold true when the complex refractive index is considered, as apposed to the real refractive index [10]:

$$\tilde{r}_p = \frac{\tilde{n}_1 \cos \tilde{\theta}_t - \tilde{n}_2 \cos \tilde{\theta}_i}{\tilde{n}_1 \cos \tilde{\theta}_t + \tilde{n}_2 \cos \tilde{\theta}_i} \quad (2.3.6)$$

$$\tilde{r}_s = \frac{\tilde{n}_1 \cos \tilde{\theta}_i - \tilde{n}_2 \cos \tilde{\theta}_t}{\tilde{n}_1 \cos \tilde{\theta}_i + \tilde{n}_2 \cos \tilde{\theta}_t} \quad (2.3.7)$$

$$\tilde{t}_p = \frac{2\tilde{n}_1 \cos \tilde{\theta}_i}{\tilde{n}_1 \cos \tilde{\theta}_t + \tilde{n}_2 \cos \tilde{\theta}_i} \quad (2.3.8)$$

$$\tilde{t}_s = \frac{2\tilde{n}_1 \cos \tilde{\theta}_i}{\tilde{n}_1 \cos \tilde{\theta}_i + \tilde{n}_2 \cos \tilde{\theta}_t} \quad (2.3.9)$$

In equations 2.3.6 and 2.3.8 \tilde{r}_p and \tilde{t}_p are the reflection and transmission coefficients for the p-polarized component of the the incident electric field and \tilde{r}_s and \tilde{t}_s are the reflection and transmission coefficients for the s-polarized component of the the incident electric field. The complex refractive index of

the first medium is represented by \tilde{n}_1 and the complex refractive index of the second medium is represented by \tilde{n}_2 , while $\tilde{\theta}_i$ represents the angle at which the wave is incident on the interface between the two media and $\tilde{\theta}_t$ represents the angle at which the wave refracts through the interface between the two media, but no longer directly represents the angle of propagation through the medium [12].

2.4 Snell's Laws

Snell's laws describe how the direction of propagation changes for light at the interface between two dielectric media. These laws relate the angle of incidence (θ_I), the angle of reflection (θ_R) and the angle of transmission (θ_T).

Snell's 1'st law states that the incident, reflected and transmitted wave vectors all lie in the same plane. This plane is known as the plane of incidence.

Snell's 2'nd law describes that the angle at which light reflects off the surface of a dielectric medium is equal to the angle of incidence, as measured relative to the surface normal.

Snell's 2'nd law:

$$\theta_R = \theta_I \quad (2.4.1)$$

Snell's 3'rd law describes how light transmitted through the interface between two dielectric media with different refractive indexes undergoes a change in propagation direction. The transmitted angle is dependent on the ratio between the refractive indexes of the two materials and the angle at which light is incident on the interface.

Snell's 3'rd law:

$$n_1 \sin \theta_I = n_2 \sin \theta_T \quad (2.4.2)$$

$$\theta_T = \sin^{-1} \left(\frac{n_1}{n_2} \sin \theta_I \right) \quad (2.4.3)$$

In equation 2.4.3 the real refractive index is used. Equation 2.4.3 does hold true if the complex refractive index is used instead [12].

$$n_1 \sin \theta_I = \tilde{n}_2 \sin \tilde{\theta}_T \quad (2.4.4)$$

$$\tilde{\theta}_T = \sin^{-1} \left(\frac{n_1}{\tilde{n}_2} \sin \theta_I \right) \quad (2.4.5)$$

In equation 2.4.5 the complex angle of refraction, $\tilde{\theta}_T$, does not equate to the angle of propagation. In this case the angle of propagation can be calculated by the following equation [12]:

$$\sin^2 \theta_{Tprop} = \frac{1}{2} \left[\left(1 + \frac{n_1^2 \sin^2 \theta_I}{n_2^2 + \kappa_2^2} \right) - \sqrt{\left(1 + \frac{n_1^2 \sin^2 \theta_I}{n_2^2 + \kappa_2^2} \right)^2 - \frac{4n_2^2 n_1^2 \sin^2 \theta_I}{(n_2^2 + \kappa_2^2)^2}} \right] \quad (2.4.6)$$

2.5 Ellipsometry

Ellipsometry is a spectroscopic technique which is used to analyze materials by the polarization based changes they introduce to light reflected from them.

As shown in section 2.3, the reflection and transmission coefficients for an electric field incident on a material is different, depending on whether the light is s- or p-polarized.

Thus, by comparing the s- and p-polarized light reflected from a material, it is possible to extract information about the material's optical properties.

As a basic example of this, when a dielectric sample, which does not depolarize incident light and does not allow for observable internal reflection, is considered, the complex dielectric constant, $\tilde{\epsilon}$, and thus the complex refractive index, \tilde{n} , of the material, can be extracted by comparing the s- and p-polarized electric fields reflected from this material [13].

$$\rho = \frac{\tilde{r}_p E_{0p}}{\tilde{r}_s E_{0s}} = \frac{\tilde{r}_p}{\tilde{r}_s} \quad (2.5.1)$$

$$\tilde{\epsilon} = \sin^2 \theta \left[1 + \left(\frac{1 - \rho}{1 + \rho} \right)^2 \tan^2 \theta \right] \quad (2.5.2)$$

$$\tilde{n} = \sqrt{\tilde{\epsilon}} \quad (2.5.3)$$

In equation 2.5.1, it is assumed that $E_{0p} = E_{0s} = E_0$. By doing so, E_0 is eliminated from the equation and thus the need to have prior knowledge of the incident electric field is removed. Thus, the complex dielectric constant of the sample can be extracted without the need need for a separate measurement to determine the incident electric field, E_0 .

A more in-depth look at our implementation of ellipsometry to extract optical information from measured data can be found in chapter 5.

Chapter 3

Experimental setup

Ellipsometry is a powerful spectroscopic technique that is especially useful for optically analyzing thin film samples and optically dense (strongly absorbing) materials [3]. Within the THz spectral region this technique will be especially useful for examining biological samples in an aqueous environment, which can not be done easily using THz transmission measurements, due to strong absorption of water in this spectral region [8]. No commercial THz ellipsometers exist, thus performing THz ellipsometry measurements necessitates the design, construction and testing of a custom THz ellipsometry setup. This included the design and manufacture of several components, which will be expanded upon in the following sections.

3.1 Terahertz generation and detection

A large portion of black body radiation at room temperature is within the THz region (at 300 K, for 0.8 THz the black body energy density is 117.7 W m^{-3}) [14], thus there is a large background within this spectral region. A coherent source is required to allow for measurements in this high background environment. Several coherent THz sources, both narrow and broadband, are currently available, such as: non-linear crystals, photo-conductive antennae, quantum cascade lasers, and directly pumped gas lasers [15–18]. There are also several detector options for the THz region. The most common of which are opto-electric crystals, photo-conductive antennae, Schottky diodes and bolometers [15–17].

Our setup uses photo-conductive antennae for both detection and generation. Photo-conductive antennae are broadband coherent THz sources, which are also capable of measuring THz electric fields in the time domain [17]. In our setup we use photo-conductive antennae, and will hence expand upon them in the coming subsections.

3.1.1 Photo-conductive antennae as THz emitter

A photo-conductive antenna is a dipole antenna that is printed on a photo-conductive substrate. Photo-conductive substrates are semi-conductor materials, which normally have a very high electrical resistance. When light with a photon energy above the band gap is absorbed by the semiconductor, the resistance decreases by several orders of magnitude, effectively changing the material from an insulator to a conductor [17].

If the semiconductor material contains many defects, as is the case with low temperature grown gallium arsenide (LT-GaAs), the lifetime of the excited state is extremely short (<ps) [17]. If the incident light pulse is a femtosecond laser pulse, the semiconductor switches from an insulator to a conductor and back again in an extremely short (<ps) time [17].

If the dipole antenna printed on the photo-conductive substrate is supplied with a DC bias voltage, a short current pulse will oscillate in the antenna under femtosecond laser illumination.

The current in the circuit is dependent on the applied voltage, the excitation lifetime of the generated charge carriers, the momentum relaxation time of the generated charge carriers and the amount of charge carriers generated in the substrate. The single cycle current oscillation produces a single cycle oscillation THz pulse that is emitted from the antenna. This THz pulse is dependent on the oscillating current and the size of the dipole and is described by the following equation [17]:

$$E(r, t) = \frac{l_e}{4\pi\epsilon_0 c^2 r} \frac{\partial J(t)}{\partial t} \sin \theta \quad (3.1.1)$$

$$J(t) = \frac{e\tau_s}{m} E_{DC} I_{opt}^0 \int_0^\infty e^{-(t-t')^2/\tau_p^2 - t'/\tau_c} [1 - e^{-t'/\tau_s}] dt'. \quad (3.1.2)$$

where $J(t)$ is the current in the dipole, l_e is the effective length of the dipole, i.e. the length of the laser gap between the two halves of the dipole antenna, r is the distance from the emitter to the point of observation and θ is the polar observation angle for the emission from the dipole. For the system we will be focusing on during this dissertation, θ is taken to be 90° , as the optical path is perpendicular to the emitter. The carrier lifetime of the substrate is represented by τ_c , τ_s is the momentum relaxation time of the substrate, m is the effective mass of the charge carriers, e is the charge of an electron and E_{DC} is the applied bias field. A Gaussian pump pulse with a temporal half-width of $2\sqrt{\ln 2}\tau_p$ and peak intensity of I_{opt}^0 is used [17].

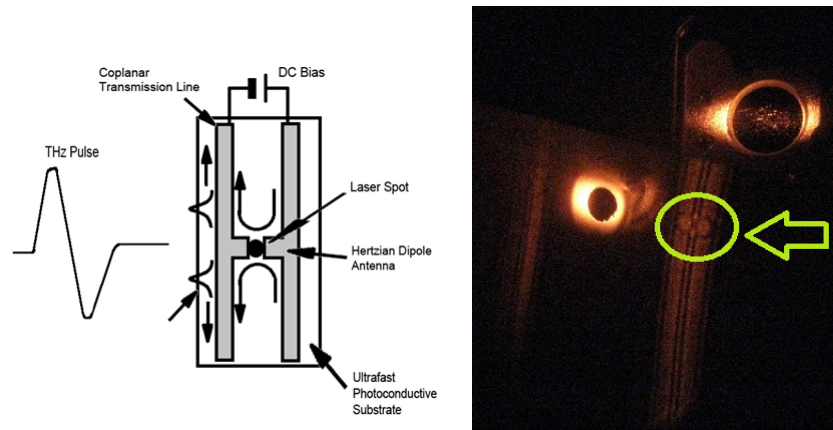


Figure 3.1: (a) is a diagram of a photo-conductive antenna [17]. (b) is a magnified image of a photo-conductive antenna used in our setup, where the circle indicates the antenna on the image.

3.1.2 Photo-conductive antennae as THz receiver

A photo-conductive antennae is also used for the detection of THz radiation in our setup. THz detection via a photo-conductive antenna works in a similar fashion to THz emission via a photo-conductive antenna (as discussed in section 3.1.1) with the difference that the antenna is not biased by a DC voltage. When a femtosecond laser pulse is incident on the dipole, charge carriers in the substrate are excited to the conduction band. A THz electric field incident on the antenna accelerates these generated charge carriers, thus producing a current that can be measured. The induced current is proportional to the incident electric field [17], as such by measuring the current, the electric field will be determined.

The induced electric field is represented by the following equation [17]:

$$J(t) = e\mu \int_{-\infty}^{\infty} E(t')N(t' - t)dt' \quad (3.1.3)$$

where $E(t')$ is the incident THz electric field, $N(t')$ is the number of excited charge carriers in the photo-conductive substrate created by the incident femtosecond laser pulse, e is the elementary electric charge and μ the electron mobility.

The generated current only represents a small portion of the incident THz electric field. The generated current is a function of the temporal overlap between the femtosecond laser pulse (fs-pulse) and THz electric field incident on the receiving antenna, as can be seen from equation 3.1.3. The arrival time of the THz electric field at the receiving antenna can be changed by implementing

an optical delay line in the path of the fs-pulse to the transmitting antenna. Altering the arrival time of the THz electric field while keeping the beam path of the fs-pulse to the receiving antenna constant, will cause the temporal overlap of the two pulses to be changed; thus a different temporal slice of the THz electric field will be represented by the generated current. Iterative changes to the optical delay allows for the entire THz electric field to be mapped in time.

The current induced in the antenna circuit is amplified via frequency based lock-in amplification, which is aided by using the TTL output of the lock-in amplifier for the DC-bias of the the transmitting antenna. This amplified current is measured by use of a data acquisition (DAQ) device.

3.2 Brewster stacks

Ellipsometric measurements require the electric field incident on the sample to have a pure polarization state, as it allows for the interpretation of polarization dependent changes induced by the sample to the electric field.

The photo-conductive antennae in our setup are structured such that they emit predominantly horizontally polarized light and, similarly, the detector antenna is more sensitive for horizontally polarized light. Hence it would be preferable to work with a pure horizontally polarized electric field.

Two Brewster stacks are implemented in our setup; one before and one after the sample. These polarisers clean up the polarization of the light incident on the sample and reflected from the sample.

Several commercial THz broadband polarisers exist, but these offer non-flat degrees of polarization and/ or transmittance in the spectral range this system will be operating in [19].

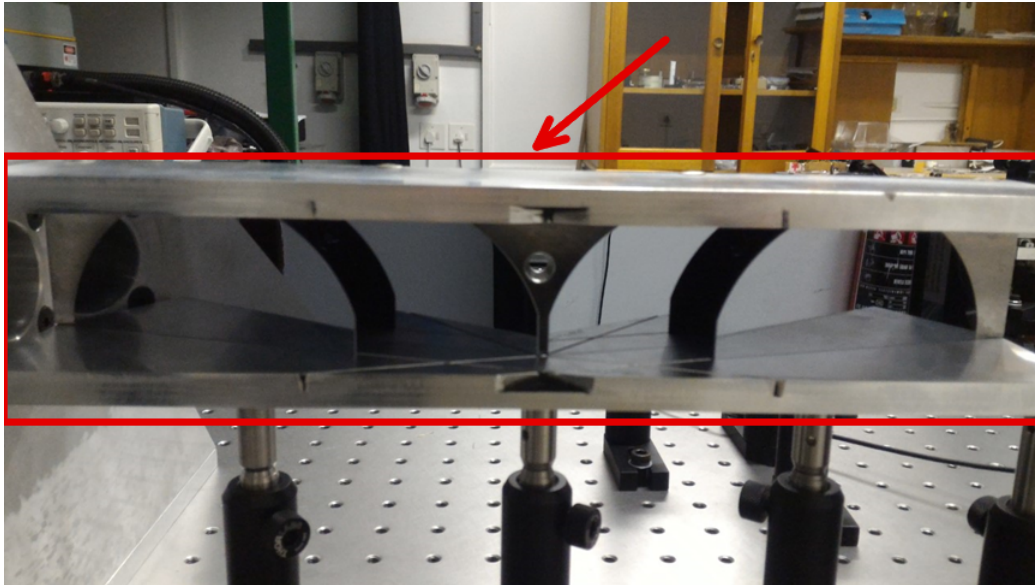


Figure 3.2: A photo of a high resistivity silicon based Brewster stack we manufactured for use in our setup.

As discussed in section 2.3, light incident on a medium at Brewster's angle undergoes reflection based losses to its s-polarized component, but not its p-polarized component. Implementing multiple layers of a substrate at Brewster's angle will hence effectively remove s-polarized light and only leave p-polarized light from an incident source. This type of structure is known as a Brewster stack.

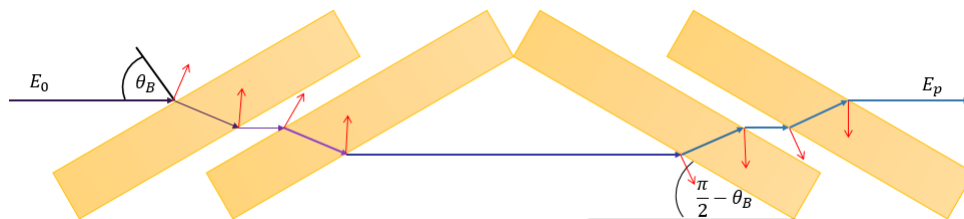


Figure 3.3: A diagram of a high resistivity silicon based Brewster stack we designed for use in our setup. An electric field E_0 is incident on the Brewster stack, depicted as a black arrow. The red lines represent the s-polarized light reflected at each interface, $r_s E_{\text{incident}}$. The blue arrow exiting the system represents the direction of the wave vector of the p-polarised electric field, E_p , leaving the Brewster stack.

It should be noted that the Brewster stack, as depicted in figure 3.3, is constructed anti-symmetrically. As light propagates through the medium, it is displaced from its initial path due to the change in propagation direction as described by equation 2.4.3. An anti-symmetric unit of the medium is used for every initial unit to correct this walk-off, hence the electric field exiting the Brewster stack will propagate along the initial path.

The material implemented in our Brewster stack is high resistivity silicon, due to its high refractive index and low absorption coefficient in the THz region. High resistivity silicon has a refractive index of 3.4177 and an absorption coefficient of 0.03 cm^{-1} in the THz region [20–22]. The high refractive index of the material leads to the s-transmission coefficient (equation 2.3.9) being relatively low at Brewster's angle ($t_{p_{01}} * t_{p_{10}} = 1.0$ and $t_{s_{01}} * t_{s_{10}} = 0.29$), hence fewer silicon layers are required in order to achieve a highly pure polarization state. In our Brewster stack four layers are used, thereby removing 99.29% of the initial s-polarized electric field. The low absorption coefficient leads to low losses to the pulse as a whole. A photo of a Brewster stack we developed and manufactured can be seen in figure 3.2.

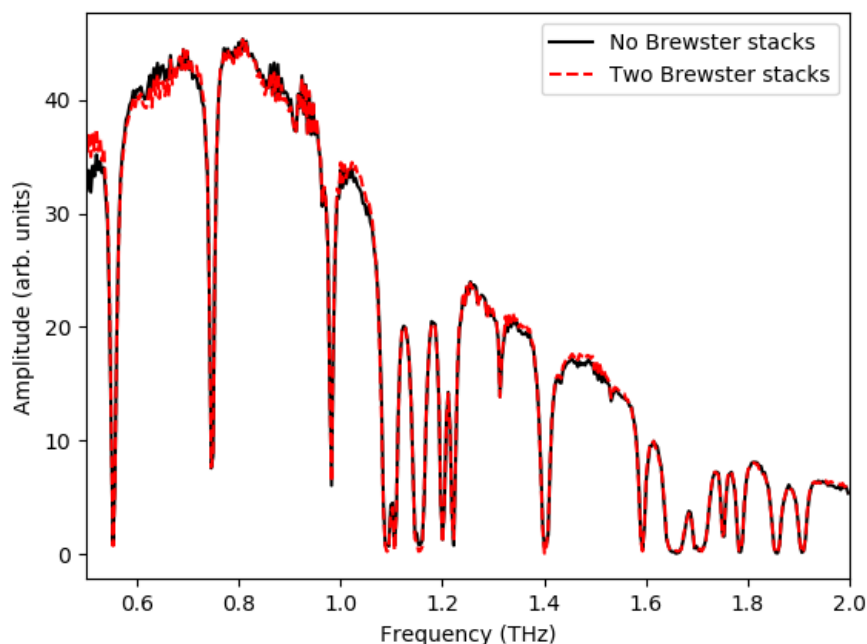


Figure 3.4: THz spectral amplitude measured with a silver mirror as the sample with with and without the Brewster stacks present in the setup. These measurements were performed in normal atmospheric conditions, with 51% humidity present at 292K.

The photo-conductive antenna used as THz sources in our setup are highly polarized, as can be seen by how little effect the introduction of Brewster stacks have on our measured THz spectral amplitude, as displayed in figure 3.4.

For the spectral region we will be working in the refractive index of undoped silicon is effectively frequency independent [20–22], and hence Brewster’s angle is also frequency independent, thus making this an ideal polarizing material for our spectral range.

In our system we will use two of these polarisers. In order to determine the effectiveness of these polarisers, two measurements were performed. One with both polarisers orientated to transmit maximally for the horizontal plane (Co-linear) and one with the first polariser orientated to transmit maximally in the horizontal plane and the second polariser rotated to transmit maximally in the vertical plane (Orthogonal). The Fourier transformed spectra for these two measurements are seen in figure 3.5.

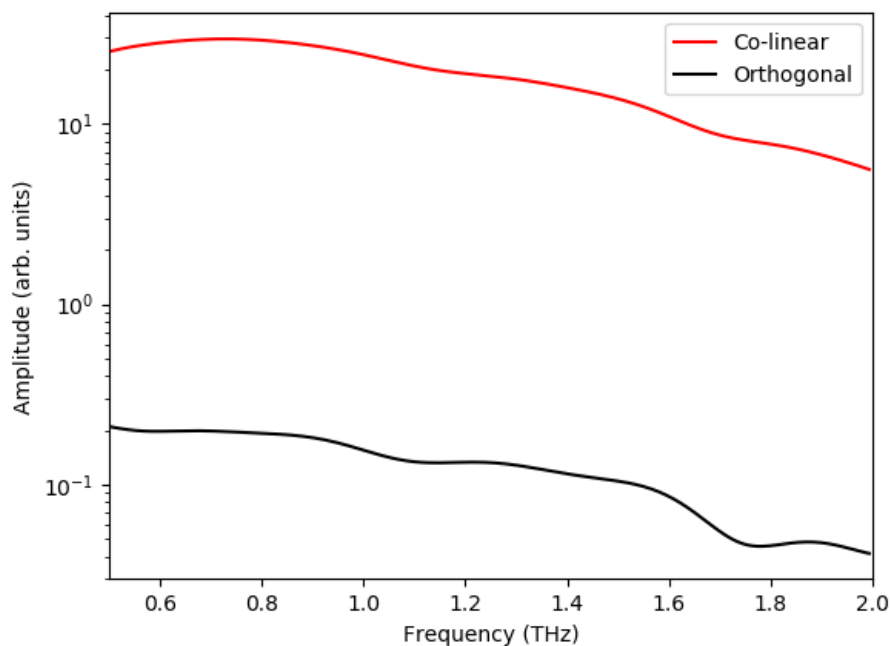


Figure 3.5: THz spectral amplitude measured with a silver mirror as the sample with the Brewster stacks and a co-linear and orthogonal configuration.

By multiplying the THz electric field with its complex conjugate, the intensity of the electric field is calculated, which can be seen in figure 3.6.

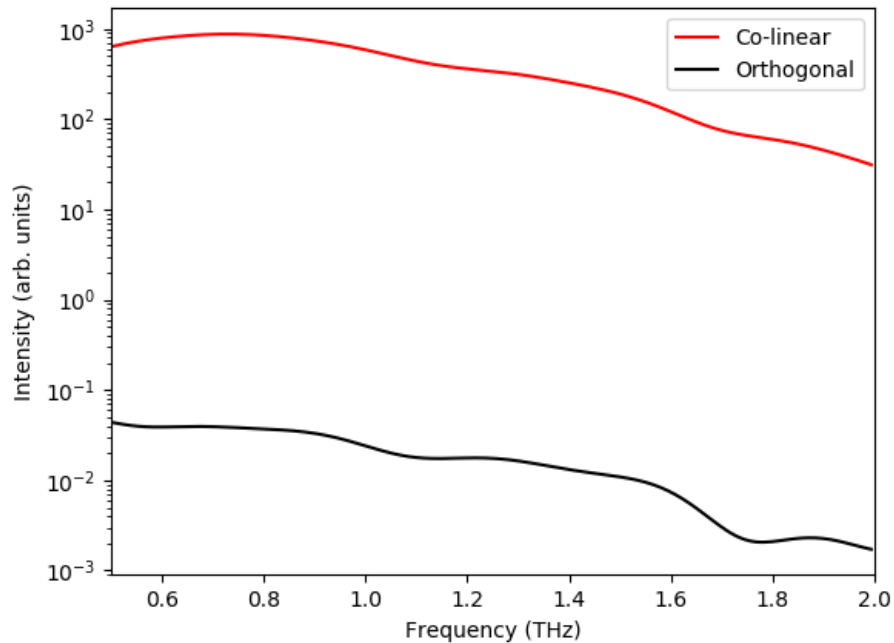


Figure 3.6: Intensity of THz spectral amplitude measured with a silver mirror as the sample with the Brewster stacks and a co-linear and orthogonal configuration.

From the intensities in figure 3.6, the extinction ratio, which is the ratio between p- and s-polarized light transmitted through the optical element, and the degree of polarization, which is a measure of how pure the polarization state of the light is after the optical element, can be calculated.

$$P = \frac{I_1 - I_2}{I_1 + I_2} * 100 \quad (3.2.1)$$

$$\rho_p = \frac{I_2}{I_1} \quad (3.2.2)$$

where P is the degree of polarization, ρ_p is the extinction ratio, I_1 is the co-linear intensity and I_2 is the orthogonal intensity [23].

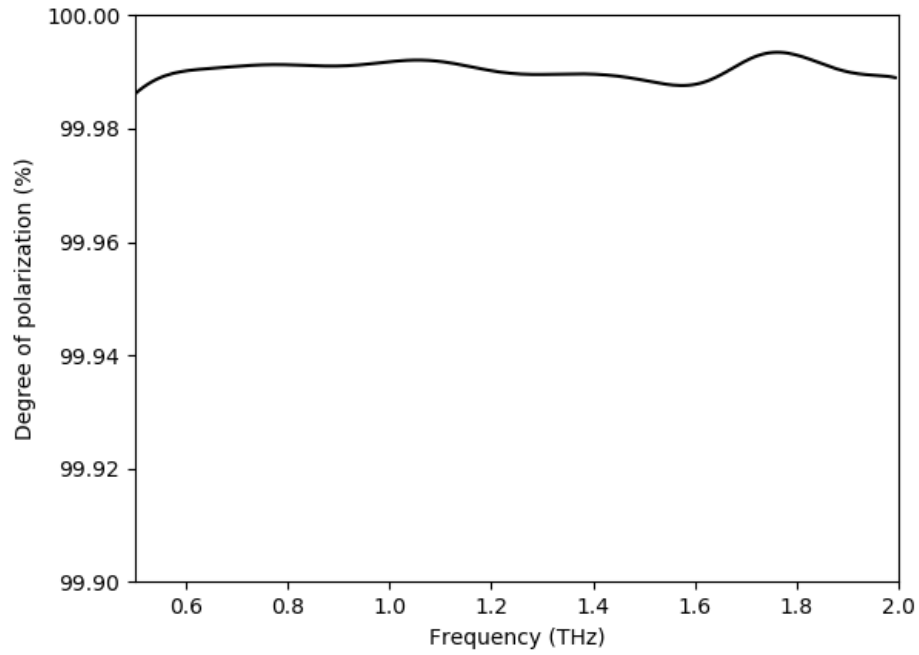


Figure 3.7: Degree of polarization measured for the silicon Brewster stacks we manufactured and used in our setup.

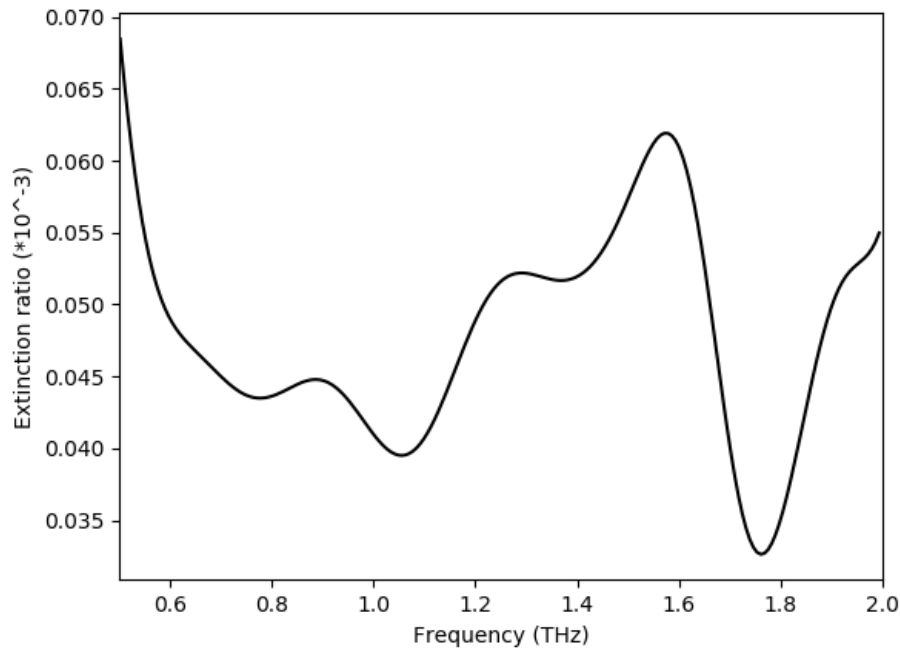


Figure 3.8: Extinction ratio measured for the silicon Brewster stacks we manufactured and used in the setup.

From figure 3.7 and figure 3.8 it can be seen that these polarisers have phenomenal performance, especially when compared to commercially available polarisers [19], as seen in figure 3.9.

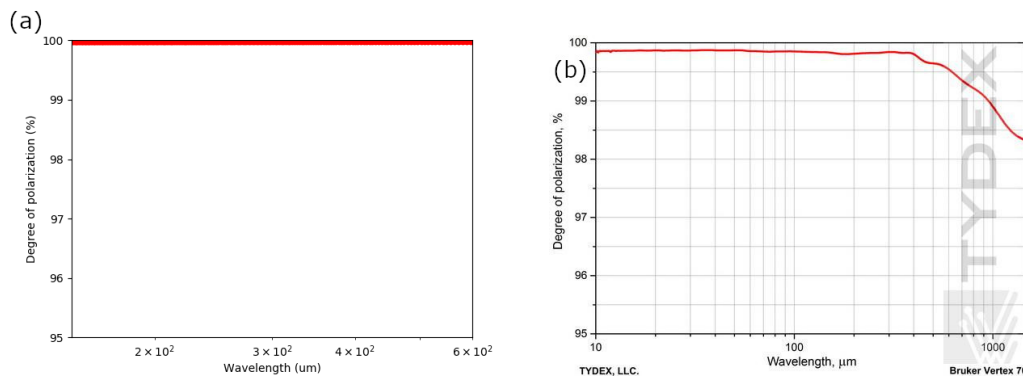


Figure 3.9: (a) The degree of polarization measured for our Brewster stacks. (b) The degree of polarization of a commercial polypropylene wire-grid polariser [19].

3.3 Rotational mount

Ellipsometry requires for both the s- and p-polarized electric fields reflected from a sample to be measured. Commercial THz achromatic half-wave plates, which would normally be used to rotate the polarization of broadband radiation, are currently quite inefficient ($< 30\%$ transmission) and are not suitable for our entire spectral range [24]. A rotational mount was designed to rotate the sample, which changes the plane of incidence of the sample and hence changes the polarization of the electric field incident on the sample. A CAD drawing of the rotational mount with the optical setup equipped is presented in figure 3.10.

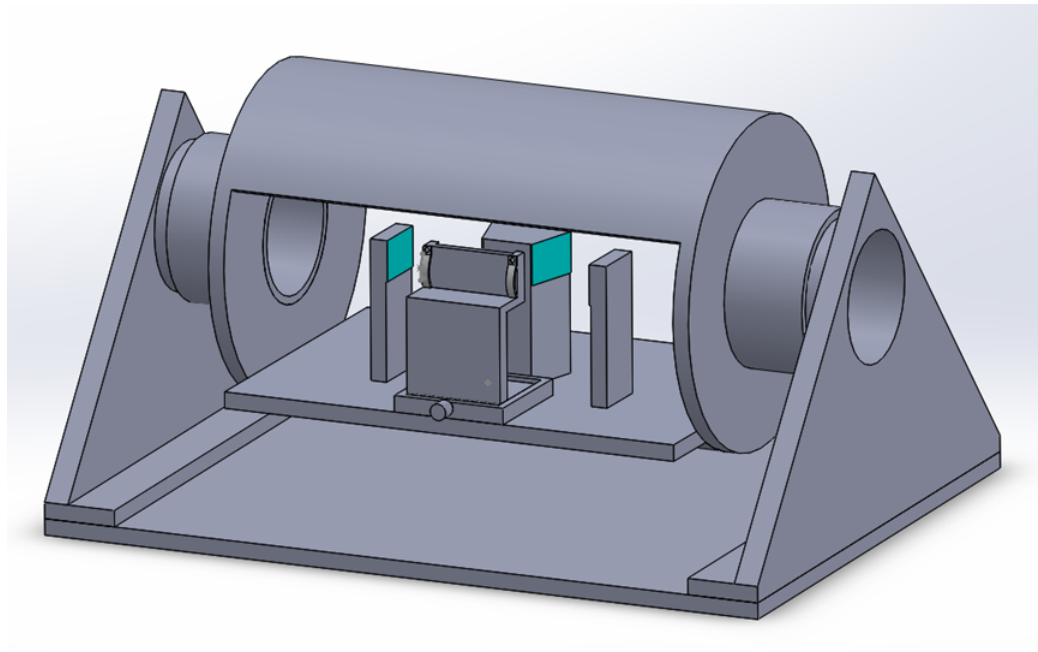


Figure 3.10: A CAD drawing of a rotational sample mount to allow for s- and p-polarization THz measurements.

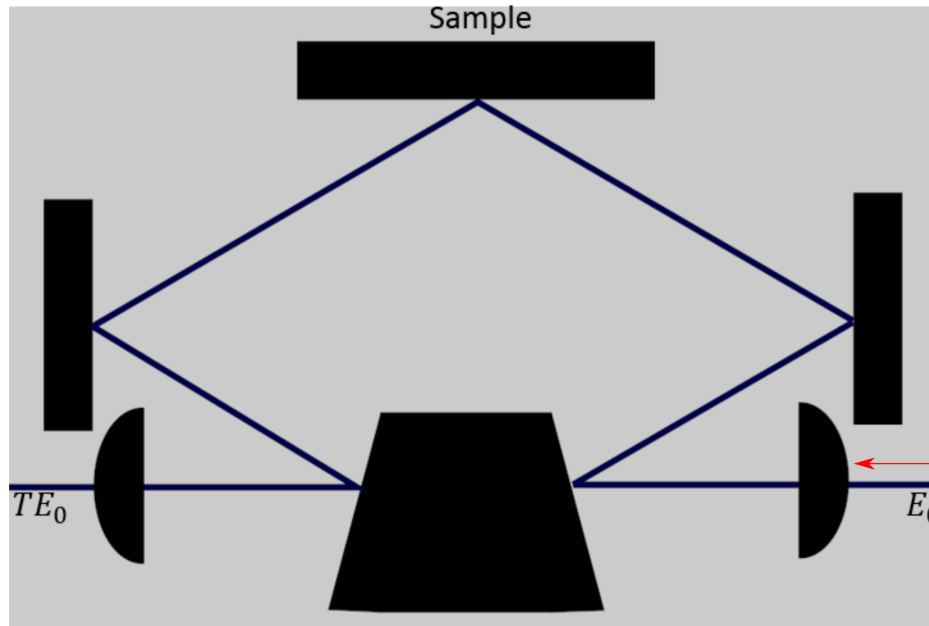


Figure 3.11: A diagram of a THz optical path designed for reflection based measurements. The transfer function for the electric field, E_0 , propagated through the given optical path is represented by T . T comprises of the effects of reflecting off the mirrors, propagating through the lenses and interacting with the sample.

Figure 3.11 represents the optical path inside the rotational mount. When the optical path (plane of incidence) is horizontal, the horizontally polarized incident electric field, E_0 , is parallel to the plane of incidence with respect to the sample (p-polarized). Rotating the optical setup by 90° changes the plane of incidence to the vertical plane, thus, from the frame of reference of the optical path, the electric field is s-polarized. In the frame of reference of the rest of the optical setup, outside of the rotated components, the polarization of the electric field did not change, thus the polarizing components will not need to be adjusted. This is important since rotating the Brewster stacks could easily introduce alignment errors, and the response of the detector can be polarization dependent.

When compared to the approaches of other groups [1; 25] the use of the rotational mount simplifies data analysis, by effectively eliminating the polarization dependence of the detector. The rotational mount also results in a higher signal to noise ratio, when compared to 45° rotated antennae [1; 25], as the full amplitude of the electric field will be used for both the s- and p-polarized electric field measurements. A potential downside to this design is that during rotation, the system might miss-align, as the bearing could shift along its axis. This design also limits changes to the layout of the terahertz

optical path, as a new mounting plate will be needed if the angle of incidence requires noticeable change.

3.4 Layout

THz time-domain ellipsometric measurements require a suitable optical setup for measurements to be performed. This optical setup can be viewed as two distinct components, the optical setup for the THz electric field and the optical setup for the femtosecond laser pulse used to excite the photo-conductive substrate of the antennae. The full layout is depicted in figure 3.12.

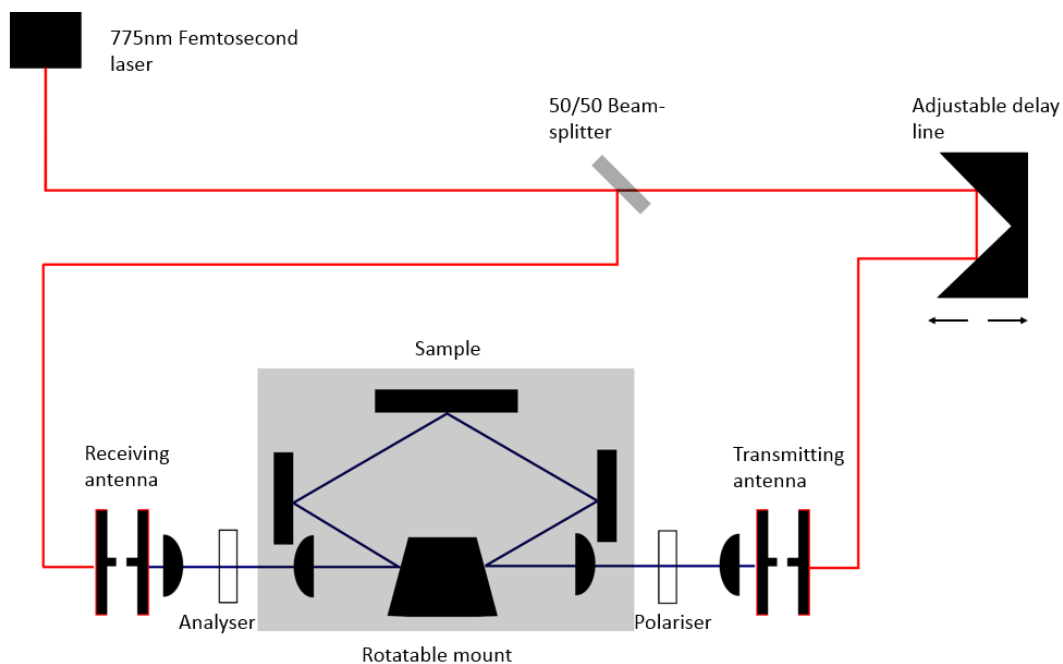


Figure 3.12: A diagram of an optical setup designed for time-domain THz ellipsometry measurements.

The femtosecond laser path includes a beam-splitter to divide the femtosecond laser pulse onto two paths, one to the emitting antenna and one to the receiving antenna. The path to the emitting antenna includes an optical delay line. This delay line is used to change at which time the THz electric field is generated relative to when the receiving antenna is excited. The temporal overlap between the femtosecond laser pulse and the THz pulse at the receiving antenna is changed to allow for the THz electric field to be measured in time, as discussed in section 3.1.2.

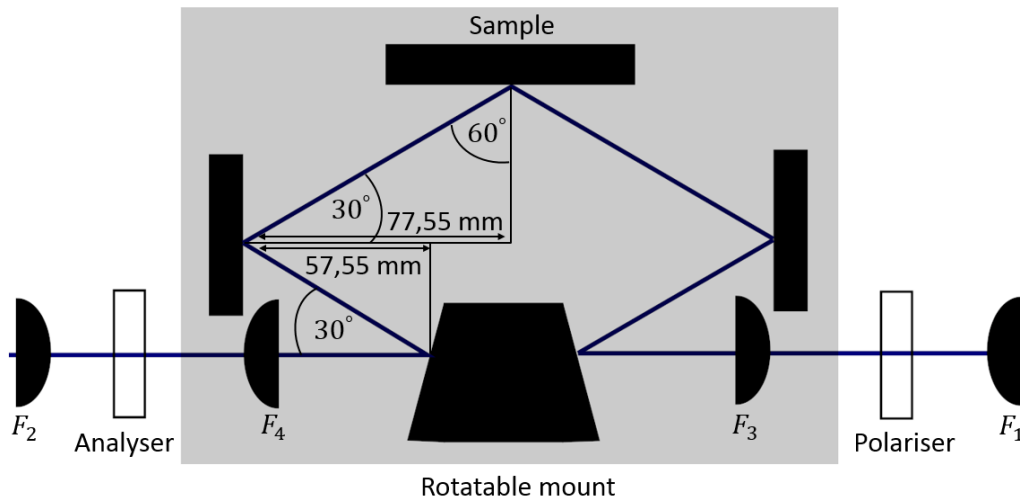


Figure 3.13: A diagram of the THz specific component of the optical setup depicted in figure 3.12.

The THz path, as seen in figure 3.13, is designed for ellipsometry measurements. The closer the angle of incidence is to the Brewster angle of a sample, the smaller the ratio is between the reflection coefficients for p- and s-polarized electric fields (equation 2.3.7 and 2.3.6). The accuracy to which the optical parameters for a given material can be extracted correlates to the magnitude of the ratio between the p- and s- reflections [3], with smaller absolute ratio values expected to yield more accurate results. Our system is designed with an angle of incidence of 60° , since this results in a sufficiently small ratio between r_p and r_s for a large variety of samples, as can be seen from figures 3.14 and 3.15. For an angle of incidence of 60° and refractive indexes between 1.2 and 4.5, an absolute reflection coefficient ratio ($\frac{r_p}{r_s}$) < 0.5 is expected, as can be seen in figure 3.15. This range is of interest as it includes semi-conductive substrates (refractive index: 3 – 4 [20]), biological materials (refractive index: 1.5 – 3.0 [7; 26; 27]), polymers (refractive index: 1.2 – 1.7 [28–30]) and water (refractive index: 2.13 [31]). Two mirrors, mounted on the rotational mount as discussed in section 3.3, are used to achieve this angle of incidence. Brewster stacks are implemented as both the polarisor and the analyzer. The polarisor is used to select the polarization state for the electric field incident on the sample. A pure polarization state for the THz electric field incident on the receiving antenna is achieved via the analyzer.

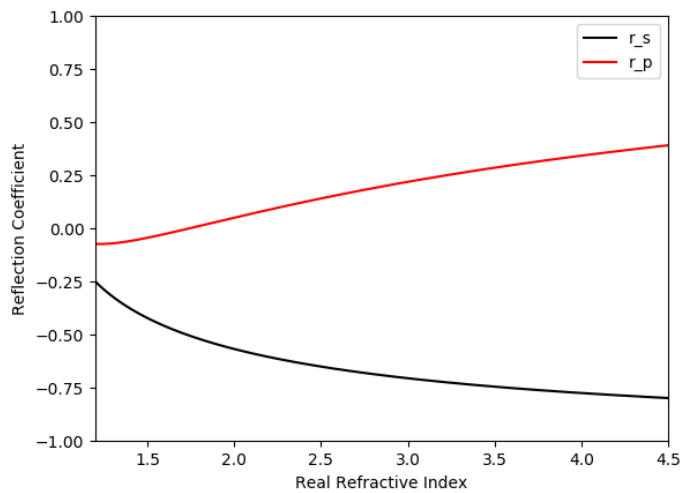


Figure 3.14: The real reflection coefficients for s- and p-polarized light reflected at 60° plotted over refractive index.

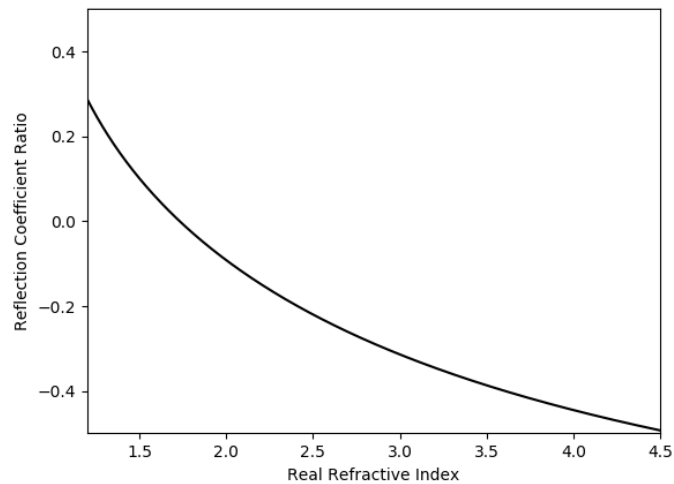


Figure 3.15: The ratio between the real reflection coefficients for p- and s-polarized light reflected at 60° plotted over refractive index.

As indicated on figure 3.13, the THz optical path contains four lenses. A lens, F_1 , with a focal length of 45 mm is used to collimate the radiation from the transmitting antenna. A lens, F_2 , with focal length of 45 mm, is used to focus the radiation on the receiving antenna. Two lenses, F_3 and F_4 , with focal

lengths of 200 mm, are found on each side of the rotational mount. The lens, F_3 , is used to focus light on the sample and the second, F_4 , is used to collimate the light reflected from the sample before it leaves the rotational mount. Lenses with focal length of 200 mm were used so as to not focus strongly on the sample, there by reducing the negative effects that can be introduced by focusing on the sample, such as exacerbating miss-alignments and the effects of the sample not being in the focus of the lenses [3]. By lightly focusing on the sample, a smaller beam spot is incident on the sample, thus expanding the options of what samples can be examined by lowering the dimensional restrictions the beam size imposes on the sample. This is especially relevant when windowed cuvettes are used, as it is best to minimize or eliminate radiation reflected from the interface between the window and the surrounding cuvette material.

The beam size of our system, for the central frequency, as measured by knife-edge (for more information see Appendix A), is $11.67 (\pm 0.02)$ mm ($\frac{1}{e^2}$ diameter) after F_1 . The central wavelength of our system is approximately $375 \mu\text{m}$.

The spot size at the focus of the 200 mm focal length lenses and the depth of focus, the distance over which the beam is considered to effectively be in focus, can be calculated from the following equations [32]:

$$2 * W_0 = \frac{4 \lambda F}{\pi D} \quad (3.4.1)$$

$$DOF = \frac{8 \lambda}{\pi} \left(\frac{F}{D} \right)^2 \quad (3.4.2)$$

where W_0 is the beam waist at the focus, F is the focal length of the lens, D is the diameter of the beam incident on the lens and DOF is the depth of focus. For a collimated beam with a diameter of $11.67 (\pm 0.02)$ mm, it is found that the spot size at the focus is $8.18 (\pm 0.02)$ mm and the depth of focus is $280 (\pm 0.5)$ mm.

It is important that we have a long depth of focus, as this will allow for internal reflections from samples to be accurately measured. The depth of focus should not be the limiting factor for the thickness of samples we can examine in our system, as 280 mm should be far longer than the path length of light traveling through a sample that can be mounted in our system.

3.5 Nitrogen (N_2) Chamber

Water vapour has a high abundance in air at ambient conditions. Water vapour has many strong THz resonances, as can be seen in figure 3.16. These resonances can hinder the extraction of accurate optical constants from measured data as they can obscure the properties of the material where they are present

in the spectrum. These resonances will always be present in ambient conditions. Due to the sensitivity of the system and fluctuations in the amount of water vapour present in the beam path, it is not simple or reliable to remove the water vapour from the data via post processing, thus it is preferable to remove the water vapour from the beam path, which is why it is preferable to perform measurements in a dry environment, as opposed to air. Dry N_2 gas is used to achieve this.

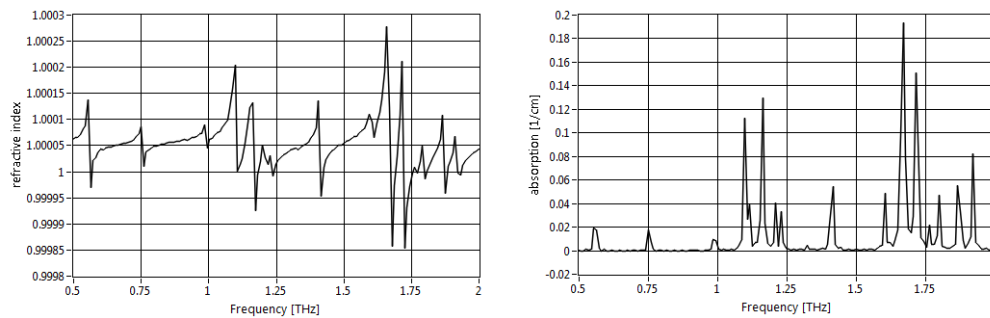


Figure 3.16: The real refractive index and absorption coefficient of water vapour for the THz spectrum, measured at atmospheric pressure and room temperature in our lab.

A chamber was constructed with a parallel gas flow system to effectively create a N_2 environment along the THz optical path and purge the system of moisture. A diagrammatic representation of this can be seen in figure 3.17.

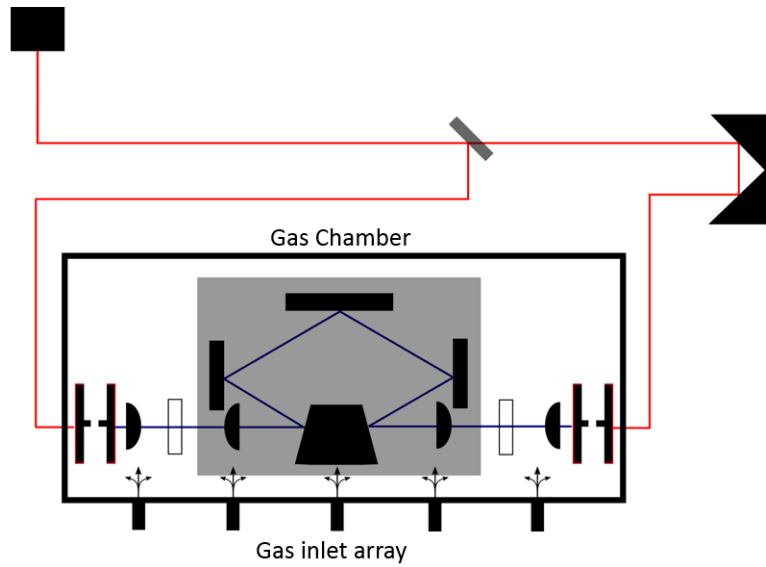


Figure 3.17: A diagram of the THz ellipsometric setup with the nitrogen gas chamber installed.

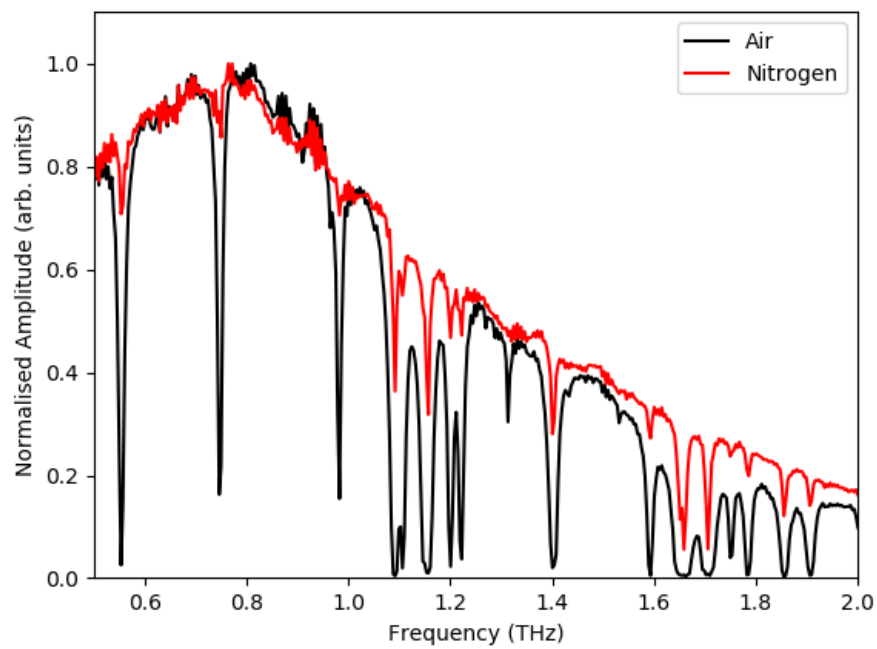


Figure 3.18: The THz spectrum measured for our system, using a silver mirror and s-polarized light in air and nitrogen.

From figure 3.18 it is evident that the implementation of the gas chamber and N₂ gas has greatly reduced the prominence of the water vapour spectra in our THz spectrum. The spectrum labeled as 'Air' had a humidity measured to be $\approx 51\%$ and spectrum labeled as 'Nitrogen' was measured to have a humidity of $\leq 0.1\%$. Due to the size of the system, it was found to be difficult to completely remove the water vapour present in the system, but the gas chamber greatly decreased the effect of water vapour on measurements.

Chapter 4

Simulation of THz ellipsometry measurements

Simulated data is produced to test the validity of the data extraction techniques discussed in chapter 5. The strategy is to generate an initial electric field in the time-domain and transform it to frequency domain via a fast Fourier transform (FFT). A transfer function representing the system of interest is then applied to this frequency domain electric field. The resultant electric field is transformed back to the time-domain via an inverse FFT (IFFT). This time-domain data therefore simulates the measured data. This data can then be fed into the data extraction algorithm to test its validity.

4.1 Incident Electric Field

As discussed in section 3.1.1, we make use of a photo-conductive antenna in our setup to generate THz radiation. The electric field generated by this antenna is described by equation 3.1.1 and 3.1.2.

The laser we use in our setup to trigger the antenna has a pulse duration, τ_p , of 90 fs. Low temperature grown GaAs (LT-GaAS), the substrate on which our antennae are printed, has an excitation lifetime, τ_c , of 300 fs and momentum relaxation time, τ_s , of 25 fs [17]. The size of the dipole, l_e , is $20 \mu\text{m}$ and the distance to the first collimation optic, r , is 45 mm. These values were used with equations 3.1.1 and 3.1.2 to generate the electric field depicted in figure 4.1. This field is used as our incident field during these simulations.

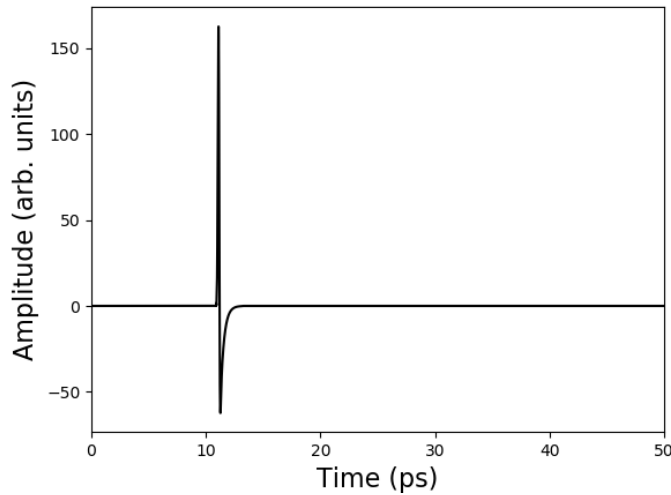


Figure 4.1: Time-domain electric field generated via equation 3.1.1 for a $20\ \mu\text{m}$ antenna on LT-GaAs.

4.2 General transfer function

As the simplest and most general example, a THz pulse incident on a single layer isotropic dielectric medium is initially considered. According to the Fresnel equations, as discussed in section 2.3, an electric field incident on the interface between two media with different refractive indexes is partially transmitted and reflected. There is an initial external reflection from the sample, followed by a train of internal reflections transmitted out of the sample (Etalon effect). Using Snell's laws, section 2.4, the angle of transmission into the sample can be determined, from this the distance light travels through the sample for each transmitted internal reflection can be calculated. This distance is used to calculate the attenuation due to absorption and phase delay of the electric field as it travels through the sample. Considering an electric field, E_0 incident on a material with real refractive index $n(f)$, extinction coefficient $\kappa(f)$ and thickness d_0 , at an angle of incidence θ_0 , the expected reflected s- and p-polarized electric fields are represented by:

$$E_s(t) = \tilde{r}_{s01}E_{s0}(t) + \tilde{t}_{s01}\tilde{r}_{s12}\tilde{t}_{s10}AE_{s0}(t) + \tilde{t}_{s01}\tilde{r}_{s12}^2\tilde{r}_{s10}\tilde{t}_{s10}A^2E_{s0}(t) + \dots \quad (4.2.1)$$

$$= \tilde{r}_{s01}E_{s0}(t) + \tilde{t}_{s01}\tilde{r}_{s12}\tilde{t}_{s10}A \sum_{j=0}^{\infty} (\tilde{r}_{s10}\tilde{r}_{s12}A)^j E_{s0}(t) \quad (4.2.2)$$

$$E_p(t) = \tilde{r}_{p01}E_{p0}(t) + \tilde{t}_{p01}\tilde{r}_{p12}\tilde{t}_{p10}AE_{p0}(t) + \tilde{t}_{p01}\tilde{r}_{p12}^2\tilde{r}_{p10}\tilde{t}_{p10}A^2E_{p0}(t) + \dots \quad (4.2.3)$$

$$= \tilde{r}_{p01}E_{p0}(t) + \tilde{t}_{p01}\tilde{r}_{p12}\tilde{t}_{p10}A \sum_{j=0}^{\infty} (\tilde{r}_{p10}\tilde{r}_{p12}A)^j E_{p0}(t) \quad (4.2.4)$$

$$A = \exp\left[\frac{-2\pi f\tilde{n}_1 d}{c}\right] \quad (4.2.5)$$

$$d = \frac{2d_0}{\cos\theta_{1prop}} \quad (4.2.6)$$

$$\tilde{n}_1 = n_1 - i\kappa_1 \quad (4.2.7)$$

where \tilde{t}_{s01} , \tilde{t}_{p01} , \tilde{r}_{s01} , \tilde{r}_{p01} are the Fresnel transmission and reflection coefficients for the interface between the initial medium and the sample. The transmission and reflection coefficients for the interface between the sample and the initial medium are represented by \tilde{t}_{s10} , \tilde{t}_{p10} , \tilde{r}_{s10} and \tilde{r}_{p10} , where as \tilde{t}_{s12} , \tilde{t}_{p12} , \tilde{r}_{s12} and \tilde{r}_{p12} represent the transmission and reflection coefficients for the interface between the sample and the medium following the sample. These coefficients are calculated using the Fresnel equations (section 2.3). The attenuation and phase delay coefficient (section 2.2) is represented by A . The distance that the electric field travels through the medium is represented by d . The complex refractive index of the sample is represented by \tilde{n}_1 . The angle of propagation, θ_{1prop} , is calculated by use of equation 2.4.6.

The complex refractive index is frequency dependent, as is the attenuation and phase delay function (equation 2.2.9), hence it is preferable to work in the frequency domain. Equation 4.2.2 and 4.2.4 are transformed from the time domain to the frequency domain with a Fourier transform.

$$E_s(f) = (\tilde{r}_{s01}(f) + \tilde{t}_{s01}\tilde{r}_{s12}\tilde{t}_{s10}A \sum_{j=0}^{\infty} (\tilde{r}_{s10}\tilde{r}_{s12}A)^j) E_{s0}(f) \quad (4.2.8)$$

$$E_p(f) = (\tilde{r}_{p01}(f) + \tilde{t}_{p01}\tilde{r}_{p12}\tilde{t}_{p10}A \sum_{j=0}^{\infty} (\tilde{r}_{p10}\tilde{r}_{p12}A)^j) E_{p0}(f) \quad (4.2.9)$$

4.3 Geometric Correction

From ray tracing it is found that in the case of internal reflections, each internal reflection takes a shorter route through the setup than expected. In turn, this

results in travel time distances between reflected pulses being shorter than expected and needs to be corrected for.

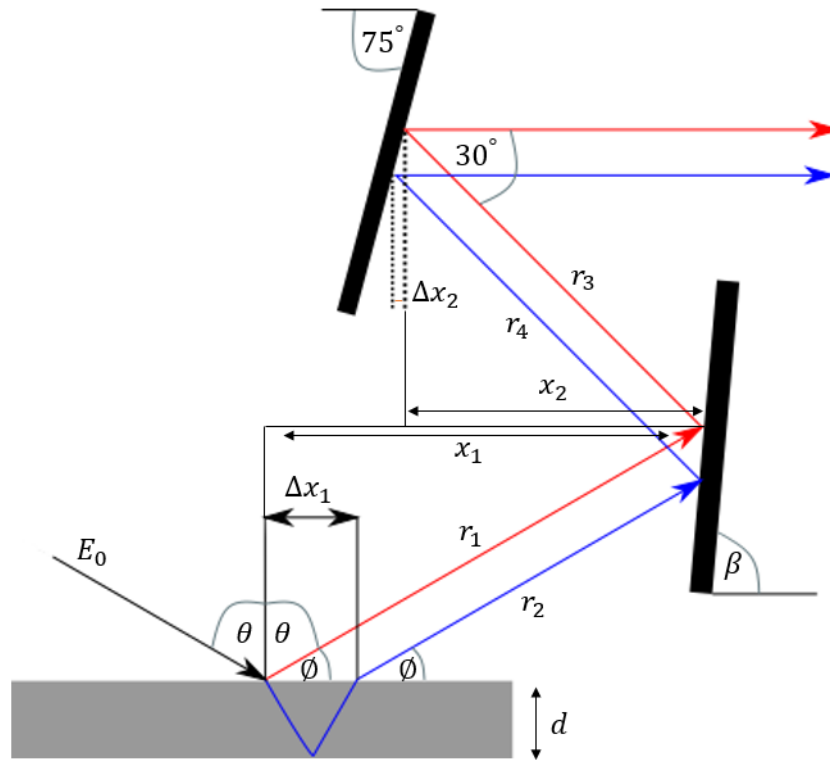


Figure 4.2: A ray tracing diagram for calculating the travel time difference between two successive reflections traveling through the setup.

This path length distance can be calculated by using the angle of incidence, θ , and the thickness of the sample, d . The angle at which light reflects from the second mirror, 30° , and the horizontal separation distance between surfaces, x_1 and x_2 , are known.

The difference between the two path lengths Δl can be calculated from the lengths r_1 , r_2 , r_3 , r_4 and Δx_2 .

$$\Delta r_1 = r_1 - r_2 \quad (4.3.1)$$

$$\Delta r_3 = r_3 - r_4 \quad (4.3.2)$$

$$\Delta l = \Delta r_1 + \Delta r_2 - \Delta x_2 \quad (4.3.3)$$

For an in-depth explanation on how to solve these value, please refer to Appendix C. This calculation will be used to derive a correction to the travel time of pulses traveling through the system.

For our system, if a $500\ \mu\text{m}$ thick undoped silicon sample of with an angle of incidence of 60° is considered, the calculated correction to the travel distance is $227\ \mu\text{m}$. This equates to the internal reflections being detected $0.757\ \text{ps}$ earlier than expected. This value is introduced as a phase correction when travel times through the sample are calculated. If this were to be ignored, the resultant travel times would be erroneous enough to introduce large errors when compared to measured data, especially as this error is cumulative for each successive internal reflection.

4.4 High resistivity silicon simulation example

The simulated data is compared to measured data to verify its validity. A $500\ \mu\text{m}$ thick sample with a frequency independent real refractive index of 3.4177 and a frequency independent absorption coefficient of $0.03\ \text{cm}^{-1}$ was simulated, as these values correspond to the measured optical properties of high resistivity float zone silicon [20–22]. This simulated data was compared to data measured by our setup for a $500\ \mu\text{m}$ thick high resistivity float zone single crystal silicon sample.

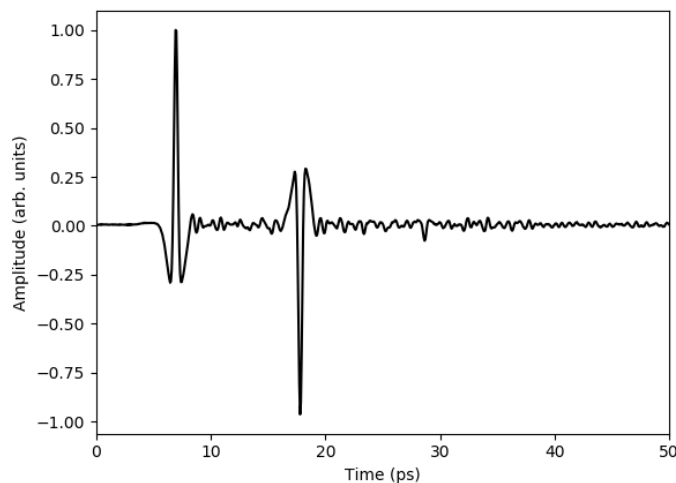


Figure 4.3: Normalized THz electric field measured in the time-domain by our setup for p-polarized light reflected from a $500\ \mu\text{m}$ thick high resistivity silicon sample.

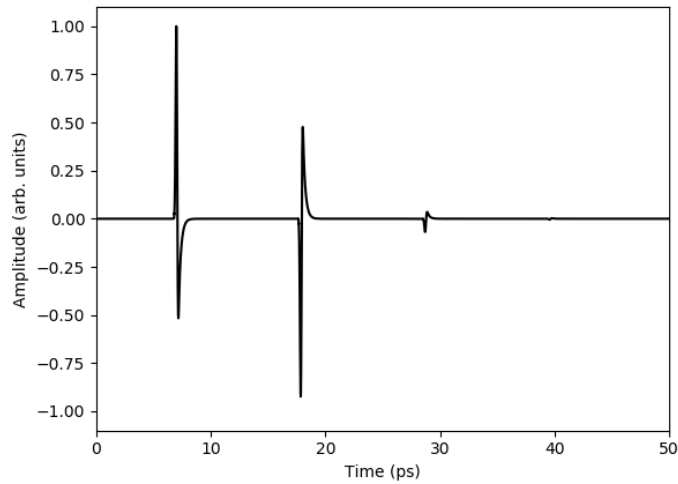


Figure 4.4: Normalized simulated THz electric field in the time-domain of p-polarized light reflected from a $500 \mu\text{m}$ thick high resistivity silicon sample.

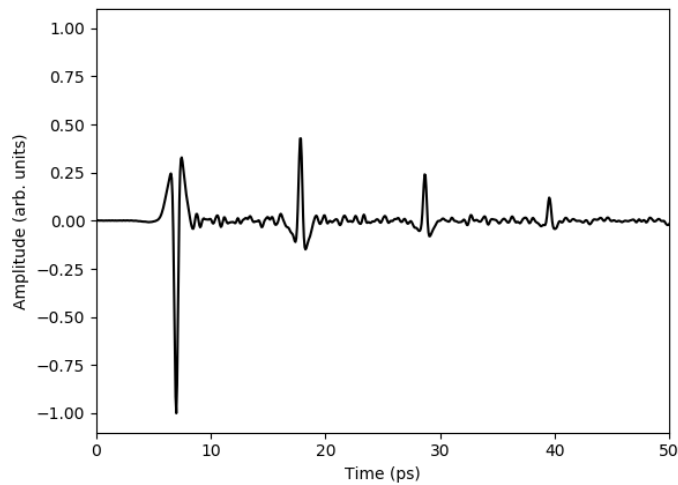


Figure 4.5: Normalized THz electric field measured in the time-domain by our setup for s-polarized light reflected from a $500 \mu\text{m}$ thick high resistivity silicon sample.

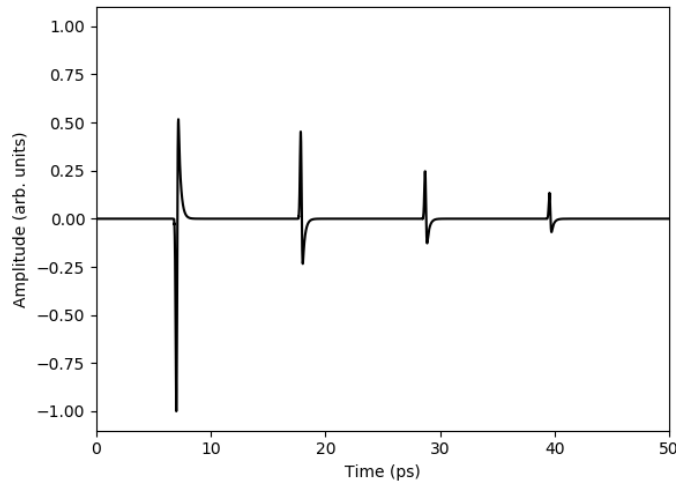


Figure 4.6: Normalized simulated THz electric field in the time-domain of s-polarized light reflected from a $500 \mu\text{m}$ thick high resistivity silicon sample.

From figures 4.3 - 4.6 it is found that the simulated data visually correlates well with experimental data. The time-delay between successive pulses correspond with one another and the phase shifts in pulses match expectations, which can be seen in pulses flipping when a π phase shift occurs. Lastly, the attenuation in successive pulses correspond visually.

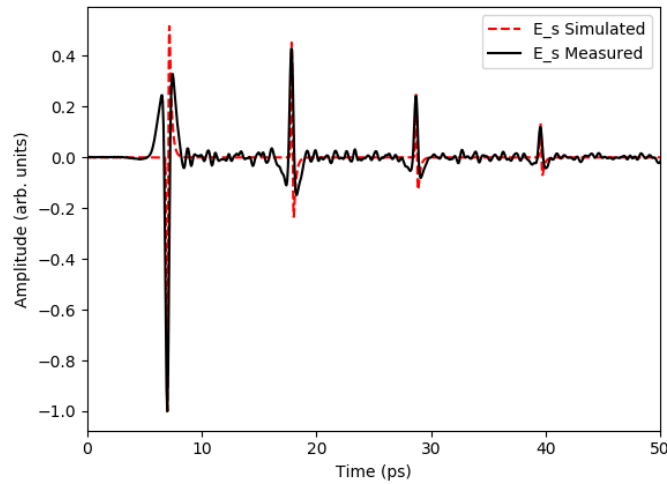


Figure 4.7: Comparison between simulated and measured normalized THz electric field in the time-domain for s-polarized light reflected from a $500 \mu\text{m}$ thick high resistivity silicon sample.

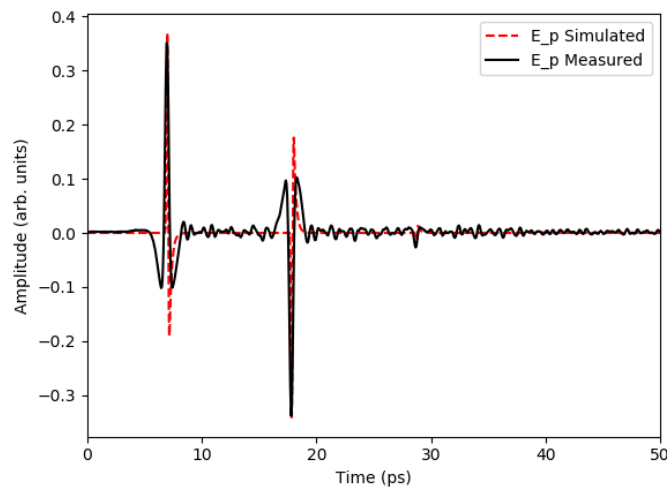


Figure 4.8: Comparison between simulated and measured THz electric field in the time-domain for p-polarized light reflected from a $500 \mu\text{m}$ thick high resistivity silicon sample. These electric fields have been normalized with respect to their corresponding s-polarized reflections.

By comparing the simulated data with measured data, we found that our angle of incidence is 60.3° . At this angle, both the Fresnel coefficients for s-

CHAPTER 4. SIMULATION OF THZ ELLIPSOMETRY MEASUREMENTS **36**

and p-polarized light and the travel time between subsequent pulses match very well, as can be seen in figure 4.7 and 4.8. Further analysis of this sample can be found in section 6.3.2.

Chapter 5

Data Analysis

Currently there is a distinct lack of data extraction techniques developed for THz time-domain ellipsometry, as many of the traditional methods of ellipsometric data analysis techniques need revision for implementation with this method of ellipsometry [1; 3; 33; 34]. Most of the classical techniques developed for ellipsometry focused on intensity based measurements and tricks for extracting the phase for such measurements [13], whereas work in terahertz ellipsometry focuses on bulk isotropic samples and are very sample specific solutions thus far [1; 3; 33; 34]. These techniques do not lend themselves well to isotropic samples which allow for measurable internal reflections, nor do they work when a sample consists of more than one layer.

We will discuss the data extraction technique applied to bulk isotropic samples. We have developed a technique which extracts the complex refractive index of isotropic samples with measurable internal reflections. A technique for extracting optical data from a two-layer isotropic system is also proposed and discussed.

5.1 Bulk isotropic model

Bulk isotropic materials are, in this context, defined as optically isotropic dielectric materials that do not cause depolarization dependent on the crystal orientation and that have a thickness and optical density which do not allow for measurable internal reflections. Accordingly, for this model only first surface reflections need to be considered. A diagram depicting this interaction can be seen in figure 5.1.

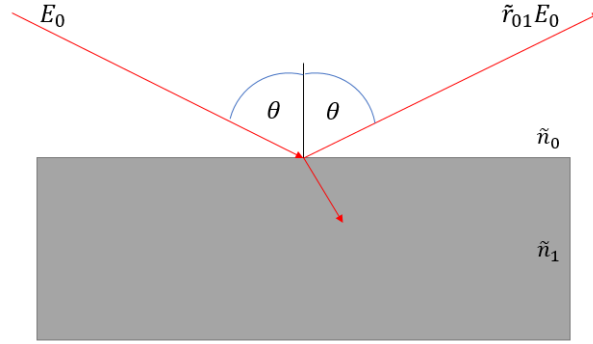


Figure 5.1: Diagram depicting light matter interaction with a bulk isotropic sample. Only surface reflections are measurable, as internal reflections are too weak to be measured.

Let us consider the electric field reflected from a bulk isotropic sample. If the s- and p- polarised incident electric fields are the same, i.e. $E_{0s} = E_{0p} = E_0$, the observed reflected electric field measured in time for the s- and p-polarization can be described as follows

$$E_s(t) = \tilde{r}_s(f)E_0(t) \quad (5.1.1)$$

$$E_p(t) = \tilde{r}_p(f)E_0(t) \quad (5.1.2)$$

where $\tilde{r}_s(f)$ and $\tilde{r}_p(f)$ are the frequency dependent s- and p-reflection coefficients (equation 2.3.6 and 2.3.7) and E_0 is the electric field, incident either with s- or p-polarization. An example of $E_0(t)$, $E_s(t)$ and E_p for a 2 mm thick sample, with a frequency independent real refractive index of 2.5 and a frequency independent absorption coefficient of 120 cm^{-1} , can be seen in figure 5.2.

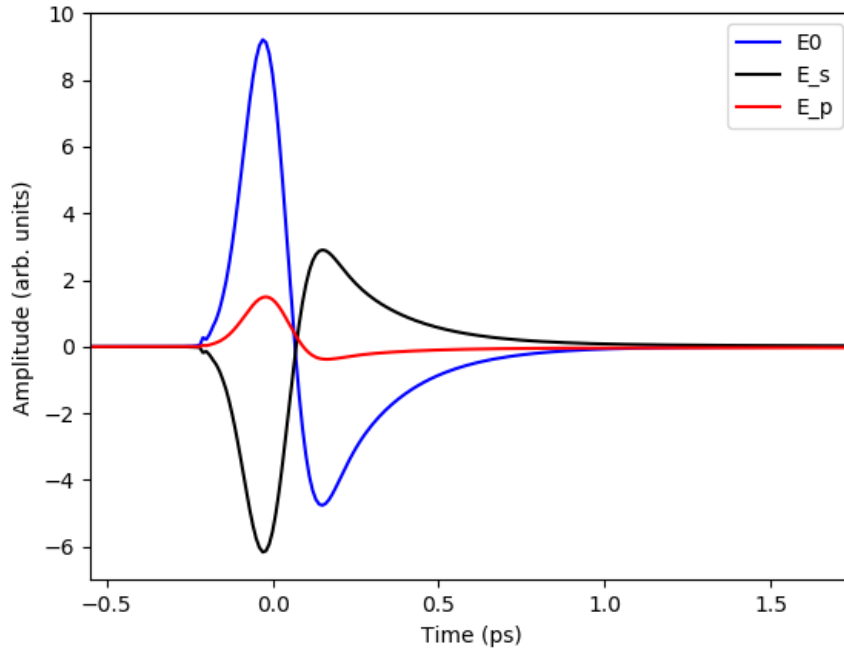


Figure 5.2: Simulated terahertz electric field E_0 in time, the s-polarised electric field reflected from the sample for E_0 with a pure s-polarization incident on the sample and the p-polarised electric field reflected from the sample for E_0 with a pure p-polarization incident on the sample. The sample is bulk isotropic in nature and has a real refractive index of 2.5 and absorption coefficient of 120 cm^{-1} . The extinction coefficient is frequency dependent and calculated by use of equation 2.2.8.

Even though the refractive index of our model sample is frequency independent, the reflection coefficients, $\tilde{r}_s(f)$ and $\tilde{r}_p(f)$, are frequency dependent, and hence it is convenient to work in the frequency domain. By performing a fast Fourier transform (FFT) on the data it is converted from the time to the frequency domain, hence the electric field components are rewritten as

$$E_s(f) = \tilde{r}_s(f)E_0(f) \quad (5.1.3)$$

$$E_p(f) = \tilde{r}_p(f)E_0(f) \quad (5.1.4)$$

Using standard ellipsometric data analysis, it is possible to extract the complex refractive index from this data [13].

$$P(f) = \frac{E_p(f)}{E_s(f)} \quad (5.1.5)$$

$$\tilde{\epsilon}(f) = \tilde{n}_0 \sin^2 \theta \left[1 + \left(\frac{1 - P(f)}{1 + P(f)} \right)^2 \tan^2 \theta \right] \quad (5.1.6)$$

$$\tilde{n}(f) = \sqrt{\tilde{\epsilon}(f)} \quad (5.1.7)$$

The angle of incidence is given by θ in equation 5.1.6, \tilde{n}_0 is the complex refractive index of the material surrounding the sample, $P(f)$ is the ratio between the p- and s-polarized electric fields, $\tilde{\epsilon}(f)$ is the frequency dependent complex dielectric constant of the sample and $\tilde{n}(f)$ is the frequency dependent complex refractive index of the material.

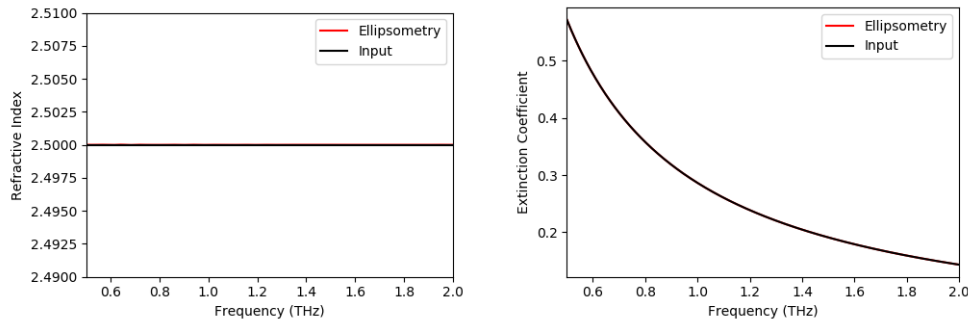


Figure 5.3: The complex refractive index extracted from the data presented in figure 5.2 via the bulk isotropic data extraction technique. The real part (reflective index) and imaginary part (extinction coefficient) are plotted as function of the THz frequency.

This technique is computationally light, as calculations scale linearly with the size of the transformed data set. As can be seen from figure 5.3, this technique is capable of accurately extracting the complex refractive index for the trivial case of bulk isotropic samples where only first surface reflections need to be considered.

5.2 Single layer isotropic model

Single layer isotropic samples are, in the context of this work, defined as optically isotropic dielectric materials. These are samples with a thickness and optical density that allow for measurable internal reflections. This model expands on the model in section 5.1 by incorporating these internal reflections.

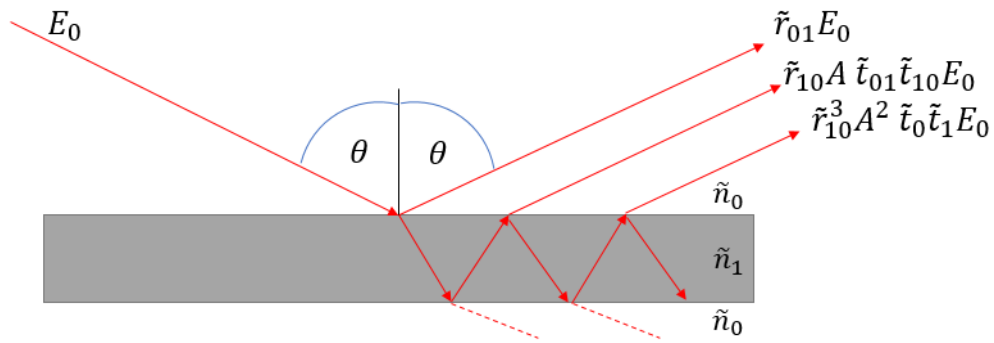


Figure 5.4: Diagram depicting light matter interaction with a single layer isotropic sample. Both surface reflections and internal reflections are measurable.

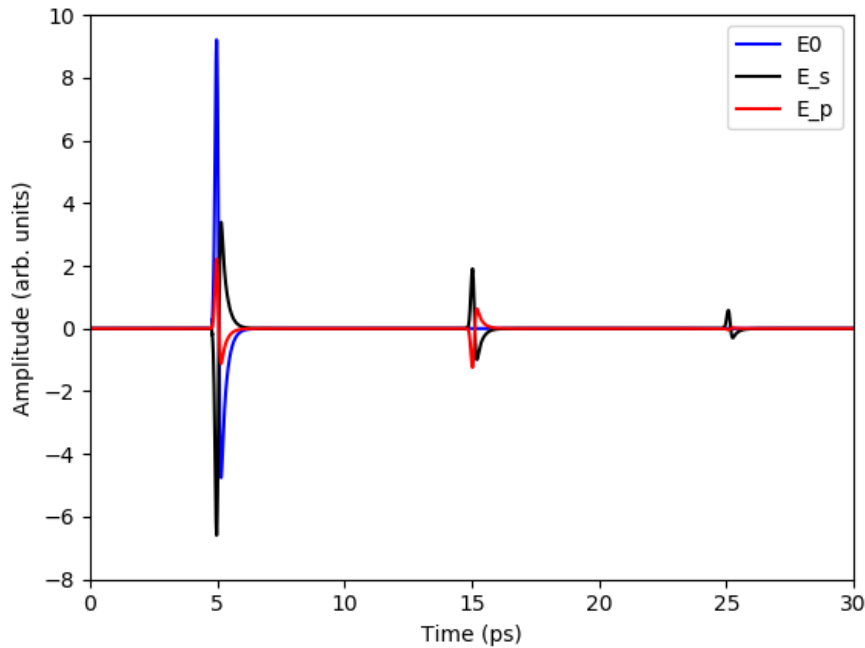


Figure 5.5: Simulate THz electric field E_0 , simulated s-polarized reflection from a single layer sample when E_0 is considered purely s-polarized and simulated p-polarized reflection from a single layer sample when E_0 is considered purely p-polarized. This simulation is in the time domain and the sample in question is a $500\ \mu\text{m}$ single layer isotropic sample with a frequency independent real refractive index of 3.136 and a frequency independent absorption coefficient of $10\ \text{cm}^{-1}$. The extinction coefficient is frequency dependent and calculated by use of equation 2.2.8.

5.2.1 Transfer Function

We define the influence of the material on the light pulse as it interacts as a transfer function that can be applied to the light pulse to account for this interaction.

In time-domain data measured for a single layer isotropic system, as depicted in figure 5.5, an initial surface reflection followed by a series of pulses as a result of internal reflections is observed. Each of the reflected pulses are separated by fixed temporal spacing, which is only determined by the thickness of the sample, the angle of incidence and the refractive index of the sample.

In this model light reflects off both the back and front face of the sample. The interaction of an electric field, E_0 , with such a system in the time domain is described by the following function:

$$\begin{aligned}
E(t) &= \tilde{r}_{01}E_0(t) + \tilde{t}_{01}\tilde{t}_{10}\tilde{r}_{10}AE_0(t) + \tilde{t}_{01}\tilde{t}_{10}\tilde{r}_{10}^3A^2E_0(t) \\
&\quad + \tilde{t}_{01}\tilde{t}_{10}\tilde{r}_{10}^5A^3E_0(t) + \dots \\
&= \tilde{r}_{01}E_0(t) + \tilde{t}_{01}\tilde{t}_{10}\tilde{r}_{10}A \sum_{m=0}^{\infty} (\tilde{r}_{10}^2A)^m E_0(t)
\end{aligned} \tag{5.2.1}$$

where:

$$A = e^{-i2\pi f \frac{\tilde{n}d}{c}} \tag{5.2.2}$$

$$d = \frac{2d_0}{\cos \theta_{1prop}} \tag{5.2.3}$$

$$\tilde{n} = n - i\kappa \tag{5.2.4}$$

and \tilde{r}_{01} and \tilde{t}_{01} are the reflection and transmission coefficients for light incident on the system from outside as determined from the Fresnel equations, while \tilde{r}_{10} and \tilde{t}_{10} are the reflection and transmission coefficients for light exiting the system. In this equation d_0 is the sample thickness and n is the real refractive index of the material at a given frequency. The frequency of the electric field is denoted by f and κ is the extinction coefficient of the material at the given frequency. The angle of propagation, θ_{1prop} , is calculated by use of equation 2.4.6.

Using a Fourier transform, this equation is rewritten in the frequency domain as follows

$$E(f) = E_0(f)(\tilde{r}_{01} + \tilde{t}_{01}\tilde{t}_{10}\tilde{r}_{10}A(f) \sum_{m=0}^{\infty} (\tilde{r}_{10}^2A(f))^m) \tag{5.2.5}$$

5.2.2 Complex refractive index extraction

The transfer function described in equation 5.2.5 will be used in this subsection to obtain a method to extract the complex refractive index, \tilde{n} , of a sample of interest.

The s- and p-polarized electric fields, $E_s(t)$ and $E_p(t)$, reflected from a sample have been measured and transformed via FFT to $E_s(f)$ and $E_p(f)$. These electric fields can be described by extending equation 5.2.5. For these equations it is assumed that $E_{0s} = E_{0p} = E_0$.

$$\begin{aligned}
E_s(f) &= E_0(f)(\tilde{r}_{s01} + \tilde{t}_{s01}\tilde{t}_{s10}\tilde{r}_{s10}A(f) \sum_{m=0}^{\infty} (\tilde{r}_{s10}^2 A(f))^m) \\
&= E_0(f) \left(\tilde{r}_{s01} + \frac{\tilde{t}_{s01}\tilde{t}_{s10}\tilde{r}_{s10}A(f)}{1 - \tilde{r}_{s10}^2 A(f)} \right) \quad (5.2.6)
\end{aligned}$$

$$\begin{aligned}
E_p(f) &= E_0(f)(\tilde{r}_{p01} + \tilde{t}_{p01}\tilde{t}_{p10}\tilde{r}_{p10}A(f) \sum_{m=0}^{\infty} (\tilde{r}_{p10}^2 A(f))^m) \\
&= E_0(f) \left(\tilde{r}_{p01} + \frac{\tilde{t}_{p01}\tilde{t}_{p10}\tilde{r}_{p10}A(f)}{1 - \tilde{r}_{p10}^2 A(f)} \right) \quad (5.2.7)
\end{aligned}$$

The reflected electric fields are strongly dependent on the incident field. However, the need for the electric field E_0 to be known is eliminated by taking the ratio between $E_p(f)$ and $E_s(f)$, thus eliminating the need for a reference measurement. This simplifies routine measurements as any misalignment that might be introduced by replacing a reference sample with the actual sample is eliminated.

$$H(f) = \frac{\tilde{r}_{p01} + \frac{\tilde{t}_{p01}\tilde{t}_{p10}\tilde{r}_{p10}A(f)}{1 - \tilde{r}_{p10}^2 A(f)}}{\tilde{r}_{s01} + \frac{\tilde{t}_{s01}\tilde{t}_{s10}\tilde{r}_{s10}A(f)}{1 - \tilde{r}_{s10}^2 A(f)}} \quad (5.2.8)$$

Equation 5.2.8 is fitted to the measured data, using the real and imaginary parts of the complex index of refraction, \tilde{n} , as the fit parameters. The Nelder-Mead algorithm is implemented to perform this fit via error minimization. This minimization algorithm was chosen due to the similarity between our method and a method previously developed by Pupeza *et al* for THz time-domain transmission spectroscopy [35].

The Nelder-Mead algorithm is a direct search algorithm which is used to minimize real non-linear functions, by using only function values, without any derivative information [36]. The Nelder-Mead algorithm is especially useful for solving optimization problems for which the differential is either unknown or not computable. The Nelder-Mead algorithm is also noted for being robust against signal noise [37].

The Nelder-Mead algorithm forms a geometric object of $N + 1$ equidistant function points, which is generally referred to as a simplex [38], where N is the number of variables which need to be optimized. In our case, the complex refractive index of each frequency component will be minimized separately, as opposed to minimizing the values for the entire data set at once, as this will help reduce the errors in the minimized data [37]. In this case, only two variables (the real and imaginary part of the complex index of refraction) will be considered, thus the simplex will be a triangle. For every vertex which makes up this simplex, a fitness function is calculated. The vertex with the

worst fitness function value is updated in accordance to the set of rules, *Order*, *Reflect*, *Expand* and *Contract*, which can be found in [36]. The optimization stops once the fitness function or standard deviation of the fitness function at all vertices reaches a threshold set at the beginning of the optimization ($< 10^{-8}$). There is also a limit set to the number of iterations the optimization will undergo before it will be terminated (1000). More details on the Nelder-Mead optimization method can be found in [36; 37].

The Nelder-Mead algorithm minimizes the error between the theoretical transfer function ratio, $H(f)$, and the ratio between the measured electric fields, $\frac{E_p(f)}{E_s(f)}$, by optimizing the the real refractive index, n , and extinction coefficient, κ . In this way the complex refractive index is extracted from the measured data. In our data extraction software the Nelder-Mead algorithm was implemented via the *minimize* function of the Python library, Scipy, with the method set to *nelder-mead* [39].

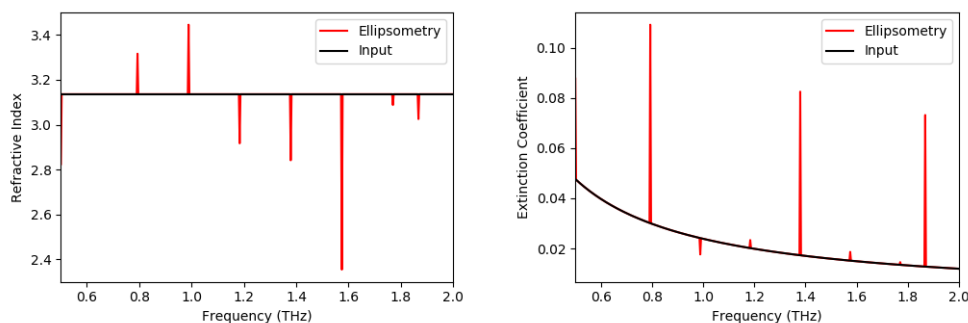


Figure 5.6: The complex refractive index extracted from the data presented in figure 5.5 via the complex refractive index extraction method. The sharp spikes present are numerical artifacts caused by erroneous convergence in the minimization algorithm. The initial values used in the simulation, and thus the expected values are represented by "Input", where as the extracted values are represented by "Ellipsometry".

5.2.3 Smoothing algorithm: LULU

The complex refractive index we extract by means of the method discussed in section 5.2.2 has single data point spikes present, as can be seen in figure 5.6. We know that the optical constants simulated are smooth, thus these spikes are erroneous. These spikes are numerical artifacts caused by erroneous convergence during the minimization process. These errors are easy to identify, as they are only a single data point in size each, and not to be confuse with actual phenomena occurring in the data.

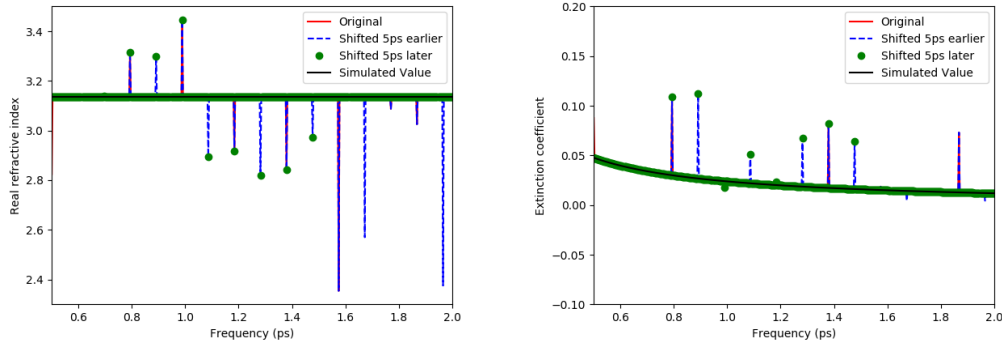


Figure 5.7: Complex refractive index extracted from data simulated for a $500\ \mu\text{m}$ sample with a frequency independent refractive index of 3.136 and frequency independent absorption coefficient of $10.0\ \text{cm}^{-1}$. The time data was sampled from -11 to $154\ \text{ps}$ (original), -6 to $159\ \text{ps}$ (Shifted 5ps later) and -16 to $149\ \text{ps}$ (Shifted 5ps earlier) and then the data extraction technique was applied.

If the sampling is slightly changed, some of these spikes will disappear and new spikes will appear, as can be seen in figure 5.7. This shows that these errors are not a simple constant problem and a broad based approach for filtering them out will be required. We suggest the use of a smoothing algorithm to do this.

A smoothing algorithm known as LULU is implemented to eliminate these erroneous points. LULU is an acronym for lower upper lower upper, which refers to how it operates. LULU is a min-max smoothing algorithm which consists of two operators, L and U . LULU smooths data by taking the maximum value amongst local minima for L or by taking the minimum value amongst local maxima for U for each data point in a data set. The number of data points which will be considered to either side of a given data point is known as the order of the LULU algorithm.

For a sequence $S = \{x_i | i \in N\}$ the n 'th order operators are defined as [40]:

$$L_n x_i = \max\{\min\{x_{i-n}, \dots, x_i\}, \dots, \min\{x_i, \dots, x_{i+n}\}\} \quad (5.2.9)$$

$$U_n x_i = \min\{\max\{x_{i-n}, \dots, x_i\}, \dots, \max\{x_i, \dots, x_{i+n}\}\} \quad (5.2.10)$$

By combining these operators as either LU or UL , very reliable smoothing of data can be achieved [41]. A one-dimensional variant of a selection method for selecting between LU and UL , as proposed by O. Kao [41] is implemented to smooth our extracted complex refractive index:

1. Apply LU and UL on x_i , resulting in w_1 and w_2 .

2. If $w_1 = w_2$, then $x_i = w_1 = w_2$. Proceed to step 4.
3. Otherwise $w_1 \neq w_2$ and if $|w_1 - x_i| < |w_2 - x_i|$, then $x_i = w_1$. Otherwise $x_i = w_2$.
4. Move to the next data point.

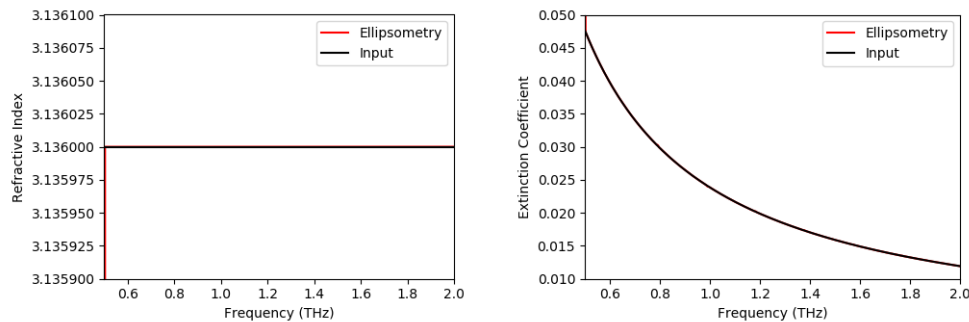


Figure 5.8: The complex refractive index in figure 5.6 after LULU of order 1 is applied to it.

In figure 5.6 the complex refractive index extracted by the algorithm for a single isotropic layer, as explained in section 5.2.2, from the data presented in figure 5.5 can be seen. Very clear numerical artifacts (spikes) are present in this data. A LULU of order 1 is applied to the data, resulting in the removal of these spikes, while leaving the data intact, as can be seen in figure 5.8.

LULU is applied to all single layer isotropic cases that follow.

5.2.4 Error tolerance

If errors are present in the thickness of the sample or the angle of incidence used as input in the data extraction method, this can have a detrimental effect on the extracted results. It is important to understand to what extent these errors can be tolerated.

Several sets of simulated data were produced to test the effect of the accuracy of the determined sample thickness on the extracted result. In the one set the real refractive index was varied, while the absorption coefficient was kept constant and several different sized errors were introduced to the sample thickness used during data extraction. In the other set the absorption coefficient was varied, while the real refractive index was kept constant and several different sized errors were introduced to the sample thickness used during data extraction. The error in the extracted complex refractive index was calculated for each of these data sets (figures 5.9 and 5.10).

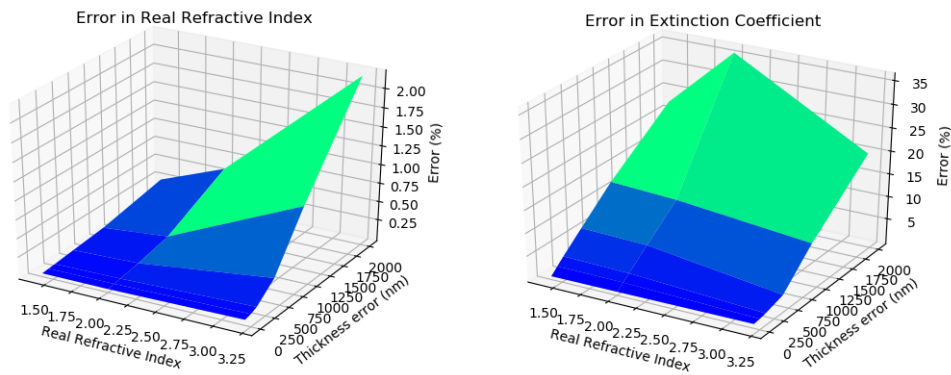


Figure 5.9: Average error in the real and imaginary parts of the extracted complex refractive index, when a thickness error is introduced (0-2000 nm), if the absorption coefficient is kept constant (5.0 cm^{-1}) and the real refractive index is varied (1.4-3.2). The thickness of the samples is $500 \mu\text{m}$. The average value was calculated for the frequency domain 0.5 – 2.0 THz.

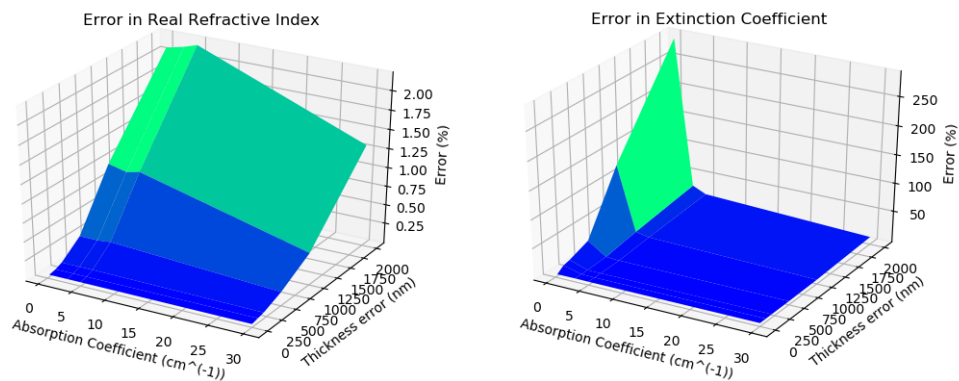


Figure 5.10: Average error in extracted complex refractive index, when a thickness error is introduced (0-2000 nm), if the real refractive index is kept constant (3.2) and the absorption coefficient is varied ($0.3\text{-}30.0 \text{ cm}^{-1}$). The thickness of the samples is $500 \mu\text{m}$. The average value was calculated for the frequency domain 0.5 – 2.0 THz.

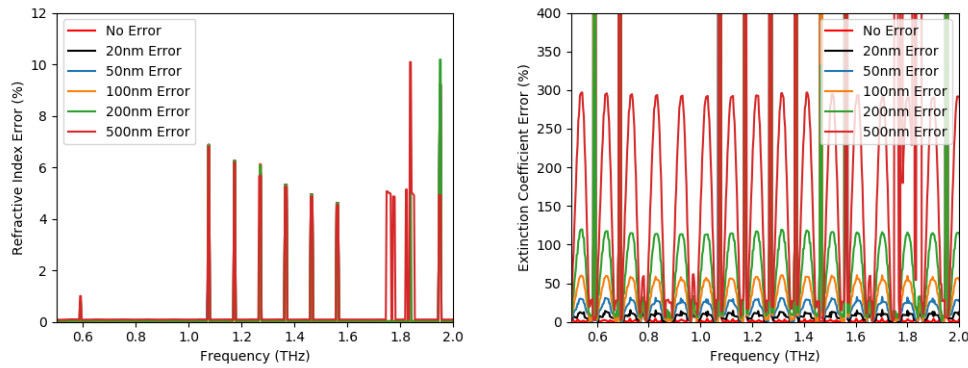


Figure 5.11: Error in extracted complex refractive index, when a thickness error is introduced (0- 500 nm), for a highly transparent sample. The thickness of the samples is $500\mu\text{m}$, the real refractive index is 3.2 and the absorption coefficient is 0.03 cm^{-1} .

We find that the extraction of the real refractive index is quite robust with regard to the accuracy in determining the sample thickness, exhibiting average errors lower than 2.5% for all cases, as evidenced in figures 5.9 and 5.10. The error in the extracted extinction coefficient is a stronger limiting factor, as can be seen in figures 5.9 and 5.10. An accuracy greater than 99.96% is required for the thickness of absorbing (absorption coefficient $> 1.0\text{ cm}^{-1}$) materials to maintain an error average below 10% in the extracted extinction coefficient.

For transparent materials the thickness accuracy becomes more strenuous, e.g. for a material with an absorption coefficient of 0.03 cm^{-1} it was found that a thickness accuracy of 99.996% was required to avoid the average error in the extracted extinction coefficient exceeding 10%. This value is obtained by taking the average of each graph in figure 5.11.

The accuracy with which the incident angle is known and its effect on the extracted complex refractive index was also tested. The same data sets used to test the thickness error tolerance were used to test the the incident angle error. Several different errors were introduced in the angle of incidence. The error in the extracted complex refractive index was calculated for each of these data sets (figures 5.12 and 5.13).

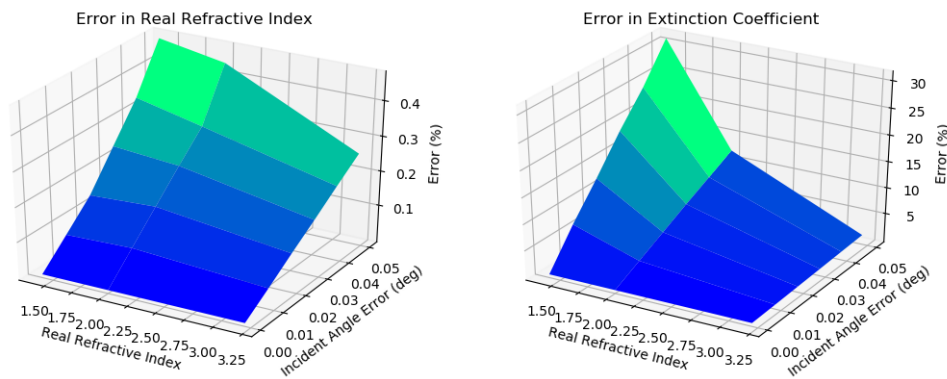


Figure 5.12: Average error in extracted complex refractive index, when an angle of incidence error is introduced ($0^\circ - 0.05^\circ$), if the absorption coefficient is kept constant (5.0 cm^{-1}) and the real refractive index is varied (1.4-3.2). The thickness of the samples is $500 \mu\text{m}$. The average value was calculated for the frequency domain $0.5 - 2.0 \text{ THz}$.

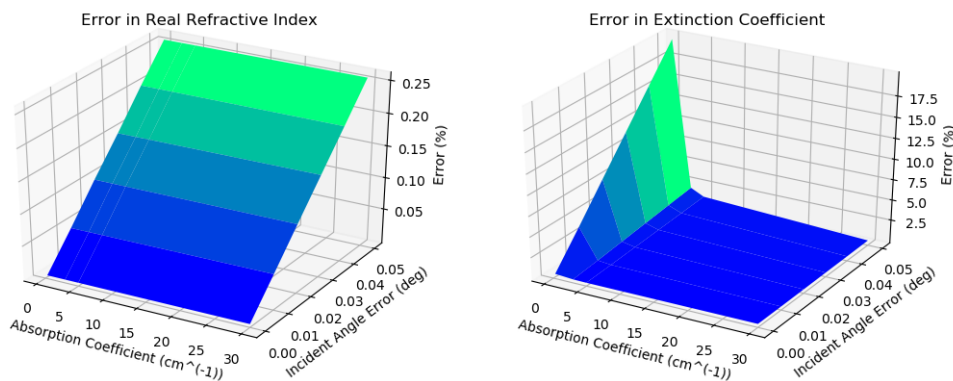


Figure 5.13: Average error in extracted complex refractive index, when an angle of incidence error is introduced ($0^\circ - 0.05^\circ$), if the real refractive index is kept constant (3.2) and the absorption coefficient is varied ($0.3 - 30.0 \text{ cm}^{-1}$). The thickness of the samples is $500 \mu\text{m}$. The average value was calculated for the frequency domain $0.5 - 2.0 \text{ THz}$.

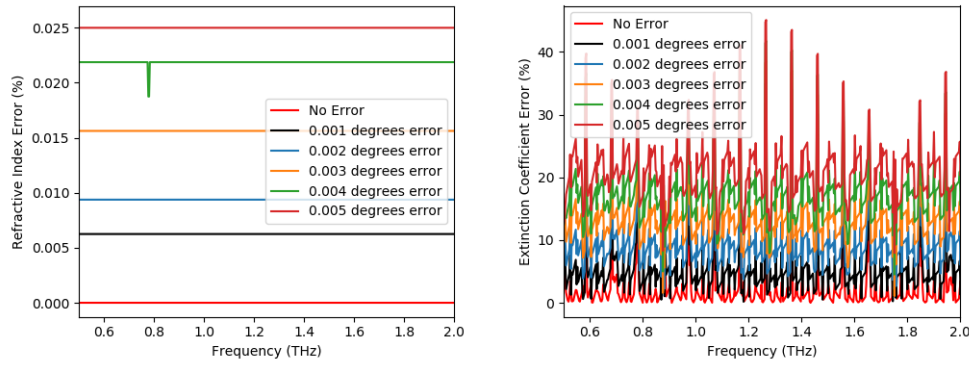


Figure 5.14: Error in extracted complex refractive index, when an angle of incidence error is introduced ($0^\circ - 0.005^\circ$), for a highly transparent sample. The thickness of the samples is $500\mu\text{m}$, the real refractive index is 3.2 and the absorption coefficient is 0.03cm^{-1} .

We find that the extracted real refractive index is resilient to errors in the angle of incidence. For an error of up to 0.05° in the angle of incidence the average error in the extracted real refractive remains below 0.5%. For the extinction coefficient extracted from absorbing (absorption coefficient $> 1.0\text{cm}^{-1}$) materials to have an accuracy greater than 90%, the error in the incident angle needs to be smaller than 0.02° , as can be seen from figures 5.12 and 5.13. When considering more transparent samples, this limitation becomes more strenuous, as can be seen in figure 5.14. As an example, consider a $500\mu\text{m}$ sample with a real refractive index of 3.2 and absorption coefficient of 0.03cm^{-1} . For this sample, the angle of incidence needs to be accurate to 0.002° for the extracted extinction coefficient to have an accuracy greater than 90%.

5.2.5 Thickness extraction

It was assumed that the thickness of the sample was perfectly known when extracting the complex refractive index presented in figure 5.8. However, for real world samples this thickness can only be measured up to a certain experimental degree of accuracy (the accuracy of a screw micrometer for instance). From simulations, discussed in section 5.2.4, we found that an accuracy greater than 99.96% is required for the thickness of absorbing (absorption coefficient $> 1.0\text{cm}^{-1}$) materials, otherwise errors are present in the data. For transparent materials the thickness accuracy becomes more strenuous, e.g. for a material with an absorption coefficient of 0.03cm^{-1} it was found that a thickness accuracy of 99.996% was required to avoid the average error in the data exceeding 10%.

If the thickness of the sample is not correct, this does not only result in erroneous values being extracted by the algorithm in section 5.2.2, but also results in oscillations being present on the extracted values, as can be seen in figure 5.15.

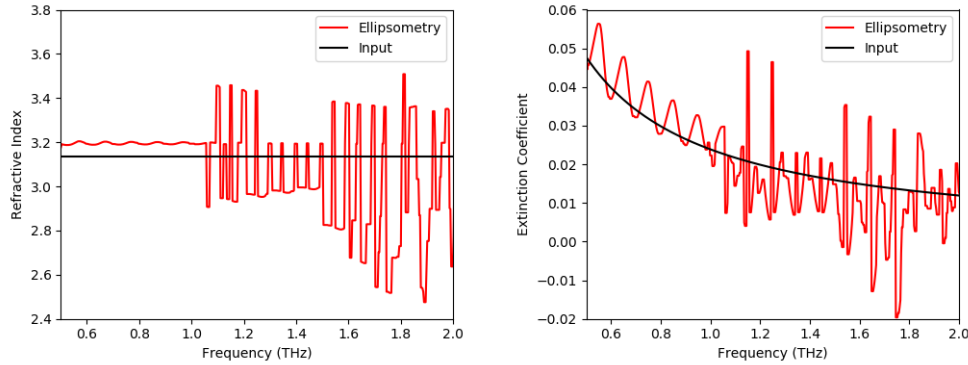


Figure 5.15: The complex refractive index extracted from the data presented in figure 5.5 via the complex refractive index extraction method presented in section 5.2.2 if the thickness was over estimated by $10 \mu\text{m}$.

These oscillations are used as an error value and a minimization algorithm is applied to calculate the correct thickness of the sample. The process works as follows for a set of z data points:

1. Start with initial thickness guess.
2. Calculate the complex refractive index.
3. Calculate the error:

$$error = \sum_{m=1}^{m < z} (|n_m - n_{m-1}| + |\kappa_m - \kappa_{m-1}|) \quad (5.2.11)$$

where n_m and κ_m are the real refractive index and extinction coefficient extracted for data point m .

4. Minimize *error* by altering the thickness used to calculate the complex refractive index.

The *minimize scalar* function of the Python library, Scipy, was used, with the method set to *bounded*, to minimize *error*. It uses the Brent algorithm to find a local minimum within a given bounded region. Brent's algorithm is a root-finding algorithm which combines the bisection method and secant

method with quadratic interpolation, which makes it a robust and highly efficient method [42]. The bounds of the minimization algorithm were set to $\pm 10 \mu\text{m}$ from the initial guess, as this is the expected limit to which we can measure the thickness of physical samples in our lab.

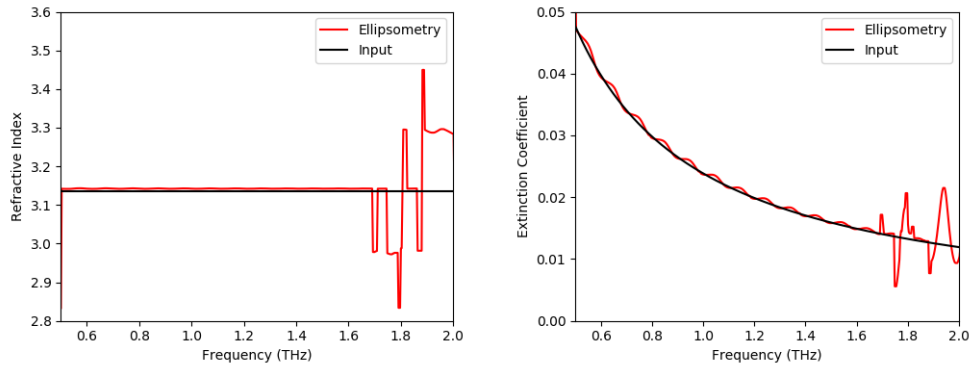


Figure 5.16: The complex refractive index extracted from the data presented in figure 5.5 via the complex refractive index extraction method presented in section 5.2.2 with an $10 \mu\text{m}$ error in the initial thickness guess, after applying the corrected thickness calculated via minimization of equation 5.2.11. The error still present in the thickness is $1.1 \mu\text{m}$.

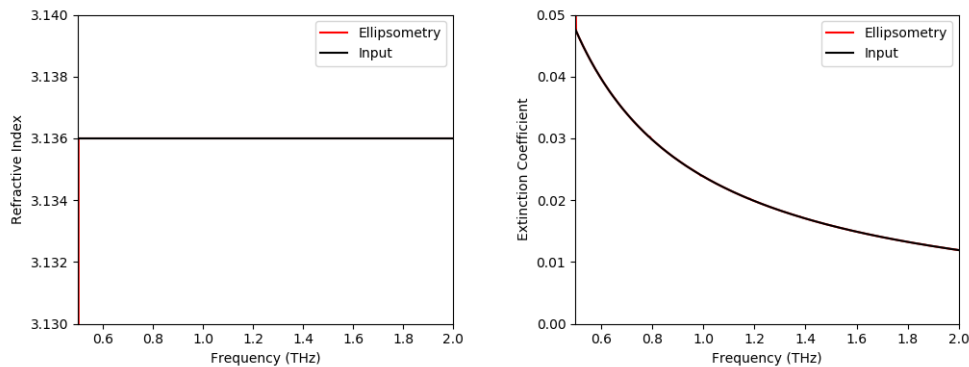


Figure 5.17: The complex refractive index extracted from the data presented in figure 5.5 via the complex refractive index extraction method presented in section 5.2.2 with an $1.1 \mu\text{m}$ error in the initial thickness guess, after applying the corrected thickness calculated via minimization of equation 5.2.11. No error remains in the thickness applied.

This process can be computationally strenuous and might require more than one pass, as can be seen from figure 5.16 and figure 5.17, but does yield the desired results, as evidenced by figure 5.17. We started with a $10\mu\text{m}$ (2%) error in sample thickness. The first application of the thickness extraction method produced thickness value with an error of $1.1\mu\text{m}$ (0.22%). When the thickness value produced by the first application of the thickness extraction method was used as the initial guess for the thickness extraction and the technique was reapplied to the data, the original thickness of the material was recovered (0% error).

5.2.6 Complete data extraction method

Combining the procedures from 5.2.5 and 5.2.2 it is possible to create a data extraction method that extracts both the complex refractive index and sample thickness, and accordingly does not require perfect knowledge of either.

However, having a good estimate of both the thickness and the complex refractive index simplifies and speeds up the data extraction.

The thickness of most samples can be measured with sufficient accuracy using a vernier caliper. For the complex refractive index it is more complicated, since if an unknown sample or a mixture of samples is investigated, this can not be estimated. A good initial guess can be obtained by only considering the surface reflection. This can be done by applying a windowing function to the measured data to truncate the data to the surface reflection. For the data produced by our system, the Hann window delivers favorable results [43]. The Hann window is described by the following function [44]:

$$G(x) = \begin{cases} \frac{1}{2} (1 + \cos(\frac{2\pi x}{L})) & \text{if } |x| \leq \frac{L}{2} \\ 0 & \text{if } |x| > \frac{L}{2} \end{cases}$$

where L is the desired duration of the window.

If a block window is used, as opposed to a smooth windowing function, this can introduce artificial discontinuities into the sampled data. When a FFT is performed on this truncated data, these discontinuities can lead to oscillations which will obscure the data. These oscillations are caused by the Gibbs phenomenon [45]. These discontinuities can also lead to an error known as spectral leakage, where it appears as if energy at one frequency leaks into other frequencies [43].

The Hann window is an especially useful window when working with FFTs, as it is smooth and its amplitude makes contact with 0 at its edges [43]. By applying a smooth window, such as the Hann window, spectral leakage caused by the windowing of the data is minimized [43] and the Gibbs phenomenon should not effect the data [44].

As an example to showcase the windowing of the electric field and its implementation as an initial guess, let us consider a $500\mu\text{m}$ sample with a

frequency independent refractive index of 3.2 and a absorption coefficient of 30 cm^{-1} . Three resonances are introduced to this data; one at 0.6 THz, one at 1.3 THz and the last at 1.65 THz. The resultant electric field can be seen in figure 5.18.

According to the Lorentz model, if electrons bound to molecules are viewed as damped, driven harmonic oscillators, at specific frequencies, they will have resonances. These resonances correspond to transition states in the molecule. The contribution of the resonance to the real refractive index and absorption coefficient at and around a resonance can be calculated by the following expression[11]:

$$n_r = \frac{Nq^2}{2m\epsilon_0} \frac{z(\omega_0^2 - \omega^2)}{(\omega_0^2 - \omega^2)^2 - \gamma^2\omega^2} \quad (5.2.12)$$

$$\alpha_r = \frac{Nq^2\omega^2}{m\epsilon_0 c} \frac{z\gamma}{(\omega_0^2 - \omega^2)^2 - \gamma^2\omega^2} \quad (5.2.13)$$

where ω_0 is the resonant frequency, ω is the frequency being considered, γ is the damping force applied to the electron, z is the driving force applied to the electron, N is the number of molecules considered, q is the charge of the electron and ϵ_0 is the electric permittivity of vacuum [11].

In the case where the damping is taken to be zero, equation 5.2.12 is discontinuous at the resonance frequency and when small damping values are used the change in the refractive index can be very sharp, as such it does not work well with FFTs [45]. For the purposes of the simulation, to simplify the proses of generating resonance-like behaviour, the following method was used to emulate a resonance:

$$\omega_{0 \text{ norm}} = \frac{\omega_0}{\Delta\omega} \quad (5.2.14)$$

$$\omega_{\text{ norm}} = \frac{\omega}{\Delta\omega} \quad (5.2.15)$$

$$Z = \frac{\omega_{\text{ norm}} - \omega_{0 \text{ norm}} - \frac{L}{2}}{v} \quad (5.2.16)$$

$$n_r = V_1 \frac{Z}{2} e^{\frac{-Z^2}{v}} \quad (5.2.17)$$

$$\alpha_r = V_2 \frac{12}{\pi} \frac{2}{Z^2 + \sqrt{v}} \quad (5.2.18)$$

where $\Delta\omega$ is the frequency spacing between data points considered for the simulation, L is the number of data points considered, v is a factor used to set the width of the function, and V_1 and V_2 are scaling factors. These functions were chosen, as they have a very similar form to the functions calculated from the Lorentz model, but are continuous at the resonance point. These emulations are not completely accurate representations of resonances, but they do help in gaining an understanding of how the data extraction method will operate at resonant frequencies.

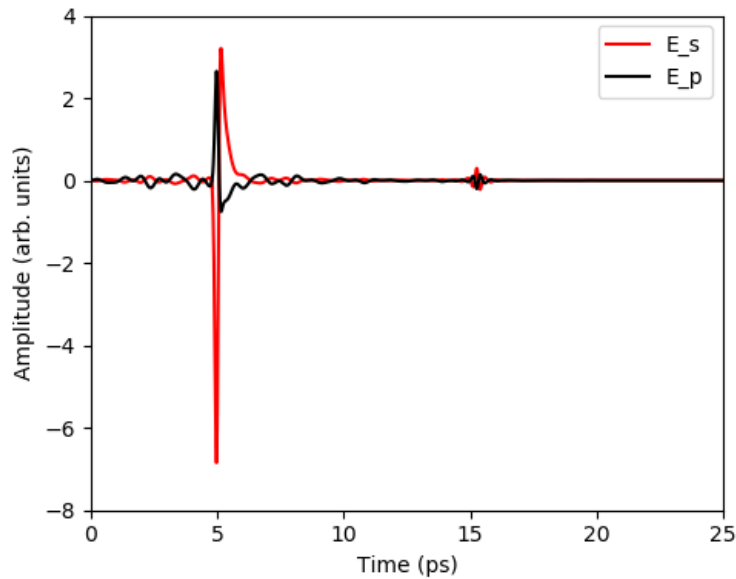


Figure 5.18: Simulated s-polarized reflection from a single layer sample when E_0 is considered purely s-polarized and simulated p-polarized reflection from a single layer sample when E_0 is considered purely p-polarized. This simulation is in the time domain and the sample in question is a $500\ \mu\text{m}$ single layer isotropic sample with a real refractive index of 3.2 and absorption coefficient of $30\ \text{cm}^{-1}$, with three resonances introduced to the data.

When a window is applied to the data in figure 5.18, the surface reflection is isolated. This process is shown in figure 5.19.

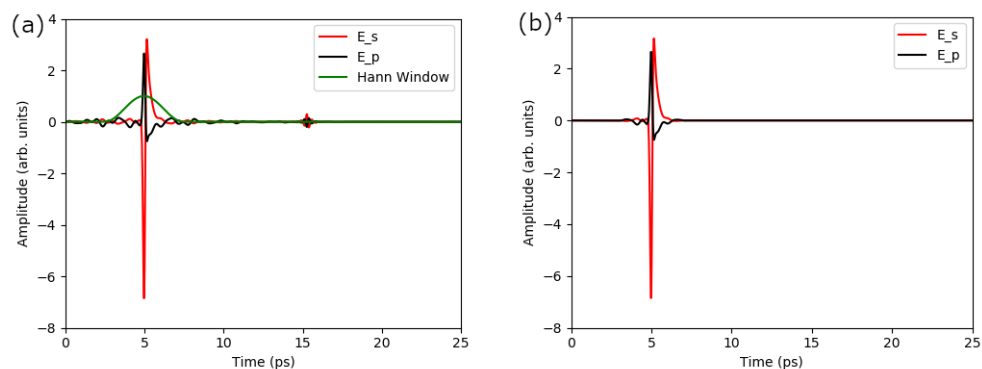


Figure 5.19: (a) The electric fields displayed in figure 5.18 and the Hann window which will be applied to it. (b) the electric fields produced by multiplying the window function shown in (a) with the electric fields in figure 5.18.

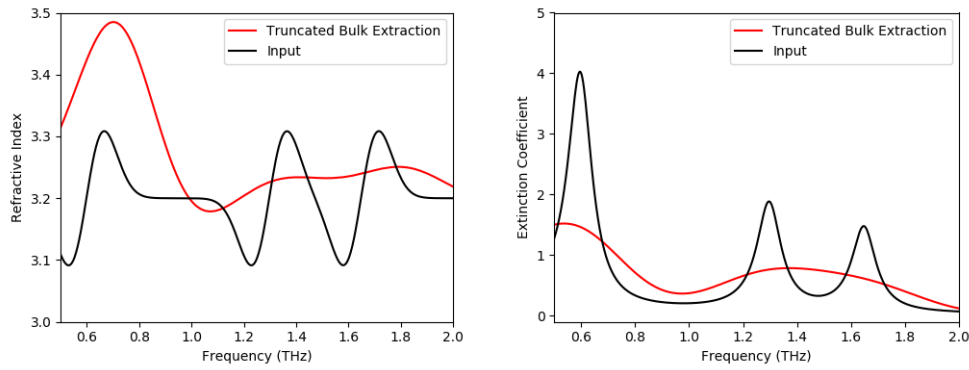


Figure 5.20: The complex refractive index extracted from the data in figure 5.19(b) by applying the bulk isotropic model. The black curve represents the values used in the simulation as input and the red curve represents the extracted values.

From figure 5.20, it can be seen that the data extracted by the bulk isotropic model from the data in figure 5.19 has been heavily smoothed. This result is very rudimentary and contains almost none of the finer details of the optical properties of the sample, thus it can be seen that this is not an ideal solution to extracting data from single layer samples, but this is however a strong initial guess for the single layer extraction method. This extracted complex refractive index is used as the initial guess, with each data point representing an initial guess for the frequency component it represents.

This complex refractive index is used as an initial guess in the single layer extraction method, and the resultant extracted complex refractive index is displayed in figure 5.21.

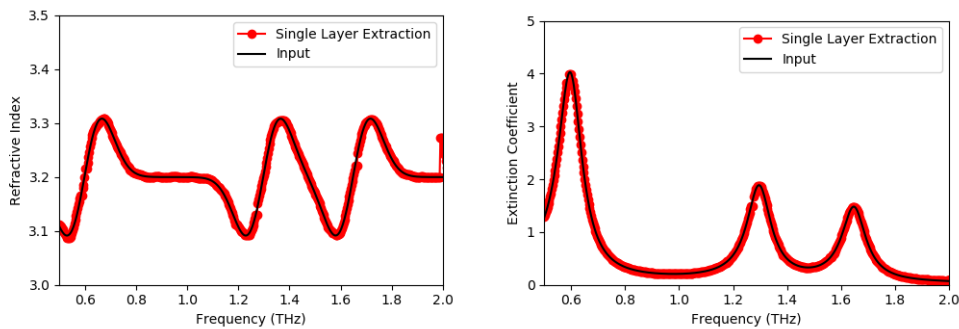


Figure 5.21: The complex refractive index extracted from the data in figure 5.18 by applying the single layer extraction method and utilizing the data in figure 5.20 as the initial guess.

The complex refractive index produced by applying the bulk isotropic model to the truncated data is a very good initial guess for the single layer extraction method and, for simulated data, has shown its ability to help the data extraction technique converge nearly perfectly to the expected values, as can be seen in figure 5.21.

This algorithm was applied to a myriad of simulated single layer samples with frequency independent real refractive indexes and absorption coefficients and gave near perfect results in all cases, as can be seen in the example extracted data in figure 5.22

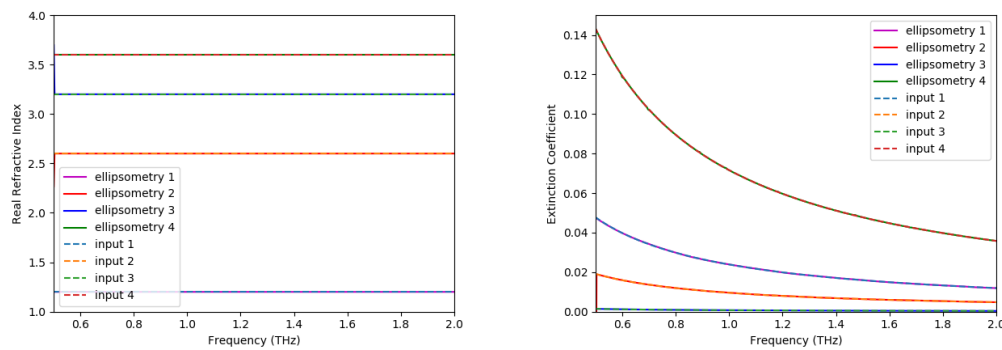


Figure 5.22: The complex refractive indexes extracted from four samples with different frequency independent real refractive indexes and absorption coefficients.

The introduction of resonances into the data can however negatively impact the ability of the algorithm to converge to the correct values, as can be seen in figure 5.23. This is in part due to the resonances being heavily smoothed and spread to surrounding frequencies in the windowed initial guess.

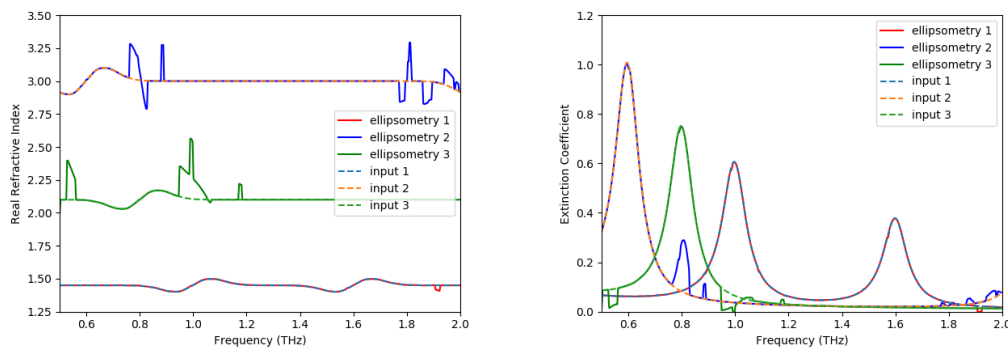


Figure 5.23: The complex refractive indexes extracted from three samples with different real refractive indexes and absorption coefficients and resonances present in their spectra.

During these tests, LULU of order 1 was applied to the data to remove the numerical errors resulting from convergence errors and the thickness extraction technique was applied, but no error was added to the initial guess of the thickness.

5.3 Single layer isotropic medium followed by bulk isotropic sample model

Our initial goal is to develop a system for analyzing samples in aqueous solution. A cuvette is required to mount these samples in the setup. The cuvette and aqueous sample form a two-layer sample, where the first layer, the cuvette, is a single layer isotropic medium and the second layer, the aqueous sample, is a bulk isotropic sample.

5.3.1 Two layer ellipsometric method

A simple approach to a two layer system consisting of a single layer isotropic sample and a bulk isotropic sample is to isolate the first and second pulse in the series of reflections from the sample and then solve them separately using the bulk isotropic method.

Consider an aqueous solution inside a silicon cuvette. This can be treated as a combination of the bulk isotropic model and the single layer isotropic model. The Si wall is a thin transparent layer on top of a optically dens bulk sample. The Silicon layer can be described by the model in section 5.2 and the water solution as the model in section 5.1.

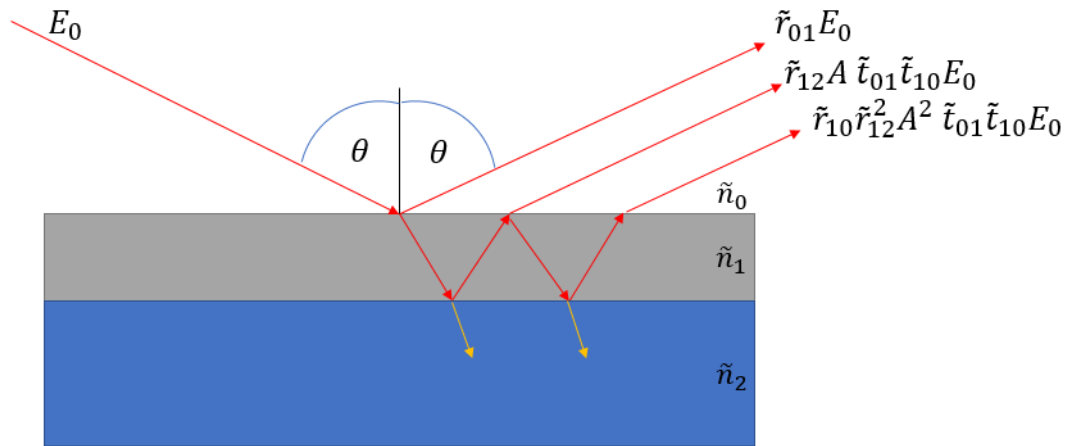


Figure 5.24: Diagram depicting light matter interaction with a single layer isotropic medium layered on top of a bulk isotropic sample. Both surface reflections and internal reflections are measurable for the single layer medium, but only surface reflections are measurable for the bulk isotropic sample.

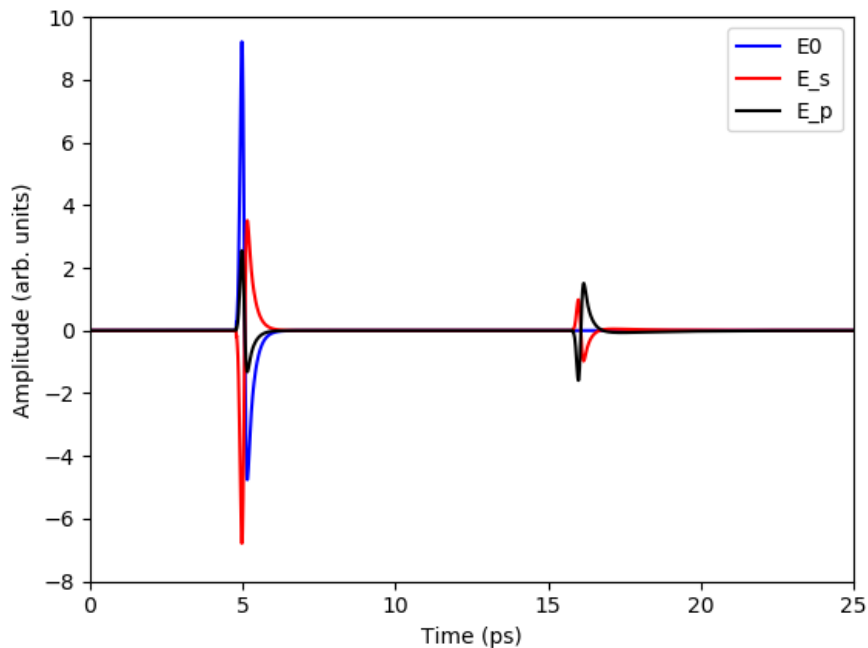


Figure 5.25: Simulated electric field E_0 , simulated s-polarized reflection of incident s-polarized electric field E_{0s} and p-polarized reflection of incident p-polarized electric field E_{0p} , where $E_{0s} = E_{0p} = E_0$. The simulated sample is a $500 \mu\text{m}$ single layer isotropic medium with a real refractive index of 3.4177 and absorption coefficient of 0.03 cm^{-1} deposited on a 2 mm bulk isotropic sample with a real refractive index of 2 and absorption coefficient of 200 cm^{-1} .

The measured time-domain data for a single layer medium deposited on a bulk isotropic sample, as depicted in figure 5.25, contains a pulse reflected from the surface of the single layer isotropic medium, followed by a series of internal reflections that occur inside the single layer medium.

Assuming nothing is known about either layer, one of the simplest solutions is to implement truncation. Due to the use of FFT functions in the data analysis process, it is preferable to use a smooth windowing function to truncate the data, as opposed to a block function. For our purposes, the Hann window is ideal [43].

A Hann window is applied to the data to select out the first pulse in the pulse train. This process can be seen in figure 5.26. This first pulse is the reflection from the surface of the single layer isotropic medium, and only contains information about this layer. The complex refractive index of this layer is extracted from this truncated data via the bulk isotropic model, as described in section 5.1.

$$E(t)G_1(t) = \tilde{r}_{01}G_1(t)E_0(t) \quad (5.3.1)$$

The window function, $G_1(t)$, is multiplied on a point-by-point bases with the measured electric field, $E(t)$, in the time domain. This results in only the initial reflection remaining in the data, as seen in figure 5.26.

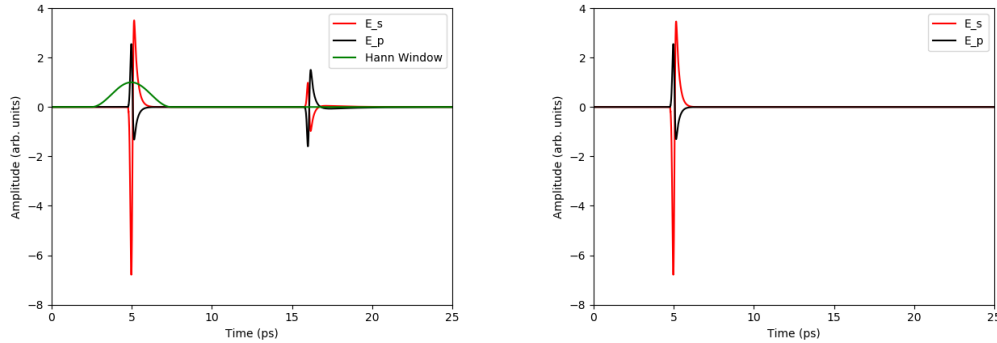


Figure 5.26: A Hann window is applied to the data represented in figure 5.25. This truncates the data to the first pulse, which represents the pulse reflected from the surface of the single layered isotropic medium.

Next, a Hann window is applied to the data, which isolates the second pulse in the pulse train. An illustration of this process can be seen in figure 5.27. This pulse represents the initial electric field transmitted into the single layered isotropic medium, propagated through the medium, reflected off the interface between the single layered isotropic medium and the bulk isotropic sample, propagated through the medium again and transmitted out of the sample.

$$E(t)G_2(t) = \tilde{t}_{01}A\tilde{r}_{12}\tilde{t}_{10}G_2(t)E_0(t) \quad (5.3.2)$$

Similar to the window applied to truncate the data to the first reflection, the second window, $G_2(t)$, is multiplied with the measured electric field, $E(t)$, truncating the data to only represent the electric field reflected from the interface between the single layer medium and the bulk isotropic sample, as shown in figure 5.27.

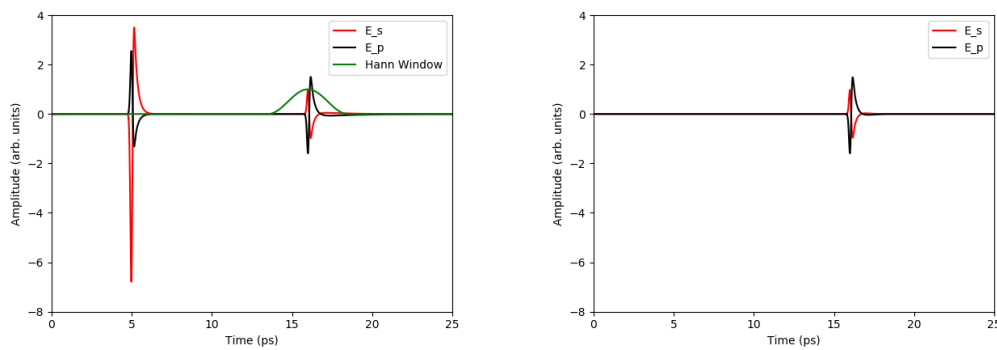


Figure 5.27: A second Hann window is applied to the data represented in figure 5.25. This truncates the data to the second pulse, which represents the pulse reflected from the interface between the single isotropic medium and the bulk isotropic sample.

With the optical constants of the first layer known, the transmission coefficient and attenuation coefficients can be removed from the data. This leaves the reflection coefficient for the interface between the single layered isotropic medium and bulk isotropic sample. The bulk isotropic model is applied to extract the complex refractive index of the bulk isotropic sample as illustrated in figure 5.28.

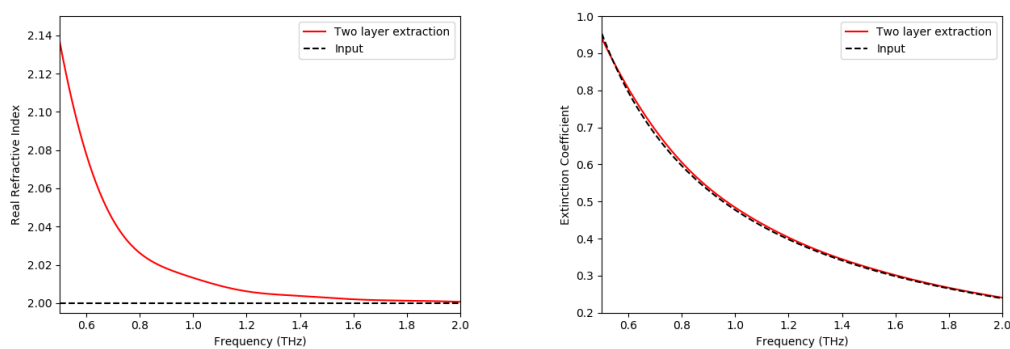


Figure 5.28: The complex refractive index extracted of the bulk sample (n_2 and its corresponding extinction coefficient) from the data presented in figure 5.25 via the two layer ellipsometric method.

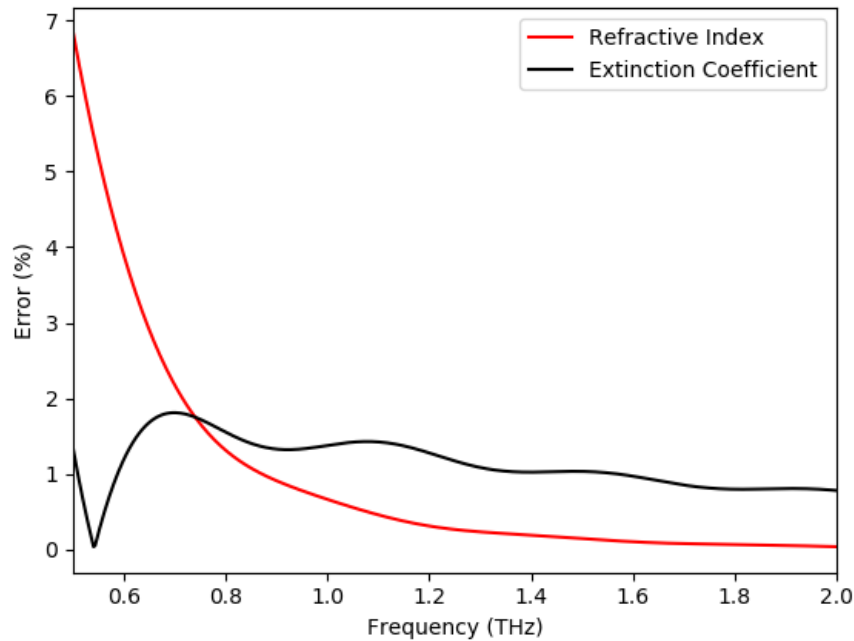


Figure 5.29: The error calculated for the extracted real refractive index and extinction coefficient data shown in figure 5.28.

From figure 5.29 it can be seen that a windowing error is present in the extracted complex refractive index, but the extracted values are still fairly accurate. There is a comparatively large error in the real refractive index at lower frequencies, which rapidly falls as the frequency increases. This is a byproduct of the windowing function. Increasing the size of the window lowers this error, but as the size of the window is increased, this will also increase the effects of noise and other signals present on the data, which becomes relevant when considering experimentally measured data.

This algorithm is independent of the sample thickness and LULU is not applied to the data.

5.3.2 Self-reference method

Another method for extracting data for a two layer system such as the one discussed in this section was proposed by Jepsen *et al* [21]. This method employs reflection spectroscopy, as opposed to ellipsometry. It is preferable to work with a system with a pure s- or p-polarization, as this greatly simplifies the mathematics used to extract optical parameters from measured data.

In reflection spectroscopy, to extract information from measured data, a reference measurement is required so that the electric field incident on the

sample can be removed from the calculations. Switching between a reference sample and a sample of interest can introduce miss-alignments in the system, which can introduce errors to the extracted information.

The reference sample used in the Self-reference case is the same as the sample which will be investigated, except the second layer is nitrogen, as opposed to a liquid sample of interest.

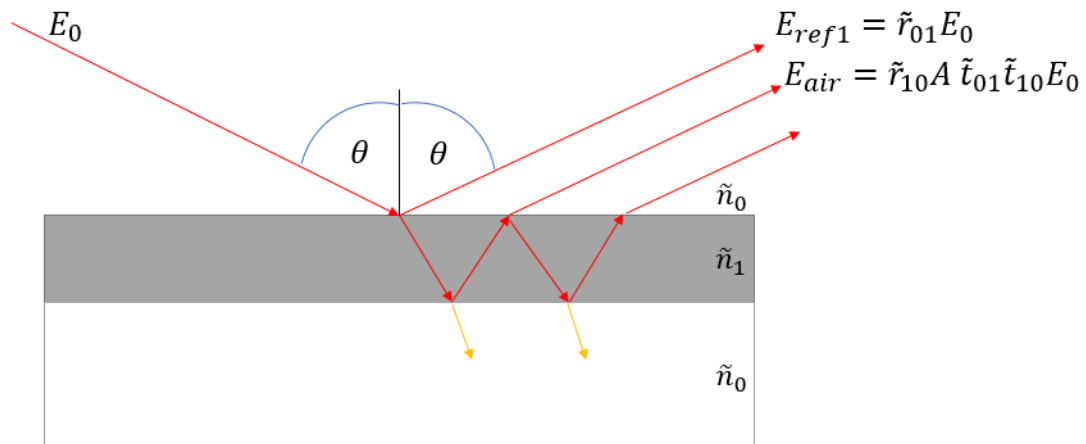


Figure 5.30: Diagram depicting light matter interaction with a single layer isotropic medium. This measurement will act as the reference measurement.

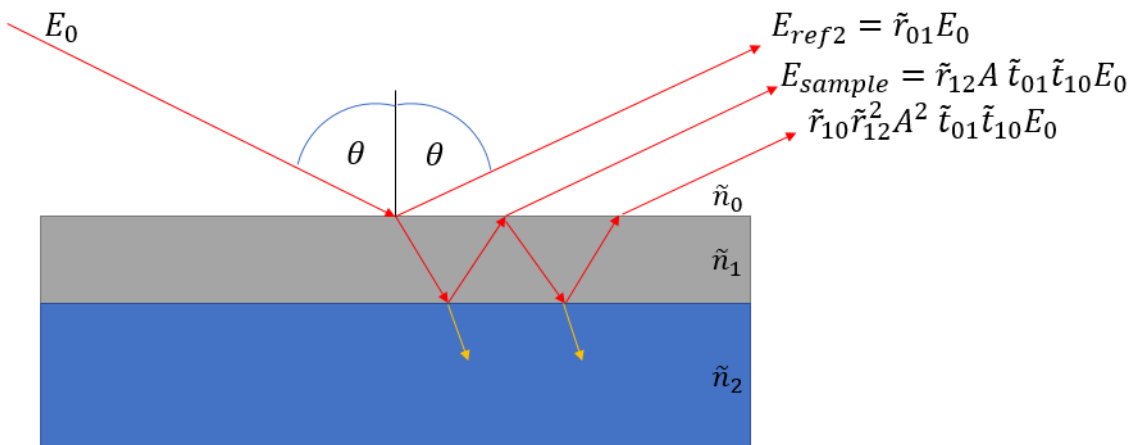


Figure 5.31: Diagram depicting light matter interaction with a single layer isotropic medium layered on top of a bulk isotropic sample.

The first layer is used as a localized reference, to correct for any phase error introduced by changing between the sample and the reference. This first layer

is considered to not change between measurements, thus any changes observed for this layer between changing samples can be used to calculate corrections for the entire measurement. This method employs truncation to isolate the first and second reflections for both the sample and reference. For a pure p-polarized system, it can be shown that [21]:

$$\tilde{r}_{12}(f) = \frac{\tilde{r}_{10}(f)C_2(f)}{C_1(f)} \quad (5.3.3)$$

$$C_1(f) = \frac{E_{air}(f)}{E_{ref1}(f)} \quad (5.3.4)$$

$$C_2(f) = \frac{E_{sample}(f)}{E_{ref2}(f)} \quad (5.3.5)$$

where $\tilde{r}_{12}(f)$ is the reflection between the first and second layer of the sample, $E_{ref1}(f)$ and $E_{air}(f)$ are the FFTs of the truncated first and second reflections from the reference sample, as shown in figure 5.30, and $E_{ref2}(f)$ and $E_{sample}(f)$ are the FFTs of truncated first and second reflections from the sample of interest, as shown in figure 5.31. The reference material should be well characterized, thus allowing for the calculation of $\tilde{r}_{10}(f)$, which is the expected reflection coefficient between the reference material and air. The complex refractive index of the unknown sample can then be extracted from $\tilde{r}_{12}(f)$. For a pure p-polarized system, the following solution was calculated by inverting equation 2.3.6 to make $\tilde{n}(f)$ the subject of the equation:

$$\tilde{r}_{12}(f) = \frac{\tilde{n}(f)\sqrt{1 - \frac{\sin^2\theta}{\tilde{n}_{ref}^2(f)} - \tilde{n}_{ref}(f)\sqrt{1 - \frac{\sin^2\theta}{\tilde{n}^2(f)}}}{\tilde{n}(f)\sqrt{1 - \frac{\sin^2\theta}{\tilde{n}_{ref}^2(f)} + \tilde{n}_{ref}(f)\sqrt{1 - \frac{\sin^2\theta}{\tilde{n}^2(f)}}}} \quad (5.3.6)$$

$$\begin{aligned} 0 &= (\tilde{r}_{12}(f) - 1)^2(\tilde{n}_{ref}^2(f) - \sin^2\theta)\tilde{n}^4(f) \\ &\quad - (\tilde{r}_{12}(f) + 1)^2\tilde{n}_{ref}^4(f)\tilde{n}^2(f) \\ &\quad + (\tilde{r}_{12}(f) + 1)^2\tilde{n}_{ref}^4(f)\sin^2\theta \end{aligned} \quad (5.3.7)$$

$$Z_1(f) = (\tilde{r}_{12}(f) - 1)^2(\tilde{n}_{ref}^2(f) - \sin^2\theta) \quad (5.3.8)$$

$$Z_2(f) = (\tilde{r}_{12}(f) + 1)^2\tilde{n}_{ref}^4(f) \quad (5.3.9)$$

$$\tilde{n}^2(f) = \tilde{\epsilon}(f) = \frac{Z_2(f) + \sqrt{Z_2^2(f) - 4Z_1(f)Z_2(f)\sin^2\theta}}{2Z_1(f)} \quad (5.3.10)$$

$$n(f) = \sqrt{\frac{\text{Re}[\tilde{\epsilon}(f)] + \sqrt{\text{Re}[\tilde{\epsilon}(f)]^2 + \text{Im}[\tilde{\epsilon}(f)]^2}}{2}} \quad (5.3.11)$$

$$\kappa(f) = \frac{-\text{Im}[\tilde{\epsilon}(f)]}{2n(f)} \quad (5.3.12)$$

The complex refractive index of the sample is represented by $\tilde{n}(f)$, the complex dielectric constant by $\tilde{\epsilon}(f)$ and the complex refractive index of the

reference material is $\tilde{n}_{ref}(f)$. The angle of incidence is θ , the real refractive index of the sample is $n(f)$ and the extinction coefficient of the material is $\kappa(f)$. The reflection coefficient for the interface between the sample and reference material, $r_{12}(f)$, is calculated by equation 5.3.3.

As an example, let us consider the sample in figure 5.32.

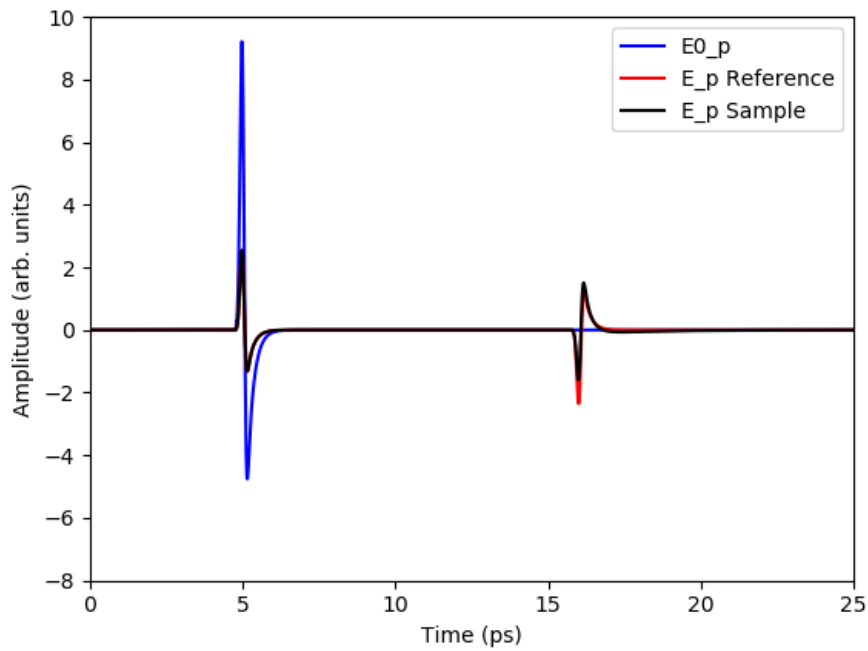


Figure 5.32: Simulated p-polarized electric field E_{0p} , simulated p-polarized reflection of incident p-polarized electric field E_{0p} from cuvette without the sample present and simulated p-polarized reflection of incident p-polarized electric field E_{0p} from cuvette with the sample present. The simulated cuvette is a $500 \mu\text{m}$ single layer isotropic medium with a real refractive index of 3.4177 and absorption coefficient of 0.03 cm^{-1} and the sample is a 2 mm bulk isotropic medium with a real refractive index of 2 and absorption coefficient of 200 cm^{-1} .

The windowing function we employ is the Hann window and it is used in a similar fashion to the case in section 5.3.1, which is shown in figures 5.33 and 5.34.

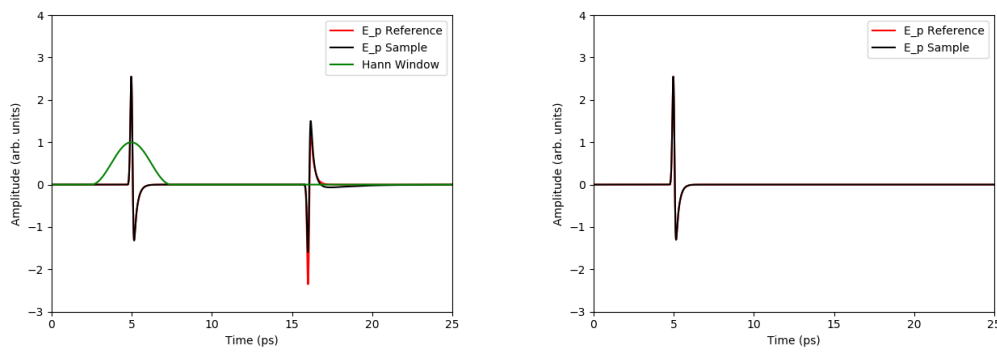


Figure 5.33: A Hann window is applied to the data represented in figure 5.32. This truncates the data to the first pulse, which represents the pulse reflected from the surface of the single layered isotropic medium. This is done for both the reference and the sample.

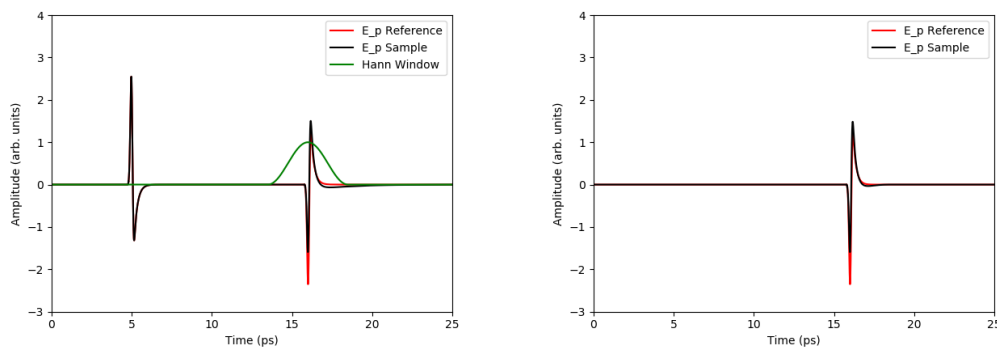


Figure 5.34: A second Hann window is applied to the data represented in figure 5.32. This truncates the data to the second pulse, which represents the pulse reflected from the interface between the single isotropic medium and the bulk isotropic sample. This is done for both the reference and the sample.

The windowed data in figure 5.33, for the reference, is used as E_{ref1} and the data for the sample is used as E_{ref2} . The windowed data in figure 5.34, for the reference, is used as E_{air} and the data for the sample is used as E_{sample} . The self-reference data extraction method is applied to this data and the complex refractive index is extracted, which can be seen in figure 5.35.

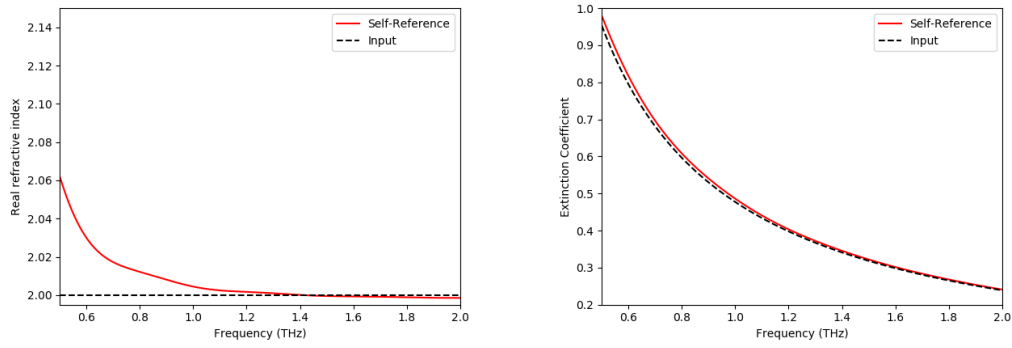


Figure 5.35: The complex refractive index extracted from the data presented in figure 5.32 via the self-reference method.

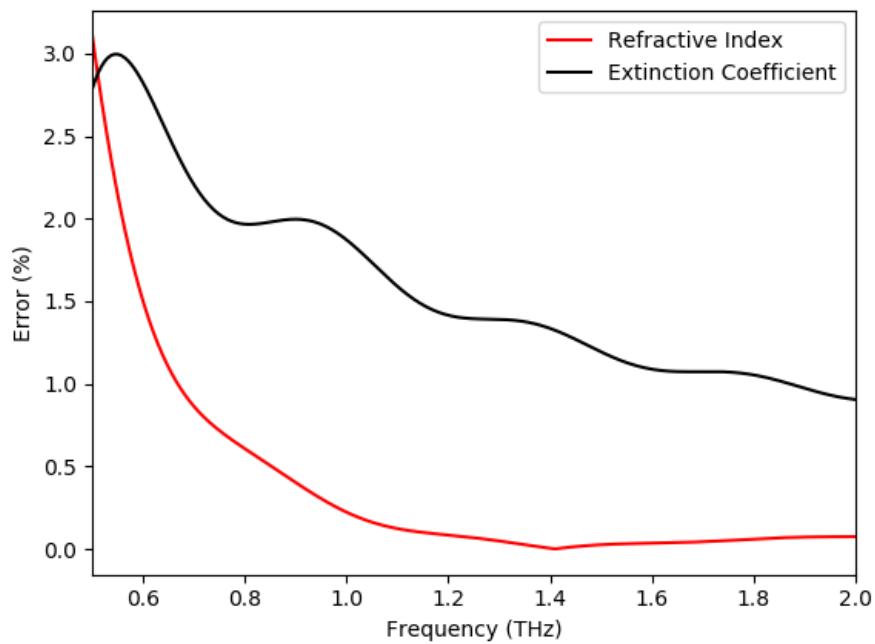


Figure 5.36: The error calculated for the extracted real refractive index and extinction coefficient data shown in figure 5.35.

From figure 5.36 it can be seen that a windowing error is present on the extracted complex refractive index, but the extracted values are still fairly accurate. Similar to the two-layer ellipsometric method used in section 5.3.1,

there is a comparatively large error in the real refractive index at lower frequencies, which rapidly falls as the frequency increases. This is a byproduct of the windowing function. The windowing error is however smaller than the error present in the two-layer ellipsometric method (section 5.3.1). This is not surprising, as the method should inherently correct for this error, as it should be similar in both the reference data and the sample data.

5.3.3 Comparison

As a simple comparison between the two layer ellipsometric method, section 5.3.1, and the self-reference method, section 5.3.2, let us consider four different liquid samples. All four samples have a thickness of 2 mm and are deposited on a $500\ \mu\text{m}$ single layer sample with a real refractive index of 3.4177 and absorption coefficient of $0.03\ \text{cm}^{-1}$. Sample one has a refractive index of 2.0 and absorption coefficient of $80.0\ \text{cm}^{-1}$, sample two has a refractive index of 1.95 and absorption coefficient of $79.0\ \text{cm}^{-1}$, sample three has a refractive index of 1.9 and absorption coefficient of $78.0\ \text{cm}^{-1}$ and sample four has a refractive index of 1.8 and absorption coefficient of $76.0\ \text{cm}^{-1}$. Samples one, two and three each had resonances added at 1.3 and 1.65 THz, while sample four had a resonances added at 1.35 and 1.7 THz. The simulated electric fields can be seen in figure 5.37.

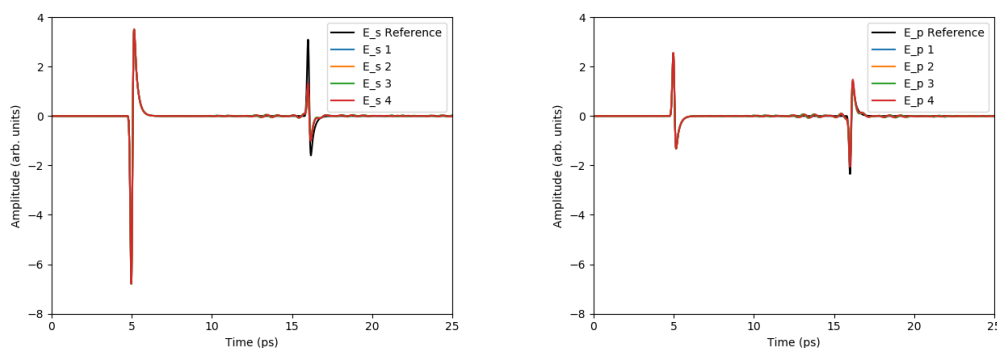


Figure 5.37: Time data produced for several different bulk samples deposited on a single layer isotropic medium.

The simulated electric fields shown in figure 5.37 were used to test both the two layer ellipsometric method and the self-reference method.

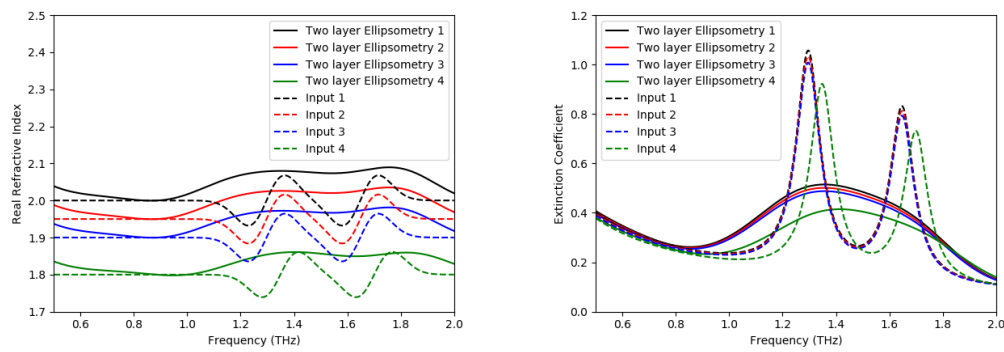


Figure 5.38: The complex refractive indexes extracted from the data presented in figure 5.37 via the two layer ellipsometric method.

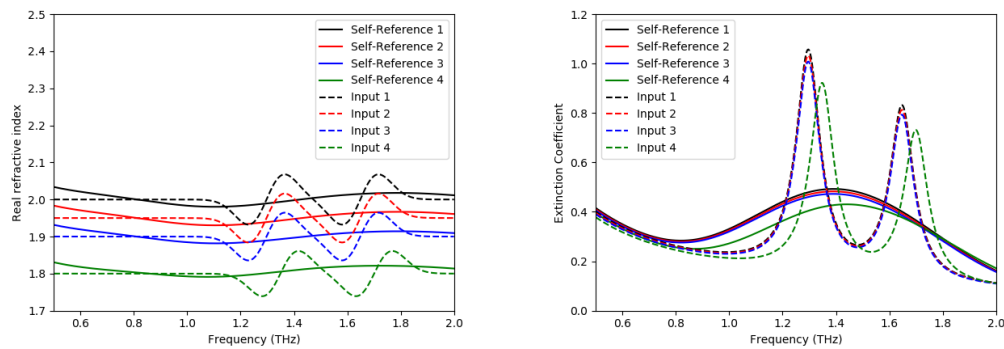


Figure 5.39: The complex refractive indexes extracted from the data presented in figure 5.37 via the self-reference method.

From figures 5.38 and 5.39 we find that both the two layer ellipsometric method and self-reference method extract similar values for the extinction coefficient with the peak shift being visibly more pronounced in the two layer ellipsometry data, but only to a minor extent. Both methods extracted similar values for the main refractive index and extinction coefficient of each sample and the values of the different samples are clearly distinguishable from each other. The most noteworthy difference between the two sets of extracted complex refractive indexes is the difference in how the resonances effected the extracted refractive index data. In the case of the two layer ellipsometric method, the refractive index is lifted by the resonances, while in the self-reference case the resonances are effectively smoothed away in the refractive index data.

From these results we find that both methods are useful for distinguishing different liquid samples from each other. When considering the data not at the resonances, both methods offer similar results. The ellipsometric method displays the resonances in the complex refractive index more prominently than the self-reference method, but as these resonances are not clearly resolved, this might not always be a favourable result, hence the usefulness of this depends on the application of the data.

The self reference method has the advantage of only needing one set of data per sample, assuming the reference material stays the same between different samples. In the case of the two-layer ellipsometry method two sets of data measured in the s- and p-polarization directions are needed. This in turn has the effect of making the self-reference method more robust with regards to miss-alignment and error in the angle of incidence. The disadvantage of this method when compared to the two layer ellipsometric method is that the reference material needs to be well characterized and that resonances in the extracted complex refractive index will be less pronounced than in the ellipsometric case.

Chapter 6

Results and discussion

The constructed time domain THz ellipsometer and the various data extractions techniques that were developed, were tested by performing measurements on appropriate samples, to illustrate the capabilities and determine the limitations of the constructed ellipsometer. At least one sample was measured for each data extraction technique discussed in section 5.

6.1 System transfer function measurement

In order to measure the system transfer function of the constructed system, a silver mirror was used as the sample. For this sample, reflection coefficients of -0.999 for s-polarized light and 0.997 for p-polarised light are expected, as the complex refractive index for silver at 1 THz is $531 - 689i$ [31].

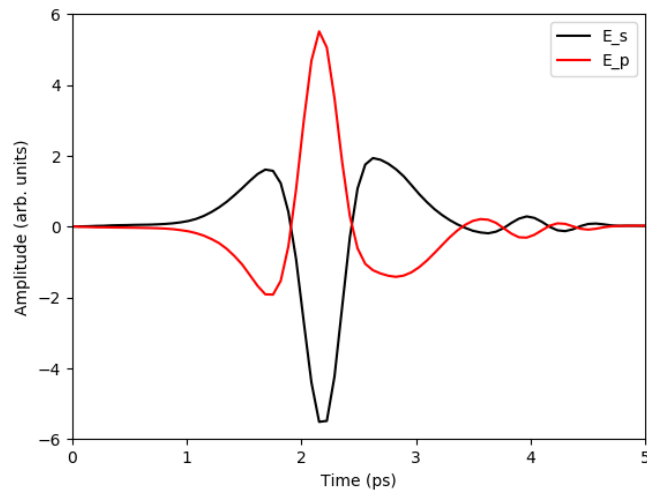


Figure 6.1: Time-domain data measured for a silver mirror. The absorption lines present in the spectrum are from residual water vapour.

From the mirror measurements, as seen in figure 6.1, and the simulation method, described in section 4, corrections to the amplitude and phase are calculated.

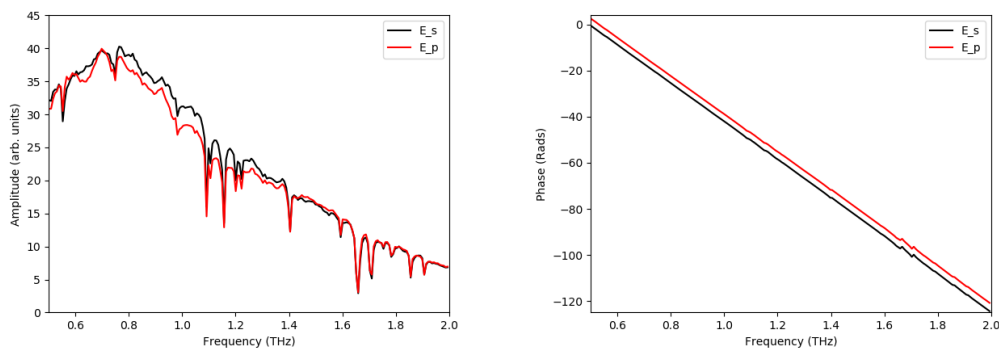


Figure 6.2: The absolute amplitude and phase of the Fourier transforms of the data represented in figure 6.1.

The resonances present in the data FFT data, as seen in figure 6.2, are from water vapour still present in the system. The path length through the system is 1.65 m, as a result it is difficult to remove all water from the environment.

Simulated reflection coefficients ($\tilde{r}_{s\text{sim}}(f)$ and $\tilde{r}_{p\text{sim}}(f)$) are calculated by using the simulation technique from chapter 4. A flat complex refractive index

of $531 - 689i$ was used. The ratio between $\tilde{r}_{sim}(f)$ and $\tilde{r}_{psim}(f)$ was taken and the absolute amplitude ($A_{simulated}$) and unwrapped phase ($\Delta P_{simulated}$) of this ratio was calculated. These values are then compared with those from the Fourier transformed data of the measurements, as seen in figure 6.2.

$$Cor_A = \frac{A_{measured}}{A_{simulated}} \quad (6.1.1)$$

$$Cor_P = \Delta P_{measured} - \Delta P_{simulated} \quad (6.1.2)$$

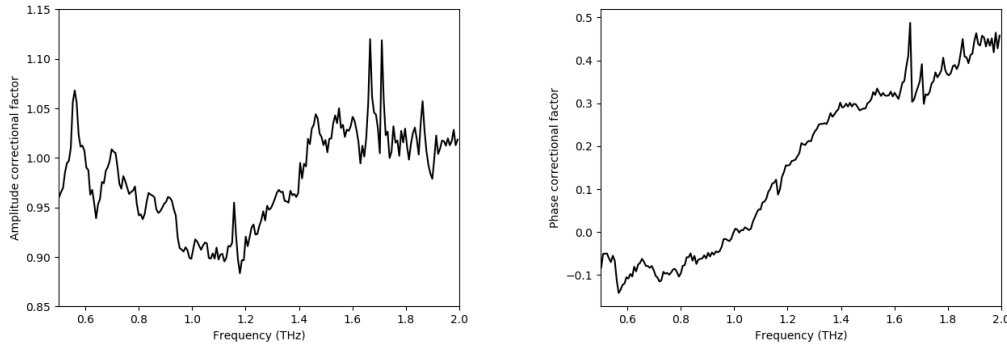


Figure 6.3: The corrections to the amplitude, Cor_A , and phase, Cor_P , calculated for the data plotted in figure 6.2

The correctional values for our system were calculated and can be seen in figure 6.3. These corrections represent the system transfer function, and can be used as a correction factor on measured data in order to eliminate the effect of the system on the final result.

As these correctional values are dependent on the angle of incidence and the water vapour levels remaining in the system, new measurements on the mirrors were performed each day before sample measurements were taken and correction values were calculated for that day's data from these mirror measurements.

These correctional values were applied to all data in the following sections during data extraction, except for the self-reference method, as this method only used p-polarized light.

6.2 Bulk isotropic sample: Thick float glass

As discussed in section 5.1, bulk isotropic samples are samples from which only a surface reflection is expected and internal reflections should not be present in the measured data.

A 2.73 mm thick piece of float glass was measured in the setup. This sample was chosen due to fulfilling several criteria. We had extracted optical properties for the sample via a commercial THz transmission setup in the range 0.5 THz to 0.9 THz, thus the optical properties of the material were known for this range. The range was limited due to the strong absorption of the sample at higher frequencies. Most importantly, the sample was of sufficient optical thickness, and as such did not allow for measurable internal reflections.

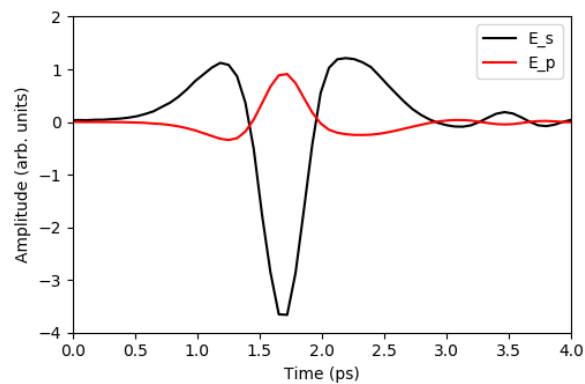


Figure 6.4: Time domain measurement of s- and p-polarized electric fields reflected from a 2.73 mm bulk float glass sample.

The data represented in figure 6.4 was analyzed via the bulk isotropic data extraction method, described in section 5.1. The results can be seen in figure 6.5.

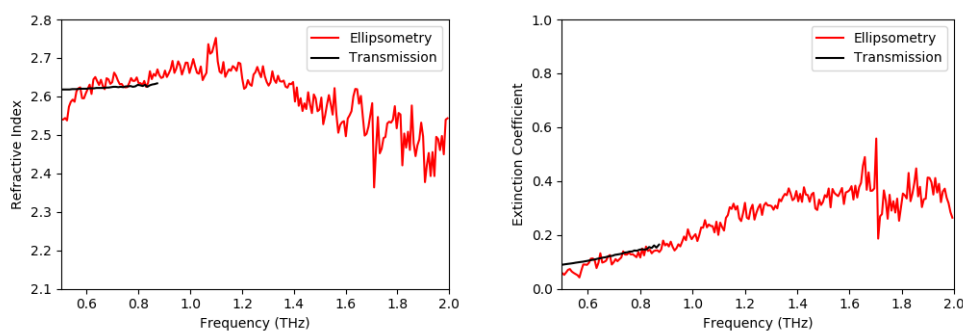


Figure 6.5: The complex refractive index extracted from the data presented in figure 6.4 via the bulk isotropic data extraction technique (red curve) in comparison to THz transmission data (black curve).

The extracted complex refractive index values for the float glass sample matched the values extracted via the commercial transmission system (error between expected and extracted values is less than 2.8%), as can be seen when comparing the different data sets (red and black curves) in figure 6.5. The trend followed by the refractive index and extinction coefficient extracted by the ellipsometric system and transmission system bore high similarity to one another. Due to strong absorption of the float glass, the ellipsometry measurements were able to measure the complex refractive index over a much wider frequency range than the transmission measurement (0.5 THz to 2 THz compared to 0.5 THz to 0.9 THz).

6.3 Single layer isotropic

Single layered isotropic samples, as discussed in section 5.2, are dielectric samples which are non-depolarizing. These samples are of such a nature that measurable internal reflections occur in them. For these measurements a strongly absorbing thin sample of borosilicate glass, a highly transparent sample of undoped high resistivity silicon and a highly transparent sample of lightly n-type doped silicon were chosen.

6.3.1 Borosilicate Glass

A 0.97 mm borosilicate glass sample was measured using our time domain THz ellipsometer. The extracted nonlinear refractive index is compared to the values obtained using a commercial THz-TDS transmissions spectrometer in the 0.5 THz to 1.4 THz region. As can be seen in figure 6.6 the sample displays a very weak internal reflection, barely noticeable in the time domain data.

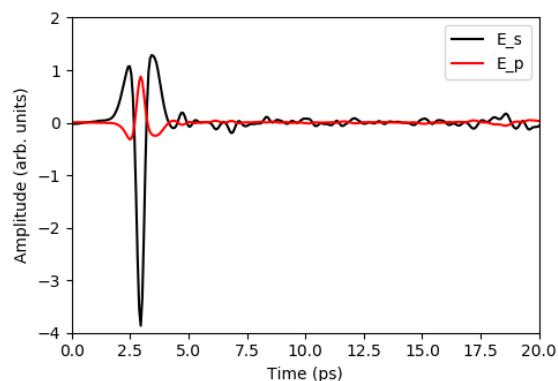


Figure 6.6: Time domain measurement of s- and p-polarized electric fields reflected from a 0.97 mm single layer glass sample.

The single layer data extraction method, as described in section 5.2, was applied to the data represented in figure 6.6. An initial thickness guess of 0.97 ± 0.01 mm, as measured by vernier caliper with $10 \mu\text{m}$ accuracy, was used for the calculation. The extracted results are presented in figure 6.7.

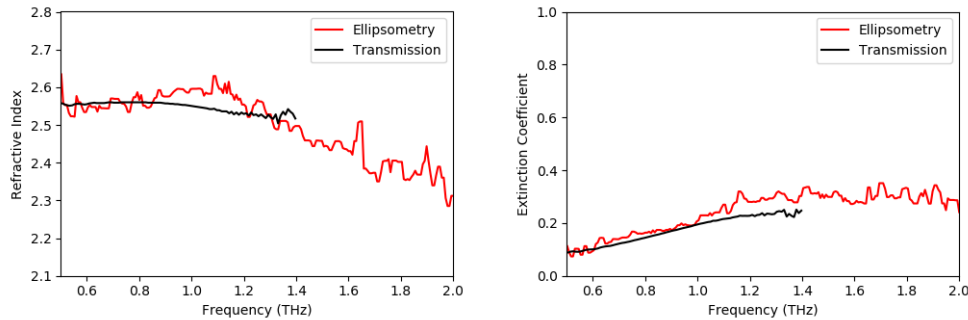


Figure 6.7: The complex refractive index extracted from the data presented in figure 6.6 via the single layer isotropic data extraction technique (red curve) in comparison to THz transmission data (black curve).

The single layer extraction method converged to a sample thickness of 0.964 mm, which is clearly within the error margin of the vernier caliper, and produced the complex refractive index displayed in figure 6.7. The complex refractive index extracted from the ellipsometry data agrees within 10% of the values measured with the transmission spectrometer, in the range 0.5 THz to 1.4 THz. However, the ellipsometer was able to measure the complex refractive index for the interval 0.5 THz to 2.0 THz, where the optical density of sample limited the range in which the transmission spectrometer could reliably determine the complex refractive index of the borosilicate sample.

6.3.2 High resistivity silicon

High resistivity silicon has very well researched optical properties in the THz region [20–22], thus it is ideal for testing the functionality of the system.

An undoped $500 \mu\text{m}$ thick silicon wafer was used as sample the in the THz ellipsometer and the complex refractive index was measured. The measured data can be found in figure 6.8.

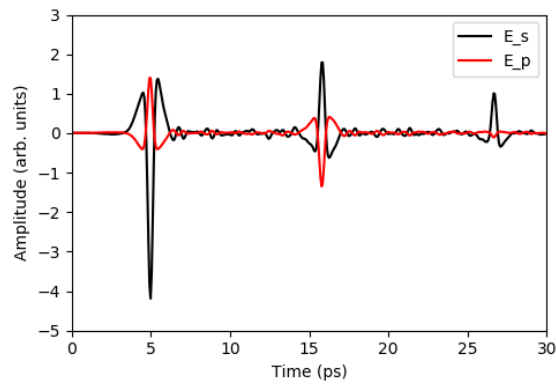


Figure 6.8: Time domain measurement of s- and p-polarized electric fields reflected from a 0.5 mm single layer undoped silicon sample.

The single layer ellipsometric data extraction technique is applied to the data presented in figure 6.8. The resultant complex refractive index which was extracted can be found in figure 6.9.

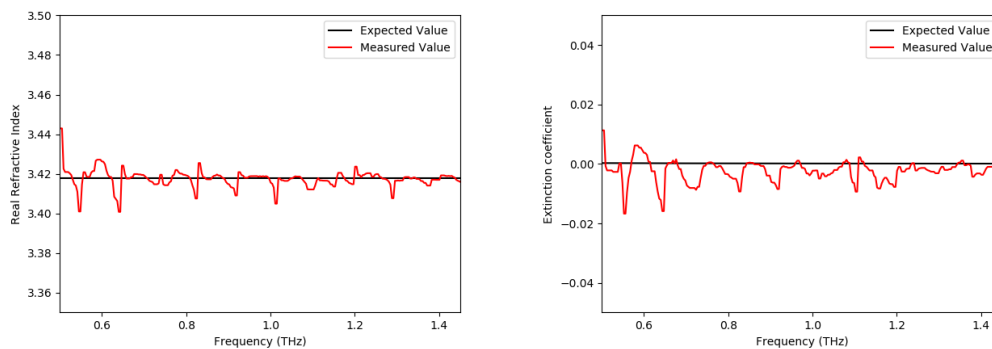


Figure 6.9: The complex refractive index extracted from the data presented in figure 6.8 via the single layer isotropic data extraction technique (red curve) compared to the expected value (black line) from literature [20–22].

The sample is effectively transparent, as can be seen from the extinction coefficient in figure 6.9. If we compare the real refractive index extracted by the single layer extraction method with data from literature [20–22] we find we have achieved a nominal average error of 0.18%. A spectral representation of our error can be found in figure 6.10. The extremely low extinction coefficient results in slightly larger errors when compared to literature values (average absolute difference of 0.003), due to the difficulty of the extraction algorithm converging when the extinction coefficient is essentially zero.

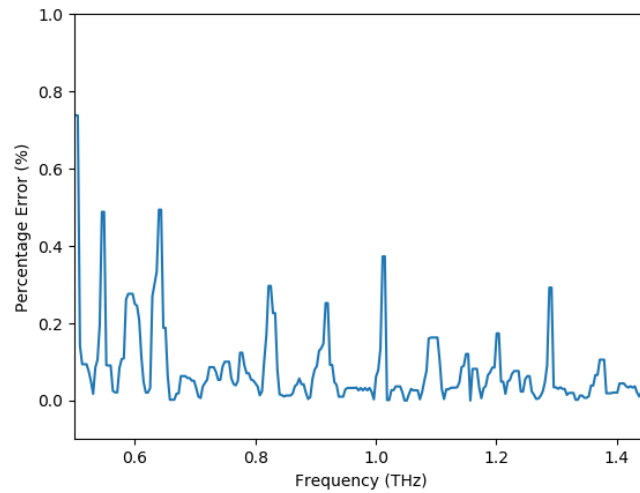


Figure 6.10: The error found when comparing our extracted real refractive index with the value found in literature [20–22].

The extracted extinction coefficient in figure 6.9 can be converted to the absorption coefficient by use of equation 2.2.8. The calculated absorption coefficient can be seen in figure 6.11.

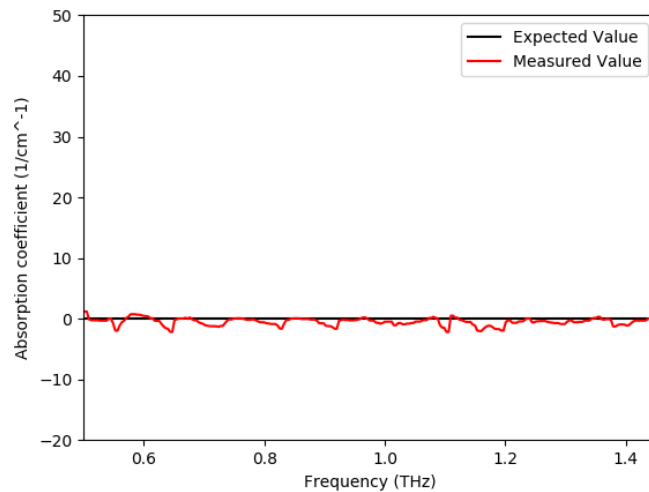


Figure 6.11: The absorption coefficient calculated from the data presented in figure 6.9 via equation 2.2.8 (red curve) compared to the expected value (black line) from literature [20–22].

The extracted values found in figure 6.9 and figure 6.11 can be compared to the THz ellipsometry results obtained by Xuequan *et al* [1], which can be seen in figure 6.12.

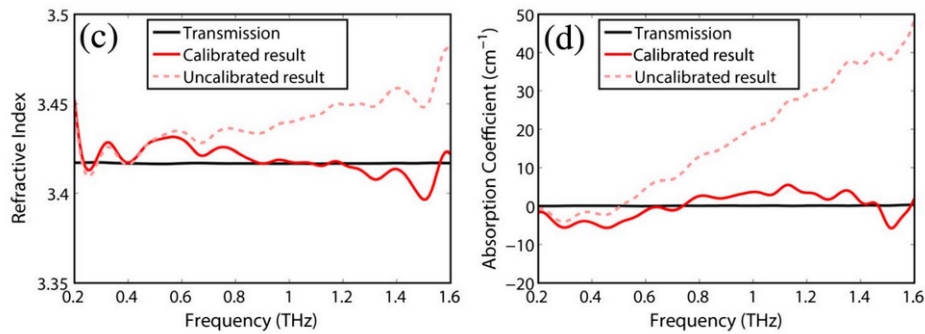


Figure 6.12: (c) The real refractive index and (d) absorption coefficient of high resistivity silicon extracted by Xuequan *et al* [1].

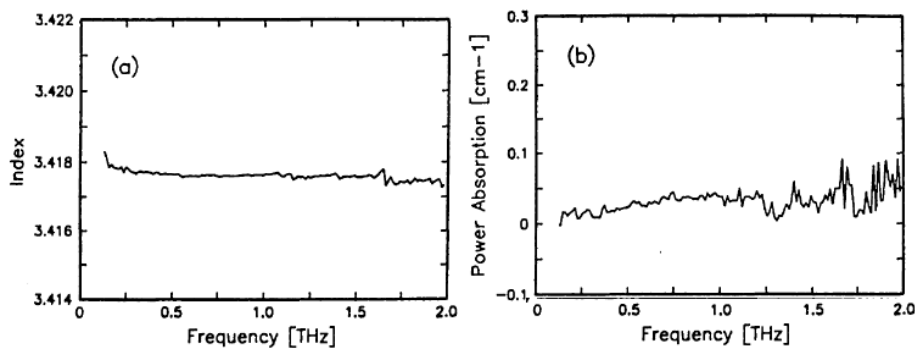


Figure 6.13: (a) The real refractive index and (b) absorption coefficient of high resistivity silicon extracted in transmission by Grischkowsky *et al* [22].

By comparing our extracted values with those extracted by Xuequan *et al* [1], we find that our values are noticeably closer to those extracted in literature via transmission, as seen in figure 6.13 [22], especially in the extracted absorption coefficient.

6.3.3 Lightly n-type doped silicon

A measurement was performed on a doped silicon sample, to compare with the undoped silicon sample in section 6.3.2. A lightly n-type doped silicon sample

was chosen. The sample has a resistivity of 1800-2000 Ωm and is 375 μm thick. The time domain data measured for this sample is displayed in figure 6.14.

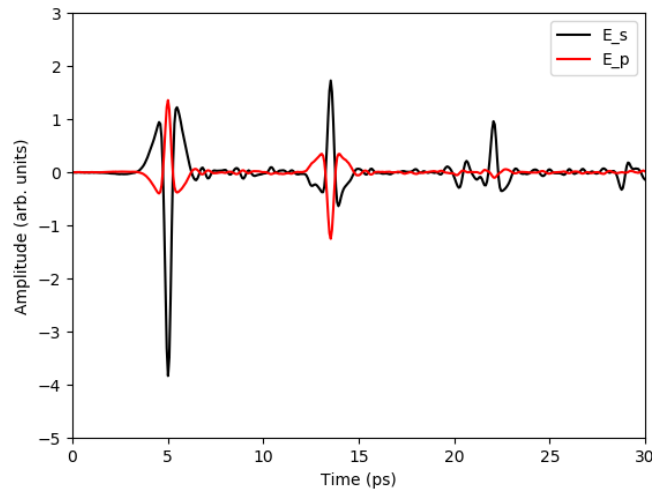


Figure 6.14: p- and s-polarized electric fields reflected from a 375 μm n-type doped silicon sample with a resistivity of 1800-2000 Ωm .

The single layer extraction method was applied to the data displayed in figure 6.14 and the complex refractive index was extracted. The extracted data can be found in figure 6.15.

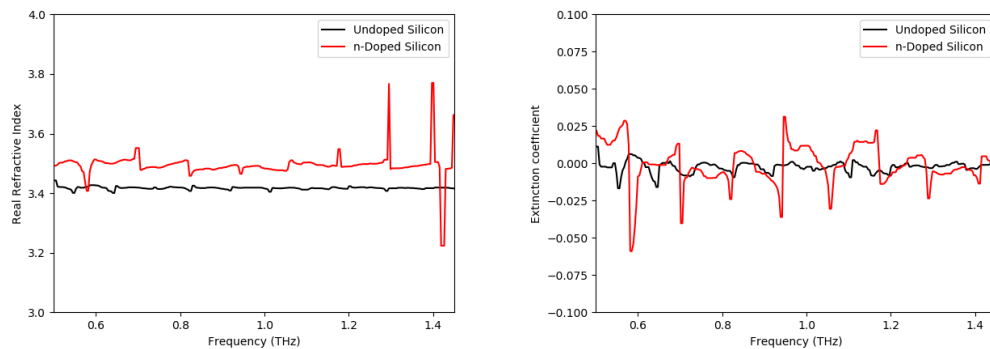


Figure 6.15: The complex refractive index extracted from the data of the n-doped silicon presented in figure 6.14 via the single layer isotropic data extraction technique (red curve) plotted with the same data for the undoped silicon sample (black curve).

As was expected, the extracted value for the real refractive index of the doped silicon sample was found to be higher than that of the undoped silicon sample [46]. We also found the doped silicon sample was still effectively transparent, as can be seen from the extinction coefficient in figure 6.15.

Figure 6.15 also shows that even very lightly doped silicon samples can be distinguished from undoped silicon, showing the sensitivity of the real refractive index in the THz region on doping concentration. Our THz ellipsometer can easily measure these differences.

As discussed in section 5.2.4, the angle of incidence needs to be measured to an accuracy of 0.002° , and the thickness needs to be calculated to an accuracy of 20 nm, for the extinction coefficient of highly transparent samples, such as these, to be extracted with an accuracy $> 90\%$. This is currently not possible with our setup.

These limitations in extracting the extinction coefficient are only an issue when considering transparent samples, as can be seen in section 6.3.1 and is discussed in section 5.2.4. The limitations set by these errors are also far less strenuous for the real refractive index, as seen in these measurements, and discussed in section 5.2.4.

6.4 Single layer isotropic medium followed by bulk isotropic sample

Aqueous samples are of great interest in the THz region [7; 47; 48]. In order to measure these samples, they need to be contained in a sample holder, requiring the THz radiation to first pass through a window material before encountering the aqueous sample. We prepared a number of different samples of different concentrations of water and ethanol. These samples were measured and analyzed using both ellipsometric data extraction and self-referencing data extraction techniques. The extracted complex refractive indexes could be compared to those found in literature [21; 49–51].

6.4.1 High resistivity silicon cuvette filled with water-ethanol mixture

Examining liquid samples was the original motivation for the development of this system. These samples require a container to mount them in the beam path. High resistivity silicon was chosen as an ideal candidate for the window material of the cuvette due to its flat refractive index and low absorption in the THz region. We developed an undoped silicon cuvette, which can be seen in figure 6.16, to house our sample which can easily be mounted in our setup. It consists of a $500\ \mu\text{m}$ thick silicon window and a 6 ml polypropylene chamber. The path length through the cuvette is 4 mm, ensuring that no further internal

reflection will reach the detector due to the strong absorption of water in the THz region.

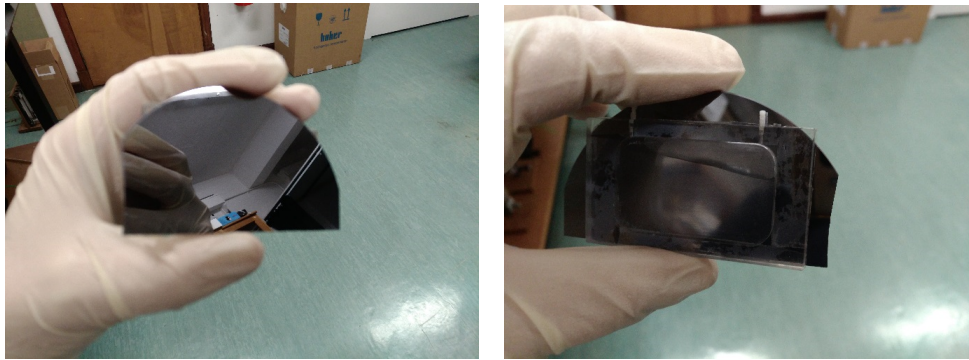


Figure 6.16: Two photos (front and back sides) of the silicon cuvette we developed for use in our setup.

Samples of 0 %, 10 %, 30 % and 40 % ethanol in water were prepared. These samples were alternately placed in the silicon cuvette and the time domain THz ellipsometry data was collected for each sample using our THz ellipsometer. These measurements can be seen in figure 6.17.

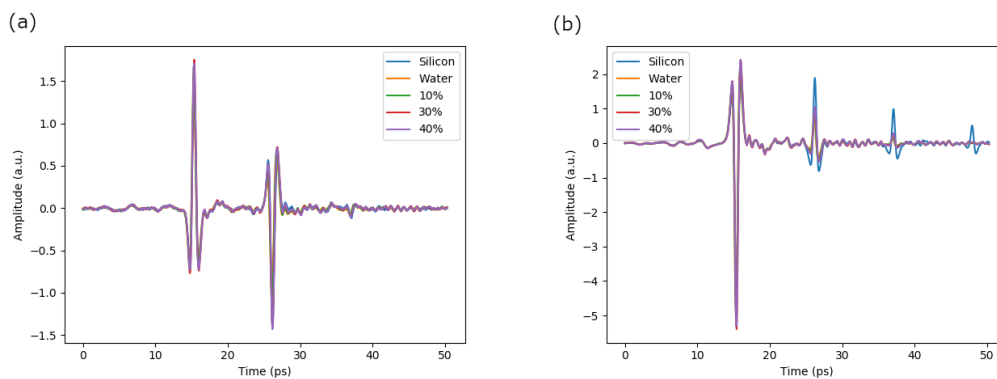


Figure 6.17: In (a) the measured time-domain electric field for the p-polarization can be seen and in (b) the measured time-domain electric field for the s-polarization can be seen. The measurements were conducted for the empty cuvette (denoted as silicon), distilled water, and a 10%, 30% and 40% ethanol-water solution.

In the following subsections the data displayed in figure 6.17 was analyzed via the two layer ellipsometric method, as discussed in section 5.3.1, and the self-reference method, as discussed in section 5.3.2.

6.4.1.1 Ellipsometry

The ellipsometric model for a two layer system, consisting of a single layer isotropic dielectric initial layer and a bulk isotropic second layer, as discussed in section 5.3.1, was applied to the measured data displayed in figure 6.17. Via this method the complex refractive index was extracted for the liquid samples.

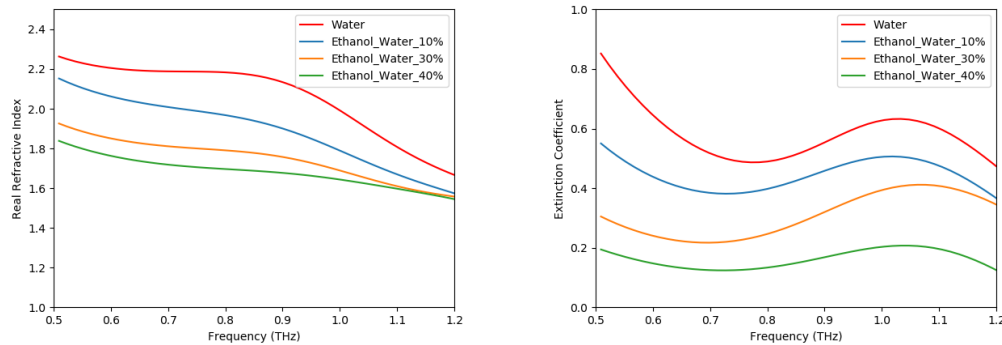


Figure 6.18: The complex refractive index extracted via the method described in section 5.3.1 from the data presented in figure 6.17.

As seen in figure 6.18, a clear difference can be seen in both the extinction coefficient and real refractive index extracted for each sample. As can be seen, both components of the complex refractive index decrease as the ethanol concentration increases. This is in agreement with the results produced by Jepsen *et al.* [21].

6.4.1.2 Self-reference

The self-reference method allows for data extraction from data measured from a two layered system. This method was discussed in section 5.3.2. This method was applied to the data presented in figure 6.17 to extract the complex refractive indexes for the different samples represented. Only the p-polarized electric fields were used during this section.

By applying the data extraction method discussed in section 5.3.2, the real refractive indexes and extinction coefficients of the samples represented by the data in figure 6.18 (a) were extracted. The empty cuvette, represented in figure 6.18 (a) by "Silicon", is used as the reference when calculating the complex refractive indexes.

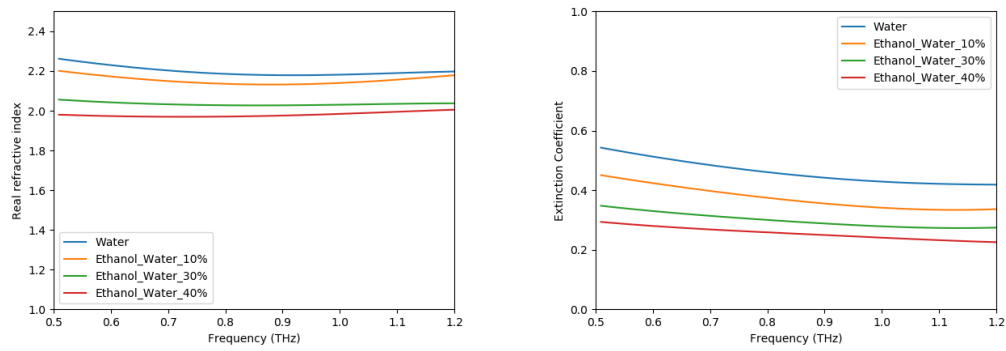


Figure 6.19: The real refractive index extracted via the ellipsometric method and the real refractive index extracted via the self-reference method.

Similar to the results in section 6.4.1.1, it was found that both components of the complex refractive index decrease as the concentration of ethanol increases.

6.4.1.3 Discussion

Both the ellipsometric method, section 6.4.1.1, and self-reference method, section 6.4.1.2, exhibited similar behavior. As the concentration of ethanol in the solution was increased, the extracted complex refractive index of the solution decreased. This was also in agreement with previous work done by Jepsen *et al* [21].

The value extracted for the real refractive index by the ellipsometric method is rather lower than the value extracted by the self-reference method.

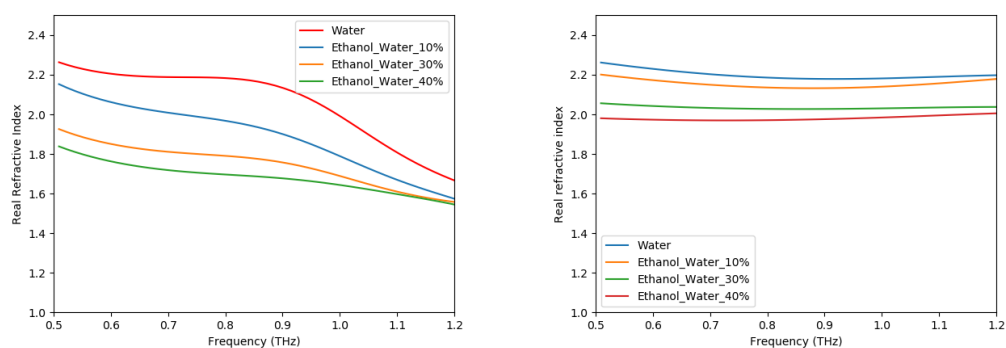


Figure 6.20: The complex refractive index extracted via the method described in section 5.3.2 from the data presented in figure 6.18 (a).

The average difference between the real refractive indexes extracted by the ellipsometric method and self-reference method was 6-15 %, increasing as the concentration of ethanol increased. These differences can arise from small path length differences that get introduced when rotating between S and P polarization measurements. These small path length differences will play no role in the self referencing method as the only the p-polarization measurement is used.

If we convert the complex refractive index extracted for water to the complex dielectric constant ($\tilde{\epsilon} = (n - i\kappa)^2$), we can compare it to data previously extracted by Kindt *et al* [49].

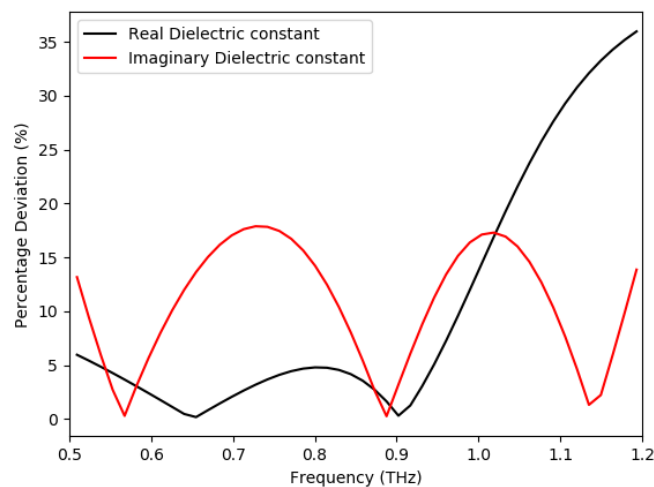


Figure 6.21: The percentage difference in the complex dielectric constant extracted via the ellipsometric method compared to data extracted by Kindt *et al* [49] for water.

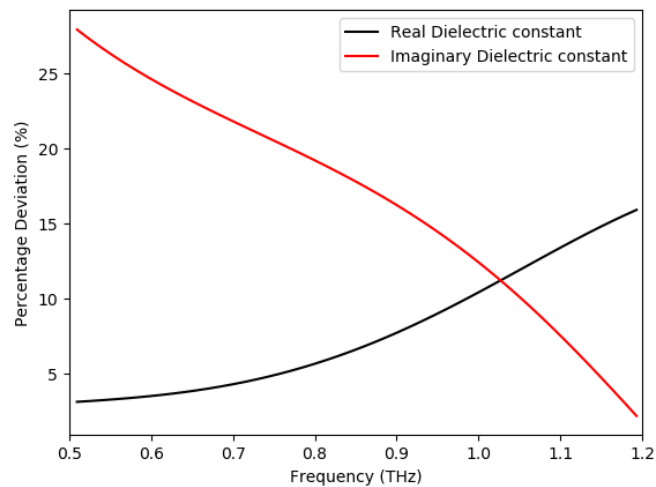


Figure 6.22: The percentage difference in the complex dielectric constant extracted via the self-reference method compared to data extracted by Kindt *et al* [49] for water.

The average difference between the results produced by the self-reference and the data extracted by Kindt *et al* is 7.8% for the real dielectric constant and 16.7% for the imaginary dielectric constant. The average difference between the results produced by the ellipsometric method and the data extracted by Kindt *et al* is 10.5% for the real dielectric constant and 10.7% for the imaginary dielectric constant.

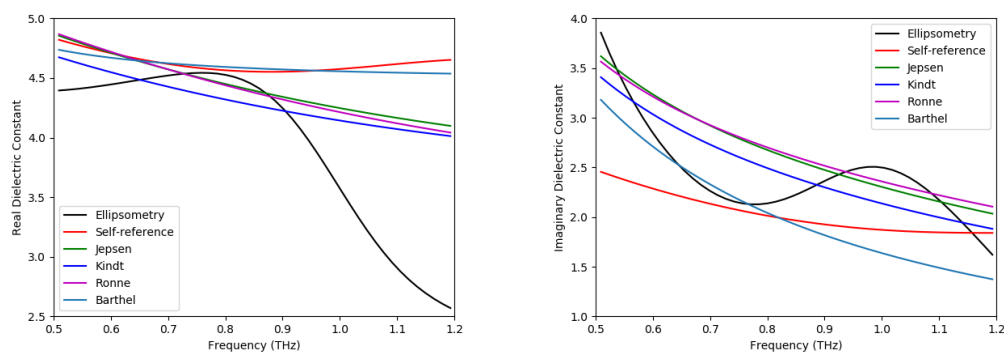


Figure 6.23: The complex dielectric constant of water extracted via ellipsometry and the self-reference method and compared to values previously extracted by Jepsen *et al* [21], Kindt *et al* [49], Ronne *et al* [50] and Barthel *et al* [51].

The real dielectric constant extracted via the ellipsometric method is very similar to the previously extracted values until 0.9 THz and then rapidly diverges from values published in literature, as seen in figure 6.23. The imaginary dielectric constant extracted via the ellipsometric method shows a different trend to those of published values, however the mean value agrees fairly well. The real dielectric constant extracted via the self-reference method is very similar to the values extracted by Barthel *et al* [51]. The imaginary dielectric constant extracted via the self-reference method is somewhat lower than the previously extracted values at low frequencies and has a lower gradient than the previously extracted values.

A potential cause for the difference between the values extracted by the self-reference method and ellipsometric method is that the travel path of the light changes as the system is rotated from p- to s-orientation. This could introduce a change in the angle of incidence of the light reflected at s-polarization, which in turn would affect the resultant data. Alternatively, the presence of absorption resonances can be the reason for these differences. As discussed in section 5.3.3, these two methods produce different results when resonances are present. These resonance based effects could potentially be from water vapour still present in the chamber and not from the sample. Any water vapour resonances still present in the data would be removed in the self-reference case, as an inherent effect of how its correctional values are calculated. In the ellipsometric extraction method the remaining water vapour resonances would not be removed, but instead propagated through the complex refractive index calculated for the first layer of the cuvette.

The literature values extracted for liquid water show a lot of variance. The complex dielectric constant extracted by the self-reference method has a similar trend to data produced by Barthel *et al* [51], whereas the complex dielectric constant extracted by the ellipsometric method shows a rather different trend to those in literature, thus warranting further investigation.

As it currently stands, the self-reference method appears to be a more reliable method to use with our setup, when compared to the two-layer ellipsometric method, as it is resilient to water vapour resonances still present in the data and is resistant to errors introduced by changing between samples.

Chapter 7

Conclusion

We designed and constructed a novel time domain THz ellipsometer. We developed our own THz polarization optics, which in itself is novel within the THz field. Two novel THz ellipsometric data extraction techniques, the single-layer isotropic technique and the two layer ellipsometric technique, were developed. A THz simulation method was pioneered, which was then used to test the aforementioned data extraction techniques, as well as two other data extraction techniques: the bulk isotropic technique and the self-reference method, which were complimentary to our system.

The ellipsometric system was used to obtain time-domain measurements of several different samples, with the complex refractive index extracted from these measurements using the appropriate data extraction technique. From these measurements we found that the system and data extraction techniques worked for a bulk isotropic sample and isotropic samples that are not highly transparent. For transparent samples it was found that the extraction technique performed well for extracting the real refractive index, but is limited in how well it can extract the very small extinction coefficient. This is in part due to the accuracy to which we can measure the angle of incidence. For ethanol-water mixtures of different concentration, both the two-layer ellipsometric method and self-reference method showed that higher ethanol concentrations lead to reduced real refractive indexes and extinction coefficients extracted for the sample. For liquid water the self-reference method produced results similar to those found in literature, but with a slightly lower imaginary dielectric constant and a slightly higher real dielectric constant than expected. The two layer ellipsometric method produced a real dielectric constant close to the expected value for water in the range of 0.5 THz to 0.9 THz. Beyond 0.9 THz the real dielectric constant rapidly diverged from the values found in literature. The extracted imaginary dielectric constant, in the range of 0.5 THz to 1.2 THz, followed a different trend from those found in literature, however the mean value agreed fairly well.

These results show the power of the data extraction techniques with the setup. Together they exhibit the ability to extract optical information for a

multitude of optically isotropic samples. The system can be improved with the future development of THz polarization optics, such as half-wave plates, which would allow for the setup to be more compact. Such a compact setup would be easy to manufacture as a turn-key system. Further expansion and optimization of the data extraction techniques can make this a sought after tool in many industries, such as semi-conductive material production and drug research.

7.1 Future Work

Water vapour is a major issue for terahertz spectroscopy in general. We found that water vapour absorption resonances are still present in our measured data after the chamber was purged with nitrogen. A possible solution to this situation would be to design a smaller, airtight chamber, and perform measurements in vacuum.

The production of a second cuvette, with a different chamber material, might be of use, as this can help determine the cause of the error present in the two-layer measurements. By manufacturing the cuvette from a material with a similar refractive index to that of the window, any reflections from the interface between the window and cuvette will be greatly minimized. If the cuvette body and window were made from the same material, these reflections can be completely eliminated. A candidate for this would be polyethylene, as it has near frequency independent characteristics in the THz region, and it is possible to etch or cast a unibody cuvette from polyethylene, if the proper facilities are available.

Improving the positioning accuracy of the sample can improve the overall functionality of the system. A mount which can consistently mount the sample at a given angle with an accuracy of 0.002° would contribute considerably to measurement and analysis of transparent materials, as the measured data has shown.

Redesigning the ellipsometric setup with the goal of changing the angle of incidence on the sample to 45° might be of use. At 45° incidence, a lower accuracy in general is expected from the data extraction techniques, as the ratio between the reflection coefficients will be closer to one. But the reflection coefficient also vary slower with the angle of incidence, as this is further from the Brewster angle for most samples. This, in turn, results in the system being less affected by misalignment. The construction and evaluation of our time domain THz ellipsometer therefore highlighted a number of design improvements which can be implemented to increase both the ease of use as

well as the accuracy of the extracted complex refractive index of a variety of samples.

Appendices

Appendix A

Knife-Edge

Knife-edge measurements are a rudimentary method for determining the size of a beam. As THz cameras don't exist, this method was employed to help characterize our beam. A knife-edge was translated in the path of the beam, along the x-axis, to determine the beam spot size. The electric field was measured at different points of the knife translation. This electric field was transformed to the frequency domain by FFT and the intensity of the light was calculated by $I(f) \approx E(f)E^*(f)$.

The beam waist, w ($\frac{1}{e^2}$ radius), is computed by fitting equation A.0.1 to the measured data [52].

$$I_{measured} = \frac{I_0}{2} \left[1 + \operatorname{erf} \left(\frac{x_0 - x}{w} \right) \right] \quad (\text{A.0.1})$$

Two different approaches were taken to calculate the beam waist from the calculated intensity.

In the first approach, only the central frequency was considered in each measured data set. The central frequency intensity was plotted as a function of knife-edge translation and equation A.0.1 was fit to it. This data and the resultant fit can be seen in figure A.1.

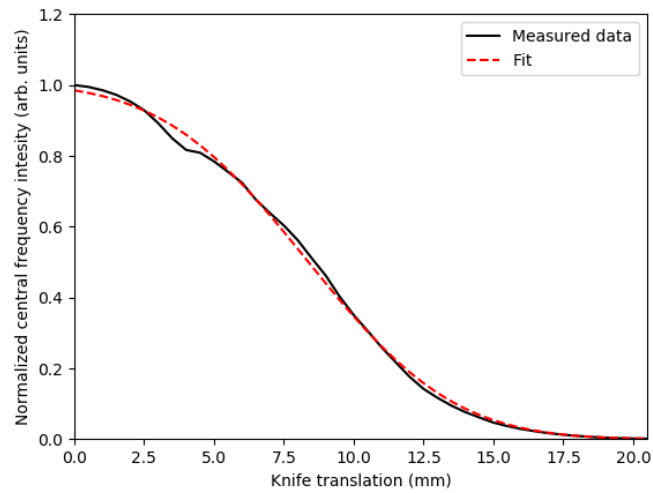


Figure A.1: Knife-edge measurement and fitting of equation A.0.1 on said data when only the central frequency is considered.

In the second approach, the data for the spectral region between 0.5 and 2.0 THz was integrated over. The integrated intensity was plotted as a function of knife-edge translation and equation A.0.1 was fit to it. This data and the resultant fit can be seen in figure A.2.

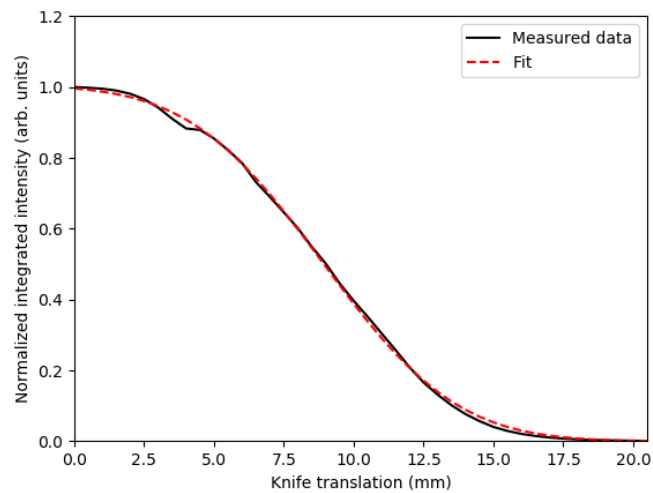


Figure A.2: Knife-edge measurement and fitting of equation A.0.1 on said data when the integrated spectrum is considered.

Method one yielded a beam waist ($\frac{1}{e^2}$ radius) of $5.84 (\pm 0.01)$ mm and method two yielded a beam waist of $5.33 (\pm 0.01)$ mm. The reason for this is that the distribution of the frequency components are frequency dependent. As the knife-edge translates across the beam spot, at first the lower frequency components fall off faster than the higher frequency components, but as the knife-edge gets closer to the center of the beam, the higher frequency components start to rapidly fall off, as can be seen in figure A.3.

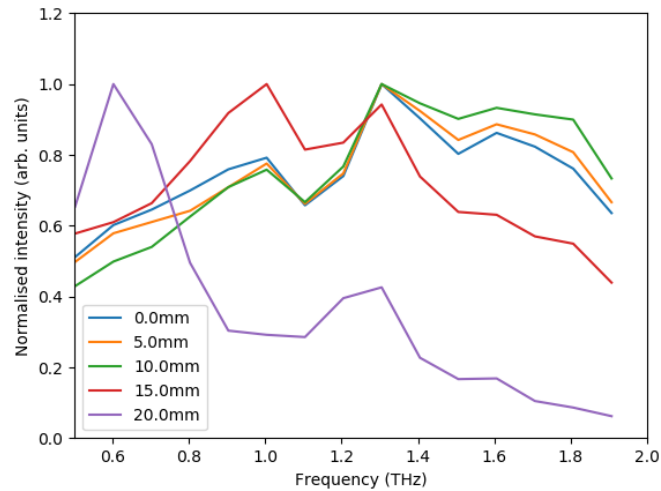


Figure A.3: Normalized spectral intensity measured at different points along the knife-edge translation into the THz beam path.

This would suggest that the lower frequency components of our pulse are distributed further out on the beam spot than the higher frequency components.

Appendix B

Alignment

B.1 Rotational mount alignment

The rotational mount, as described in section 3.3, is an integral component of our THz ellipsometry system. This system will house the stage on which our sample and several mirrors will be mounted. It is paramount that this mount is aligned as optimally as possible, as any miss-alignment it incurs will introduce significant errors to measured data.

Several steps were taken to align the rotational mount. A secondary optical route from the femtosecond laser to the receiving antenna was constructed. This allows the system to operate in transmission when needed.

When the antennae are removed from their mounts, the femtosecond laser travels from the one mount to the other via the current THz optical path. The femtosecond laser was used to find an optimal placement and height for the antenna mounts, such that the light travels through the center of the mount. The mount was then removed, the antennas inserted and aligned in a transmission configuration.

By using a fast oscillating stage on the path to the transmitting antenna, the pulse can be measured on an oscilloscope and changes made by alterations to the alignment of the mount can be viewed in real time. The stage is then placed back in the THz optical path and manipulated until optimal throughput is achieved.

Once the Rotational mount is placed in the system, the same process is used to find the optimal mounting position for the two Brewster stacks.

B.2 Ellipsometric stage and THz antenna alignment

The THz ellipsometric system is sensitive to miss-alignment. An iterative process for aligning the setup was developed.

A HeNe laser is employed for aligning the lenses, mirrors and sample on the plate mounted on the rotational mount. The use of the HeNe laser requires that the Brewster stacks be removed, as the laser light cannot pass through the silicon.

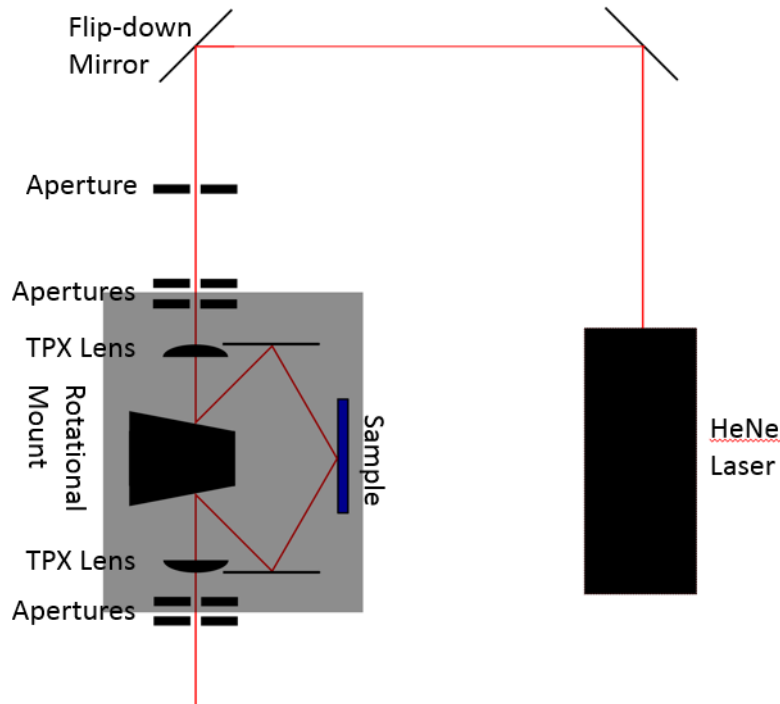


Figure B.1: A diagram of the optical path traveled by the HeNe alignment laser.

A flip-down mirror is used to couple the HeNe laser light onto the THz optical path. This eases the change-over between the use of the alignment laser and the THz pulse in the optical path. Several apertures are used to ensure the HeNe laser is coupled straight in and through the rotational mount, as can be seen in figure B.1. The lenses used in our THz system are made from the polymer TPX. This material allows for both visible and THz radiation to pass through it, thus the HeNe laser is used to align these lenses.

A set of measurements, with the rotational mount set to 0° , 90° , 180° and 270° respectively, with a silver mirror as the sample is taken via the THz system. These measurements are used to determine whether the THz pulse is traveling straight through the ellipsometric system. If not, the alignment of the antennae must be corrected such that the pulse travels straight through the ellipsometric system. An example of measured results before and after this alignment adjustment can be seen in figure B.2.

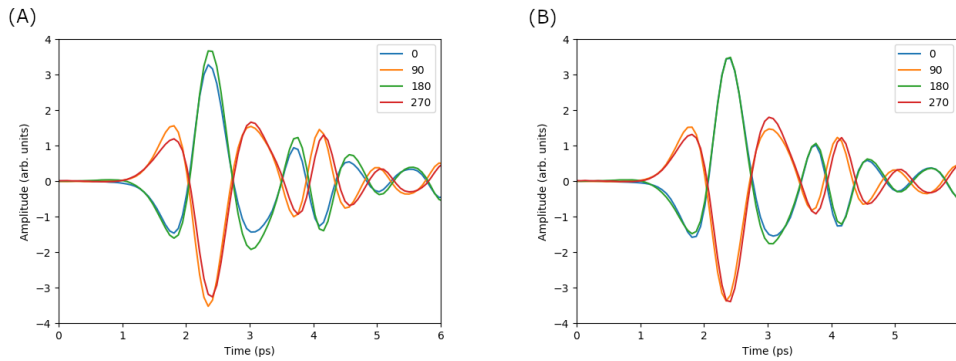


Figure B.2: (a) is a THz time-domain measurement which is poorly centered. (b) is a repeat of the measurement performed for (a), after the alignment of the photo-conductive antennae was improved regarding radiation going straight through the rotational mount.

Next, using a known sample, measurements for p- and s-polarized light reflected from the sample are performed. These measured time-domain electric fields are then compared with electric field produced via simulation, as described in section 4. This comparison allows for the determination of the angle of incidence, as well as whether the sample has been mounted skew.

The angle of incidence is determined by comparing the ratio between the first pulse measured for the s- and p- electric fields, with that of the simulated electric fields. This angle of incidence is applied to the simulation and compared to the measured fields. If the sample has been mounted skew, this will be evidenced by poor overlap between simulated and measured arrival times for pulses beyond the initial pulse. In figure B.3 it can be seen how the secondary pulses drift from the expected arrival time when the sample has been inserted skew.

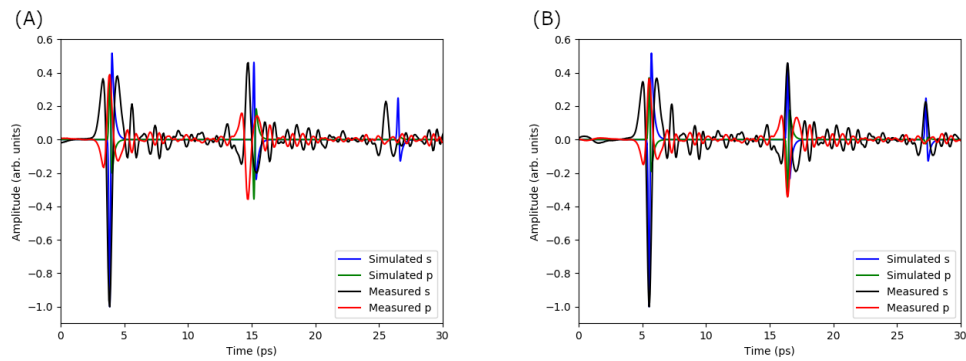


Figure B.3: (a) is a THz time-domain measurement taken of silicon with the sample inserted skew and the simulated expected electric fields. (b) is a repeat of the measurement performed for (a), after the sample was straightened and the system was realigned. The expected simulated electric field is also presented.

The sample used to align the setup was high resistivity, undoped single crystal silicon, which has been measured to have a flat real refractive index of 3.4177 and absorption coefficient of 0.03 cm^{-1} in the THz region [20–22].

If the sample mount is skew, or the angle of incidence needs to be altered, said alteration is applied and the process of aligning the ellipsometric stage components must be repeated.

Appendix C

Calculation of the geometric correction

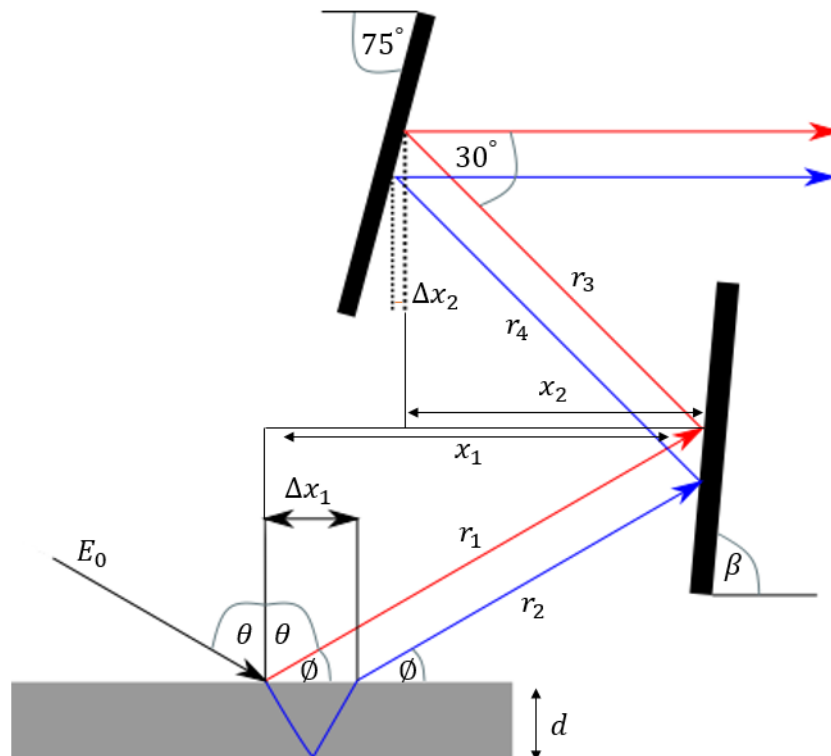


Figure C.1: A ray tracing diagram for calculating the travel time difference between two successive reflections traveling through the setup.

This system can be divided up into two components, a system encompassing r_1 and r_2 and a system focusing on r_3 and r_4 .

Δx_1 is calculated by using Snell's laws.

$$\theta_1 = \sin^{-1}\left(\frac{n_0 \sin(\theta)}{n_1}\right) \quad (\text{C.0.1})$$

$$\Delta x_1 = 2d \tan(\theta_1) \quad (\text{C.0.2})$$

Via construction, a set of similar triangles with r_1 and r_2 as parallel sides is drawn.

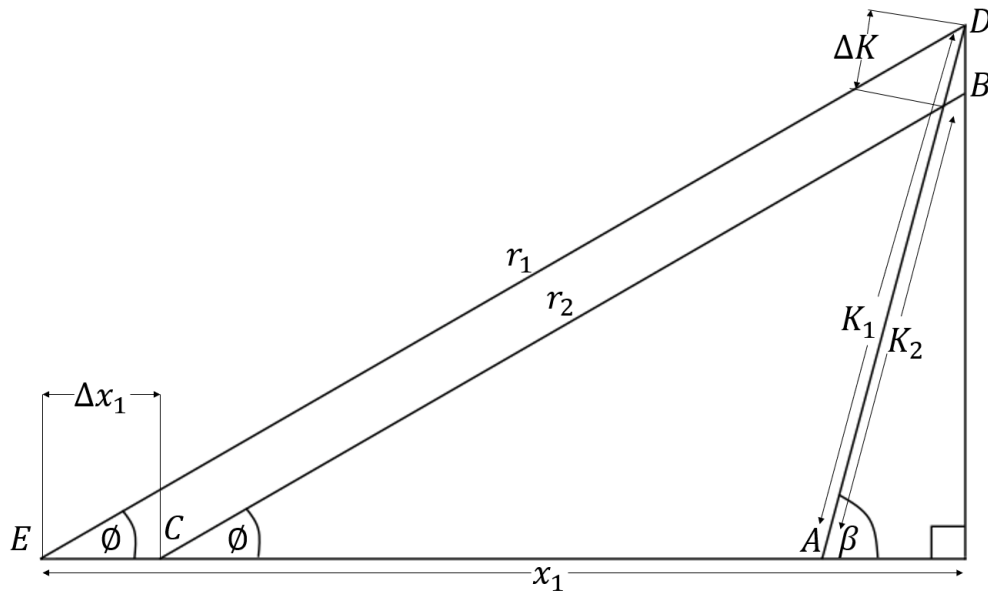


Figure C.2: First part of the construction used to solve the geometric error introduced to subsequent beams.

r_1 and r_2 can be solved by making use of the construction shown in figure C.2. ΔK can also be extracted from this sketch.

$$\phi = 90^\circ - \theta \quad (\text{C.0.3})$$

$$\beta = 75^\circ + \frac{\phi}{2} \quad (\text{C.0.4})$$

$$AE = x_1 - \frac{x_1 \tan(\phi)}{\tan \beta} \quad (\text{C.0.5})$$

$$AC = AE - \Delta x_1 \quad (\text{C.0.6})$$

$$r_1 = \frac{x_1}{\cos(\phi)} \quad (\text{C.0.7})$$

$$K_1 = \sqrt{r_1^2 + AE^2 - 2r_1 AE \cos(\phi)} \quad (\text{C.0.8})$$

$$K_2 = \frac{K_1(AC + 1)}{\Delta x_1} \quad (\text{C.0.9})$$

$$r_2 = \sqrt{K_2^2 + AC^2 - 2K_2 AC \cos \alpha} \quad (\text{C.0.10})$$

$$\Delta K = K_1 - K_2 \quad (\text{C.0.11})$$

r_3 and r_4 , and subsequently Δx_2 , can be solved by via a second construction of two similar triangles, with r_3 and r_4 as similar sides.

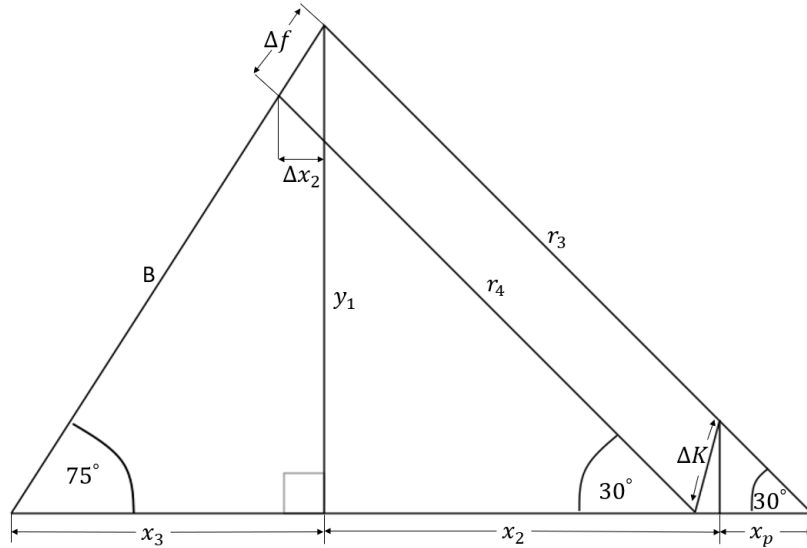


Figure C.3: Second part of the construction used to solve the geometric error introduced to subsequent beams.

$$\Delta y_2 = dK \sin \beta \quad (\text{C.0.12})$$

$$x_p = dK \cos(\beta) + \frac{dy_2}{\tan(30^\circ)} \quad (\text{C.0.13})$$

$$y_1 = (x_2 + x_p) \tan(30^\circ) \quad (\text{C.0.14})$$

$$x_3 = \frac{y_1}{\tan(75^\circ)} \quad (\text{C.0.15})$$

$$B = \frac{y_1}{\sin(75^\circ)} \quad (\text{C.0.16})$$

$$A = x_3 + x_p + x_2 \quad (\text{C.0.17})$$

$$C = \frac{x_2 + x_p}{\cos(30^\circ)} \quad (\text{C.0.18})$$

$$\Delta f = \frac{x_p B}{(A - x_p) \left(1 + \frac{x_p}{A - x_p}\right)} \quad (\text{C.0.19})$$

$$\Delta x_2 = \Delta f \cos(75^\circ) \quad (\text{C.0.20})$$

$$r_3 = C - \frac{dy_2}{\sin(30^\circ)} \quad (\text{C.0.21})$$

$$a = A - x_p \quad (\text{C.0.22})$$

$$b = B - \Delta f \quad (\text{C.0.23})$$

$$r_4 = \sqrt{a^2 + b^2 - 2ab \cos(75^\circ)} \quad (\text{C.0.24})$$

$$\Delta r_1 = r_1 - r_2 \quad (\text{C.0.25})$$

$$\Delta r_2 = r_3 - r_4 \quad (\text{C.0.26})$$

$$\Delta l = \Delta r_1 + \Delta r_2 - \Delta x_2 \quad (\text{C.0.27})$$

Δl represents the total change in the path length of the second ray through the optical setup and is used to calculate how much earlier the the internal reflections will be measured than they would be expected to if only the travel distance through the sample were to be considered.

Bibliography

- [1] Xuequan, C., Parrott, E., Huang, Z., Hau-ping, Z. and Pickwell-Macpherson, E.: Robust and accurate terahertz time-domain spectroscopic ellipsometry. *Chinese Laser Press*, vol. 6, no. 8, pp. 768–775, 2018.
- [2] Karl, N., Heimbeck, M.S., Everitt, H.O., Chen, H.-T., Taylor, A.J., Brener, I., Benz, A., Reno, J.L., Mendis, R. and Mittleman, D.M.: Characterization of an active metasurface using terahertz ellipsometry. *Applied Physics Letters*, vol. 111, no. 19, p. 191101, 2017.
- [3] Neshat, M. and Armitage, N.P.: Developments in THz range ellipsometry. *Journal of infrared, millimeter and terahertz waves*, vol. 34, pp. 682–708, 2013.
- [4] Hoshina, H., Morisawa, Y., Sato, H., Kamiya, A., Noda, I., Ozaki, Y. and Otani, C.: Higher order conformation of poly(3-hydroxyalkanoates) studied by terahertz time-domain spectroscopy. *Applied Physics Letters*, vol. 96, pp. 101904–101904, 2010.
- [5] Han, X., Yan, S., Zang, Z., Wei, D., Cui, H. and Du, C.: Label-free protein detection using terahertz time-domain spectroscopy. *Biomedical Optics Express*, vol. 9, no. 3, pp. 994–1005, 2018.
- [6] Born, B., Kim, S.J., Ebbinghaus, S., Gruebele, M. and Havenith, M.: The terahertz dance of water with the proteins: the effect of protein flexibility on the dynamical hydration shell of ubiquitin. *Faraday Discussions*, vol. 141, pp. 161–173, 2009.
- [7] Novelli, F., Pour, S.O., Tollerud, J., Roozbeh, A., Appadoo, D.R.T., Blanch, E.W. and Davis, J.A.: Time-domain THz spectroscopy reveals coupled protein-hydration dielectric response in solutions of native and fibrils of human lysozyme. *Journal of Physical Chemistry B*, vol. 121, pp. 4810–4816, 2017.
- [8] Wu, Y., Su, B., He, J., Zhang, C., Zhang, H., Zhang, S. and Zhang, C.: An effective way to reduce water absorption to terahertz. In: Wang, Y., Jia, B., Tatsuno, K. and Dong, L. (eds.), *2017 International Conference on Optical Instruments and Technology: Optical Systems and Modern Optoelectronic Instruments*, vol. 10616, pp. 315–323. International Society for Optics and Photonics, SPIE, 2018.
- [9] Nagashima, T. and Hangyo, M.: Measurement of complex optical constants of a highly doped si wafer using terahertz ellipsometry. *Applied Physics Letters*, vol. 74, no. 24, pp. 3917–3919, 2001.

- [10] Driscoll, W.G.: *Handbook of Optics*. McGraw-Hill Inc., 1978.
- [11] Griffiths, D.J.: *Introduction to Electrodynamics*. 3rd edn. Pearson Education, Inc, Pearson Benjamin Cummings, 1301 Sansome St., San Francisco, CA 94111, 2008.
- [12] Kovalenko, S.A.: Descartes-snell law of refraction with absorption. *Semiconductor Physics, Quantum Electronics & Optoelectronic*, vol. 4, no. 3, pp. 214–218, 2001.
- [13] Tompkins, H.G. and Irene, E.A.: *Handbook of Ellipsometry*. William Andrew Publishing, 2005.
- [14] Swinburne University of Technology: Blackbody radiation. 2019.
Available at: <http://astronomy.swin.edu.au/cosmos/B/Blackbody+Radiation>
- [15] Hubers, H.W.: Terahertz heterodyne receivers. *IEEE Journal of Selected Topics in Quantum Electronics*, vol. 14, no. 2, pp. 378–391, March 2008.
- [16] Siegel, P.H.: Terahertz technology. *IEEE Transactions On Microwave Theory and Techniques*, vol. 50, no. 3, pp. 910–927, March 2002.
- [17] Sakai, K.: *Terahertz Optoelectronics*. 1st edn. Springer-Verlag, Springer-Verlag New York, LLC, 233 Spring Street, New York, NY 10013, USA, 2005.
- [18] Xie, X., Dai, J. and Zhang, X.C.: Coherent control of thz wave generation in ambient air. *Physical Review Letters*, vol. 97, no. 075005, pp. 1–4, February 2006.
- [19] Tydex: Thz polarizers. 2018.
Available at: http://www.tydexoptics.com/products/thz_optics/thz_polarizers1/
- [20] Li, J.S. and Li, J.R.: Dielectric properties of silicon in terahertz region. *Microwave and Optical Technology Letters*, vol. 50, no. 5, 2008.
- [21] Jepsen, P.: Investigation of aqueous alcohol and sugar solutions with reflection terahertz time-domain spectroscopy. *Optics Express*, vol. 15, no. 22, pp. 14717–14737, 2007.
- [22] Grischkowsky, D.: Far-infrared time-domain spectroscopy with terahertz beams of dielectrics and semiconductors. *Journal of the Optical Society of America B*, vol. 7, no. 10, pp. 2006–2015, 1990.
- [23] Bass, M., DeCusatis, C., Enoch, J., Lakshminarayanan, V., Li, G., MacDonald, C., Mahajan, V. and Van Stryland, E.: *Handbook of Optics: Geometrical and Physical Optics, Polarized Light, Components and Instruments*, vol. 1. 3rd edn. 2010.
- [24] Tydex: Thz broad-band phase transformers. 2019.
Available at: http://www.tydexoptics.com/pdf/THz_Broad-band_Phase_Transformers.pdf

- [25] Neshat, M. and Armitage, P.: Terahertz time-domain spectroscopic ellipsometry: instrumentation and calibration. *Optics Express*, vol. 20, no. 27, pp. 29063–29075, 2012.
- [26] Charkhesht, A., Regmi, C.K., Mitchell-Koch, K.R., Cheng, S. and Vinh, N.Q.: High-precision megahertz-to-terahertz dielectric spectroscopy of protein collective motions and hydration dynamics. *The Journal of Physical Chemistry B*, vol. 122, no. 24, pp. 6341–6350, 2018.
- [27] Shin, H.J., Choi, S.-W. and Ok, G.: Qualitative identification of food materials by complex refractive index mapping in the terahertz range. *Food Chemistry*, vol. 245, pp. 282–288, 2018.
- [28] Sommer, S., Koch, M. and Adams, A.: Terahertz time-domain spectroscopy of plasticized poly(vinylchloride). *Analytical Chemistry*, vol. 90, pp. 2409–2413, 2018.
- [29] Yamada, T., Kaji, T., Chiyumi, I.A., Maya, Y., Shingo, M., Yukihiro, S., Tanaka, T.S. and Otomo, A.: Terahertz time domain and far-infrared spectroscopies of side-chain electro-optic polymers. *Japanese Journal of Applied Physics*, vol. 55, pp. 1–5, 2016.
- [30] Cunningham, P.D., Valdes, N.N., Vallejo, F.A., Hayden, L.M., Polishak, B., Zhou, X.-H., Luo, J., Jen, A.K.-Y., Williams, J.C. and Twieg, R.J.: Broadband terahertz characterization of the refractive index and absorption of some important polymeric and organic electro-optic materials. *Journal of Applied Physics*, vol. 109, no. 043505, pp. 1–5, 2011.
- [31] Polyanskiy, M.N.: Refractive index database. 2019.
Available at: <https://refractiveindex.info>
- [32] Technical note: Gaussian beam optics. 2019.
Available at: <https://www.newport.com/n/gaussian-beam-optics>
- [33] Marsik, P., Sen, K., Khmaladze, J., Yazdi-Rizi, M., Mallett, B.P.P. and Bernhard, C.: Terahertz ellipsometry study of the soft mode behavior in ultrathin SrTiO₃ films. *Applied Physics Letters*, vol. 108, no. 5, p. 052901, 2016.
- [34] Chen, X., Parrott, E.P.J., Tekavec, P. and Pickwell-MacPherson, E.: A novel method for accurate THz ellipsometry. pp. 1–2, Aug 2017. ISSN 2162-2035.
- [35] Pupeza, I., Wilk, R. and Koch, M.: Highly accurate optical material parameter determination with THz time-domain spectroscopy. *Optics Express*, vol. 15, no. 7, pp. 4335–4350, 2007.
- [36] Lagarias, J.C., Reeds, J.A., Wright, M.H. and Wright, A.E.: Convergence properties of the nelder-mead simplex method in low dimensions. *SIAM Journal on Optimization*, vol. 9, no. 1, pp. 112–147, 1998.
- [37] Hejase, J.A.: *Terahertz time-domain methods for material characterization of layered dielectric media*. Ph.D. thesis, Michigan State University, 2012.

- [38] Weisstein, E.W.: Simplex. 2020.
Available at: <http://mathworld.wolfram.com/Simplex.html>
- [39] The SciPy community: `scipy.optimize.minimize`. 2019.
Available at: <https://docs.scipy.org/doc/scipy/reference/generated/scipy.optimize.minimize.html>
- [40] Jankowitz, M.D.: *Some Statistical Aspects of LULU smoothers*. Ph.D. thesis, Stellenbosch University, 2007.
- [41] Kao, O.: Modification of the LULU operators for the preservation of critical image details. In: *Proceedings of the 2001 International Conference on Imaging Science, Systems, and Technology*, pp. 280–286. 2001.
- [42] Zhang, Z.: An improvement to the brents method. *International Journal of Experimental Algorithms*, vol. 2, no. 1, pp. 21–26, 2011.
- [43] National Instruments: Understanding ffts and windowing. 2019.
Available at: <https://www.ni.com/en-za/innovations/white-papers/06/understanding-ffts-and-windowing.html>
- [44] Stearns, C.W.: A generalized hann window for apodization of filtered backprojection pet images. In: *IEEE Nuclear Science Symposium Conference Record*, vol. M11-351, pp. 2719–2721. IEEE, 2005.
- [45] Zill, D.G. and Cullen, M.R.: *Differential Equations with Boundary Value Problems*. 7th edn. Brooks/Cole, 10 Davis Drive, Belmont, CA 94002-3098, USA, 1988.
- [46] Hangyo, M., Nagashima, T. and Nashima, S.: Spectroscopy by pulsed terahertz radiation. *Measurement Science and Technology*, vol. 13, pp. 1727–1738, 2002.
- [47] Born, B., Kim, S.J., Ebbinghaus, S., Gruebele, M. and Havenith, M.: The terahertz dance of water with the proteins: the effect of protein flexibility on the dynamical hydration shell of ubiquitin. *Faraday Discussions*, vol. 141, pp. 161–173, 2009.
- [48] Sun, J., Niehues, G., Forbert, H., Decka, D., Schwaab, G., Marx, D. and Havenith, M.: Understanding THz spectra of aqueous solutions: Glycine in light and heavy water. *Journal of the American chemical society*, vol. 136, pp. 5031–5038, 2014.
- [49] Kindt, J.T. and Schmuttenmaer, C.A.: Far-infrared dielectric properties of polar liquids probed by femtosecond terahertz pulse spectroscopy. *Journal of Physical Chemistry*, vol. 100, no. 24, pp. 10373–10379, 1996.
- [50] Ronne, C. and Thrane, L.: Investigation of the temperature dependence of dielectric relaxation in liquid water by THz reflection spectroscopy and molecular dynamics simulation. *Journal of chemical physics*, vol. 107, no. 14, pp. 5319–5331, 1997.

- [51] Barthel, J., Bachhuber, K., Buchner, R. and Hetzenauer, H.: Dielectric spectra of some common solvents in the microwave region. water and lower alcohols. *Chemical Physics Letters*, vol. 165, no. 4, pp. 369–373, 1990.
- [52] Marcos, A.C., de Araújo, R., Silva, E., de Lima, D., Pereira, P. and de Oliveira, P.C.: Measurement of gaussian laser beam radius using the knife-edge technique: improvement on data analysis. *Applied Optics*, vol. 48, no. 2, pp. 393–396, 2009.